# Recent development in Metal Halide Perovskites Synthesis to improve their charge-carrier mobility and photocatalytic efficiency

*Marija Knezevic,[1] Thi-Hieu Hoang,[1] Nusrat Rashid,[2] Mojtaba Abdi-Jalebi,[2] Christophe Colbeau-Justin,[1] Mohamed Nawfal Ghazzal*[,1]*

[1] Université Paris-Saclay, Institut de Chimie Physique, UMR 8000 CNRS, 91405, Orsay, France

[2] Institute for Materials Discovery, University College London, Malet Place, London, WC1E 7JE, UK

*Correspondence and requests for materials should be addressed to Ass. Prof. Dr. Mohamed Nawfal Ghazzal (email: mohamed-nawfal.ghazzal@universite-paris-saclay.fr).

*Keywords: all-inorganic halide perovskite; charge-carrier dynamics; stability; photocatalysis.*

**Abstract:** Over the past decade, all inorganic metal halide perovskites (MHPs, $CsPbX_3$: X = Cl, Br, I) have been widely investigated as promising materials for optoelectronic devices such as solar cells and light-emitting diodes. MHPs are defect tolerant, which allows tuning of their bandgap without altering their photophysical properties. From a fundamental point of view, MHPs are excellent candidates for photocatalytic reactions due to their light-harvesting capability, high photogenerated charge-carrier mobility, long diffusion lengths, and tunable bandgap energy. In this review, we provide an overview of various MHPs engineering strategies (e.g., surface, morphological, and structural modifications, heterojunction coupling, and encapsulation) which are directly linked to the charge-carrier mobility and lifetimes, and then to the photocatalytic efficiency. Specifically, we outline different synthetic approaches resulting in surface and morphological modifications, anion/cation substitution, metallic doping, coupling, and encapsulation that tremendously influence MHP's stability, optical properties, and charge-carrier dynamics at variable time scales (from fs to μs). We also provide an in-depth evaluation of the MHP's for variable photoredox reactions, discussing how the optical and electronic properties help to improve their stability and efficiency.

## 1. Introduction

In the last decade, all-inorganic metal halide perovskites (MHPs) $CsPbX_3$ (X=Br, Cl, I) have received a close review of the photochemical and photoelectrochemical communities, although

their stoichiometry [1], crystallinity [2, 3], and photoconductivity [4] have been known for more than a century. The successful story of perovskites started in 1840, when the term perovskite was firstly used by German mineralogist Gustav Rose to describe the newly discovered $ABX_3$ compound during his exploratory expedition in Russia i.e. $CaTiO_3$, in honor to Lev Alekseyevich Von Perovski, a Russian mineralogist [5]. Since then, this naming was widely accepted as a common designation for all $ABX_3$ materials [6]. Later in 1893, compounds based on cesium, lead, and halides from aqueous solutions, $CsPbX_3$ (X=Br, Cl, I), were reported, as well as non-perovskite structures such as $Cs_4PbX_6$ and $CsPb_2X_5$ (X=Br, Cl) [1]. The first detail of crystalline MHPs structure was revealed for the high-temperature $CsPbI_3$ perovskite phase in 1958 [2]. Two phases were described, the black cubic and yellow orthorhombic. The latter is a non-perovskite phase but thermodynamically favored and stable under ambient conditions. The cubic crystals of $CsPbCl_3$ and $CsPbBr_3$ were found to be formed at a temperature above 320K and 400K, respectively [3]. The phase transition studies of MHPs showed the transformation from orthorhombic through tetragonal to cubic phase with the temperature increase, and even monoclinic $CsPbCl_3$ at a temperature lower than 310K (Table 1) [7].

It is worth mentioning that with the expansion of both hybrid and all-inorganic perovskites, the term "perovskite" has been employed for all compounds containing Cs, Pb, and Br atoms, regardless of their ratio [8–11]. J. Breternitz and S. Schorr emphasized the importance of defining perovskite as a crystalline structure $ABX_3$ (or A:B:X=1:1:3), with B cation having either octahedral or distorted octahedra coordination, organized in all-corner 3D sharing network. Since 0D, 1D, and 2D e.g. $Cs_4PbX_6$ and $CsPb_2X_5$, do not share such properties, they are considered as non-perovskite structures [12]. More recently, Q. A. Akkerman and L. Manna explained different metal halide lattice distortions, distinguishing cubic, anti, distorted, vacant, ordered, and vacancy-ordered perovskites. Due to the size difference of the A, B cations, and X anion, halide perovskites usually suffer from certain distortions and do not crystalize in perfect cubic phase (aristotype), but rather experience lower symmetry (hettotype) [13]. What has to be taken into account when describing a crystallite as halide perovskite is certainly its stability with Goldschmidt tolerance factor (*t, $0.80 \leq t \leq 1.00$*),[6, 14, 15] and octahedral factor ($\mu$>0.41) [14, 15].

**Table 1**. Structural properties of all-inorganic perovskites $CsPbX_3$

| Lattice parameters (Å) | | | Space | Crystal symmetry | Phase | Ref. |
|---|---|---|---|---|---|---|
| a | b | c | group | | transition | |

| | | | | | | temperature (K) | |
|---|---|---|---|---|---|---|---|
| **$CsPbCl_3$** | 5.607 | 5.575 | 5.572 | Pmmm | orthorhombic | 315>T>310 | [3]·[16]·[7] |
| | 5.590 | 5.590 | 5.630 | P4/mbm | tetragonal | 320>T>315 | |
| | | 5.605 | | Pm-3m | cubic | 320 | |
| **$CsPbBr_3$** | 8.207 | 8.255 | 11.759 | Pbnm | orthorhombic | ambient | [17, 18] |
| | 5.827 | 5.827 | 5.891 | P4/mbm | tetragonal | 266-397 | |
| | | 5.874 | | Pm-3m | cubic | 410-500 | |
| **$CsPbI_3$** | 10.028 | 4.853 | 18.164 | Pnma | orthorhombic ($\delta$) | ambient | [19, 20] |
| | 6.095 | 6.259 | 6.250 | Pbnm | orthorhombic ($\gamma$) | 325 | |
| | 6.241 | 6.241 | 6.299 | P4/mbm | tetragonal ($\beta$) | 510 | |
| | | 6.297 | | Pm-3m | Cubic ($\alpha$) | 645 | |

In the following fifty years, the optical and electronic properties of MHPs have been discussed, including their application for the X-ray and γ-ray radiation detection [21–26]. Despite the quantum confinement effect of $CsPbX_3$-like quantum dots (X=Br, Cl) in CsX single-crystal host (X = Cl, Br), being known since 1997 [24], it was only after the breakthrough of $CsPbX_3$ nanocrystals (NCs) colloidal synthesis in 2015 that the astonishing development of MHP NCs synthetic methods has been recorded [20]. Further photophysical studies disclosing high photoluminescence quantum yield (PLQY), charge-carrier mobility, and diffusion lengths, i.e. the micrometer range, have followed [27–29]. By the time the first research MHP-based solar cell was proposed [30], hybrid organic-inorganic perovskite solar cells had already been extensively investigated [31–34]. The iodine-based MHPs strike immense attention due to their small bandgap of 1.73 eV [35]. However, their rapid phase transformation and relatively limited stability prevent the extension of their field of application. The ongoing studies are focused on their stability improvement; e.g. it is shown that heating up the yellow non-perovskites phase (δ–perovskite) results in the orthorhombic perovskite phase upon cooling (γ–perovskites), allowing longer stability under ambient conditions [36]. Up to date, perovskite-silicon tandem solar cells registered the energy conversion efficiency record, reaching up to 31.3%, while single-junction perovskite solar cells reached the efficiency of 25.7% [37], being in close competition with the conventional thin-film and silicon solar cells. The MHPs have been used in a wide range of applications, being identified as promising materials for optoelectronics [28, 38, 39], and very recently photocatalysis, which will be discussed thoroughly in this review. Besides being optically active in a large range of the solar spectrum, to be considered as an efficient photocatalyst, MHPs should be able to convert quantum energy to highly mobile and long-lived charge carriers and overcome instability

to moisture, non-polar media, and illumination-induced phase segregation. In general, the stability and photoelectronic properties of MHPs, which determine their photocatalytic efficiency, are elaborated through MHP coating with stable materials, and selective control of the synthetic procedure of MHPs. In this review, we will first expose diverse synthetic procedures, reported up to now, that offer great flexibility and versatility in morphology control, electronic bandgap engineering, and enhancement of charge carriers' lifetime. Then, an overview of the photoelectronic properties, and their evolution through a selective substitution of the anion (or cation) atom in terms of light-harvesting properties will be discussed [20, 40–56]. The last part is dedicated to the recent advancements and achievements of MHPs as a photoactive photocatalyst.

## 2. Synthetic methods for $CsPbX_3$ nanocrystals

The time and energy-consuming protocols are the main challenges facing industrial scale-up MHP synthesis, while keeping excellent dispersion, size distribution, structural, optical, and photophysical properties of nanocrystals. Nanocrystal colloidal hot injection method [20] has led to the development of different synthetic procedures such as microwave-assisted [57–61], ultrasonication [49, 62–64], solvothermal [65–70], ligand-assisted reprecipitation (LARP) [71, 72], post-synthetic anion exchange [40, 51], cation exchange [53], and conversion of $Cs_4PbX_6$ [73–76]. Here, we will discuss the versatility of different synthetic methods that yield nanocubes (NCus), nanowires (NWs), nanorods (NRs), nanoplatelets (NPLs), and nanosheets (NSs), as well as their advantages and emerging green perovskite synthesis [77–79].

### *2.1. Direct synthesis of MHPs*

#### *2.1.1. Hot-injection method*

The extensively used, hot-injection method consists of a quick injection of cesium-oleate (Cs-oleate) in the solution of $PbX_2$ (X=Br, I, Cl) in octadecene (ODE), containing oleylamine (OAm), and oleic acid (OA) as capping agents, under inert gas or vacuum, followed by immediate quenching in the ice water bath:

$$2Cs(RCOO) + 3PbX_2 \rightarrow 2CsPbX_3 + Pb(RCOO)_2 \quad (1)$$

The reaction is performed in the temperature range of 140-200 °C allowing variation of the particle size in the range of 4-15 nm (Figure 1a) [20]. The Cs-oleate is prepared separately by mixing

cesium-carbonate ($Cs_2CO_3$) or cesium-acetate (CsOAc) with OA in ODE at 120 °C:

$$Cs_2CO_3 + 2RCOOH \rightarrow 2Cs(RCOO) + CO_2 + H_2O \quad (2)$$

The advantage of using Cs-acetate lies in its non-hygroscopic nature and the liquid state of Cs-oleate upon cooling [80]. However, *Lu et al.* demonstrated that $Cs_2CO_3$ can be completely dissolved with the ratio of Cs:OA = 1:5, allowing complete solubility at room temperature, making $CsPbBr_3$ synthesis independent on Cs-oleate precursor origin (Figure 1b,c) [81]. Cs-oleate in ODE is then heated and injected into the mixture of Pb-oleate and OAm-X (3) to trigger the formation of $CsPbX_3$ and oleylammonium oleate (4). The metathesis reaction completion is driven by an excess of $PbX_2$ relative to $CsPbX_3$ [82]:

$$PbX_2 + 2RCOOH + 2\mathrm{R'NH_2} \rightarrow \mathrm{Pb(OOCR)_2} + 2R'NH_3X \ (X = Br, I) \quad (3)$$

$$Cs(RCOO) + Pb(OOCR)_2 + 3R'NH_3X \rightarrow CsPbX_3 + 3R'NH_3OOCR \ (X = Br, I) \quad (4)$$

$$R = CH_3(CH_2)_7HC = CH(CH_2)_7 \quad R' = CH_3(CH_2)_7HC = CH(CH_2)_8$$

The MHPs morphology can be controlled by adjusting injection rate of Cs-oleate, during the synthesis of $CsPbI_3$ NCs, forming either NCus (0.4 mL $s^{-1}$) or NRs (0.4 mL $min^{-1}$) (Figure 1d), on the contrary, injection rate has no impact on $CsPbBr_3$ morphology (Figure 1e,f) [83].

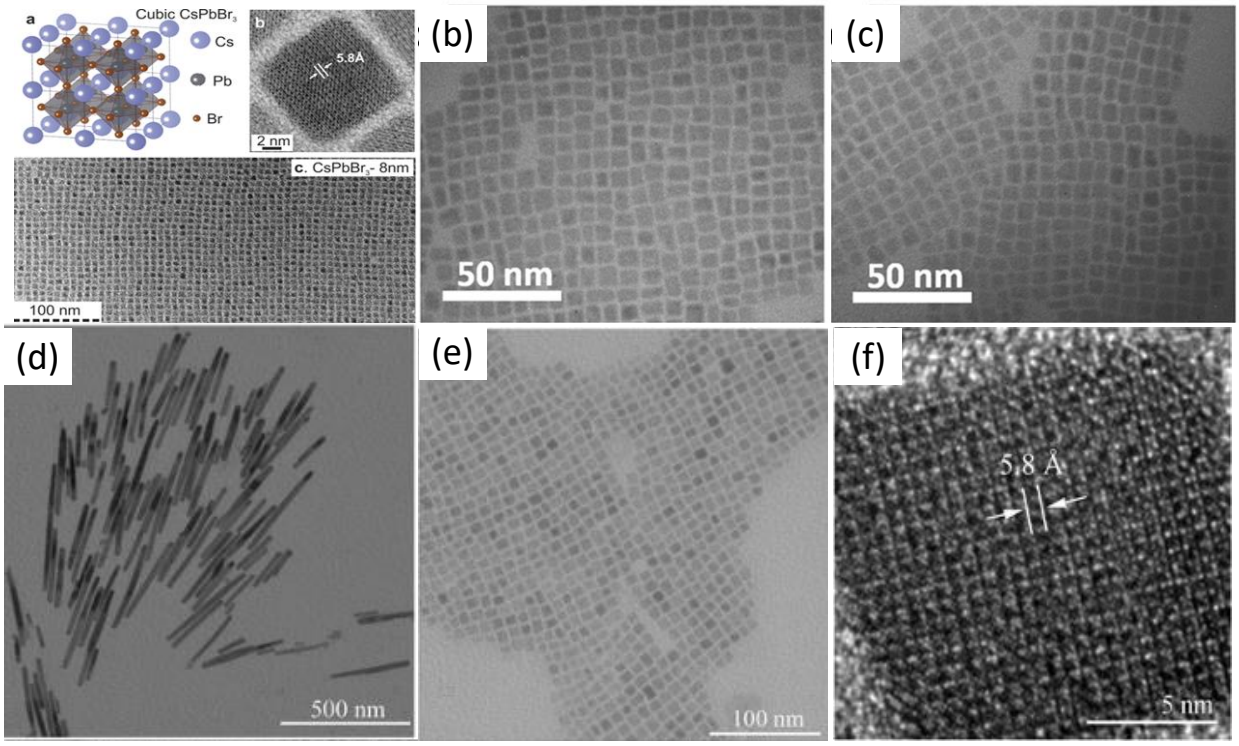


**Figure 1.** (a) HRTEM and TEM images of $CsPbBr_3$ and structural model of $CsPbBr_3$ (insert). Reproduced with permission [20]. Copyright 2015 American Chemical Society. (b) $CsPbBr_3$ prepared with Cs-oleate (OAc) and (c) Cs-oleate ($CO_3$) with Cs:OA ratio 1:5. Reproduced with permission [81]. Copyright 2018 American Chemical Society. (d) The effect of the injection rate of 0.4 mL $min^{-1}$ on $CsPbI_3$ NRs and (e, f) $CsPbBr_3$ NCu synthesis. Reproduced with permission [83]. Copyright 2017 Elsevier B.V.

Significant attention was dedicated to the influence of different capping agents i.e. carboxylic acids and alkyl amines, on NCs stability [84–86]. A variation of acid/amine ratio, chain length, and temperature dictates the control of the shape, size, and morphology of the MHPs, giving rise to NCus, NPLs and NSs (Figure 2) [80, 84, 87]. The long-chain capping agents, i.e. OA/OAm mixture, and their density control enhance NCs surface passivation, a feature crucial for improving photoluminescence in LED manufacturing [88, 89]. However, during the purification process MHPs could suffer from ligand loss, due to the proton transfer between acid and base, lowering NCs stability [89, 90].

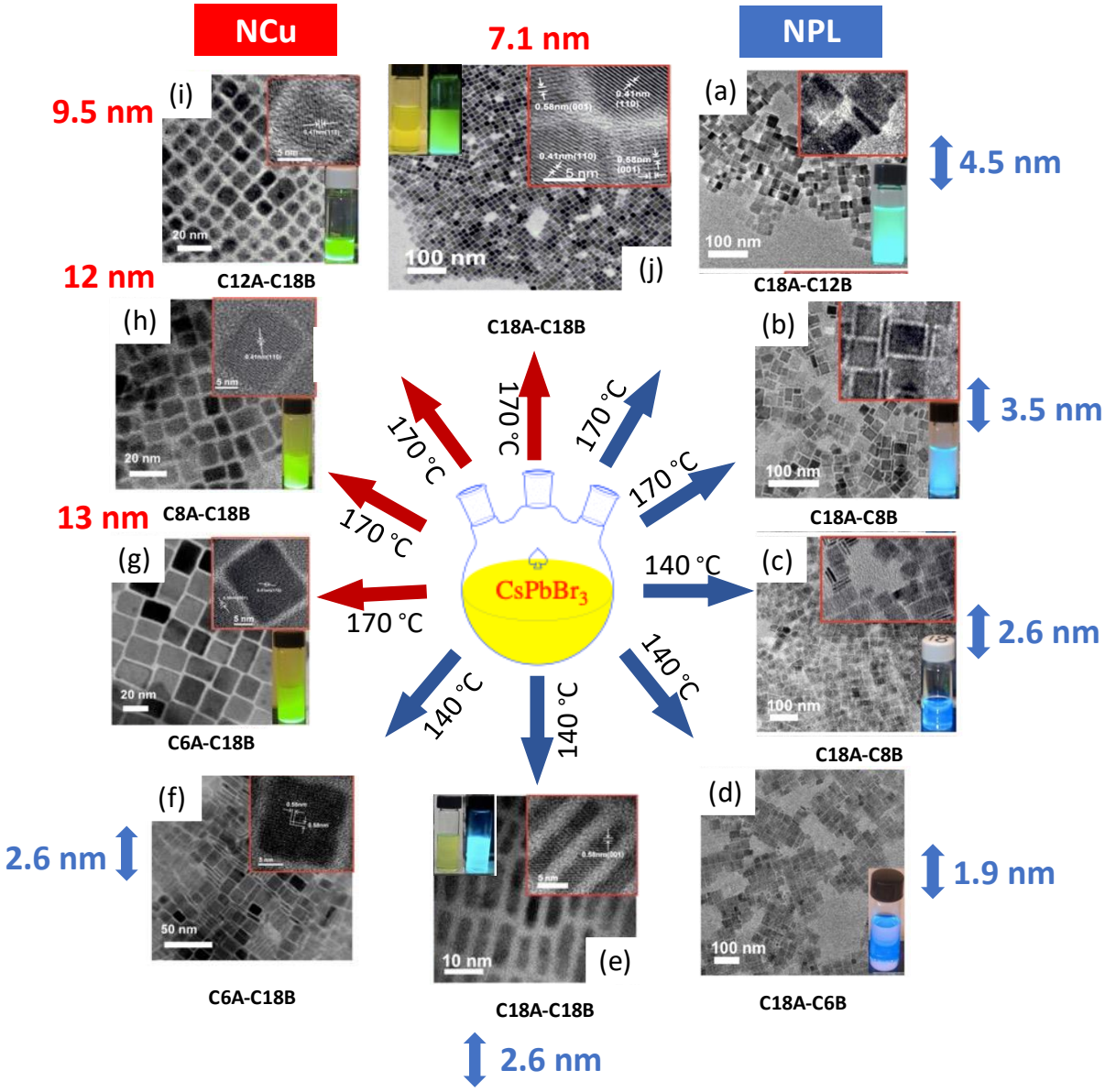


**Figure 2**. TEM and HRTEM images of $CsPbBr_3$ NPLs synthesized at 170 °C using C18A–C12B and C18A–C8B, and at 140 °C using C18A-C18B, C18A–C8B, C18A–C6B, and C6A-C18B. NCus synthesized using C18A-C18B, C12A-C18B, C8A-C18B, and C6A-C18B at 170 °C, with the insets of $CsPbBr_3$ NPLs colloidal solutions in hexane under UV light. Reproduced with permission [80], Copyright 2016 American Chemical Society.

The aging of $PbBr_2$ and Cs-oleate reaction, along with temperature and capping agents variation, yields $CsPbBr_3$ NWs and $CsPb_2Br_5$ NSs, making this method perfect for synthesizing NCs with different photophysical properties (Figure 3.a-f) [91, 92].

Versatile synthetic approaches demonstrated that Pb/Cs ratio determinates the phase purity of $CsPbBr_3$ synthesis: the copious amount of Cs leads to the formation of UV active $Cs_4PbBr_6$, while

the poor quantity of Cs results in the inhomogeneous cubic $CsPbBr_3$ NCs (Figure 3.g-i) [73, 75, 83, 93–95]. *Jing et al.* verified the influence of each Cs, Pb and Br on final product composition, by mixing variable amounts of cesium acetate, lead acetate, and tetraoctylammonium bromide (TOAB) in the amine-free environment. The authors found that the influence of bromide is weak compared to the Pb/Cs ratio, which determines the phase purity. In addition, the introduction of OAm results in strong coordination of $Pb^{2+}$ cations, causing their reduced availability, indulging the formation of $Cs_4PbBr_6$ (Figure 3.j-l). Simultaneously, it was revealed that bromide concentration dictates the mechanism of MHP synthesis through CsBr-seeded growth of $CsPbBr_3$ [96], indicating two possible paths of $CsPbBr_3$/$Cs_4PbBr_6$ evolution [97].

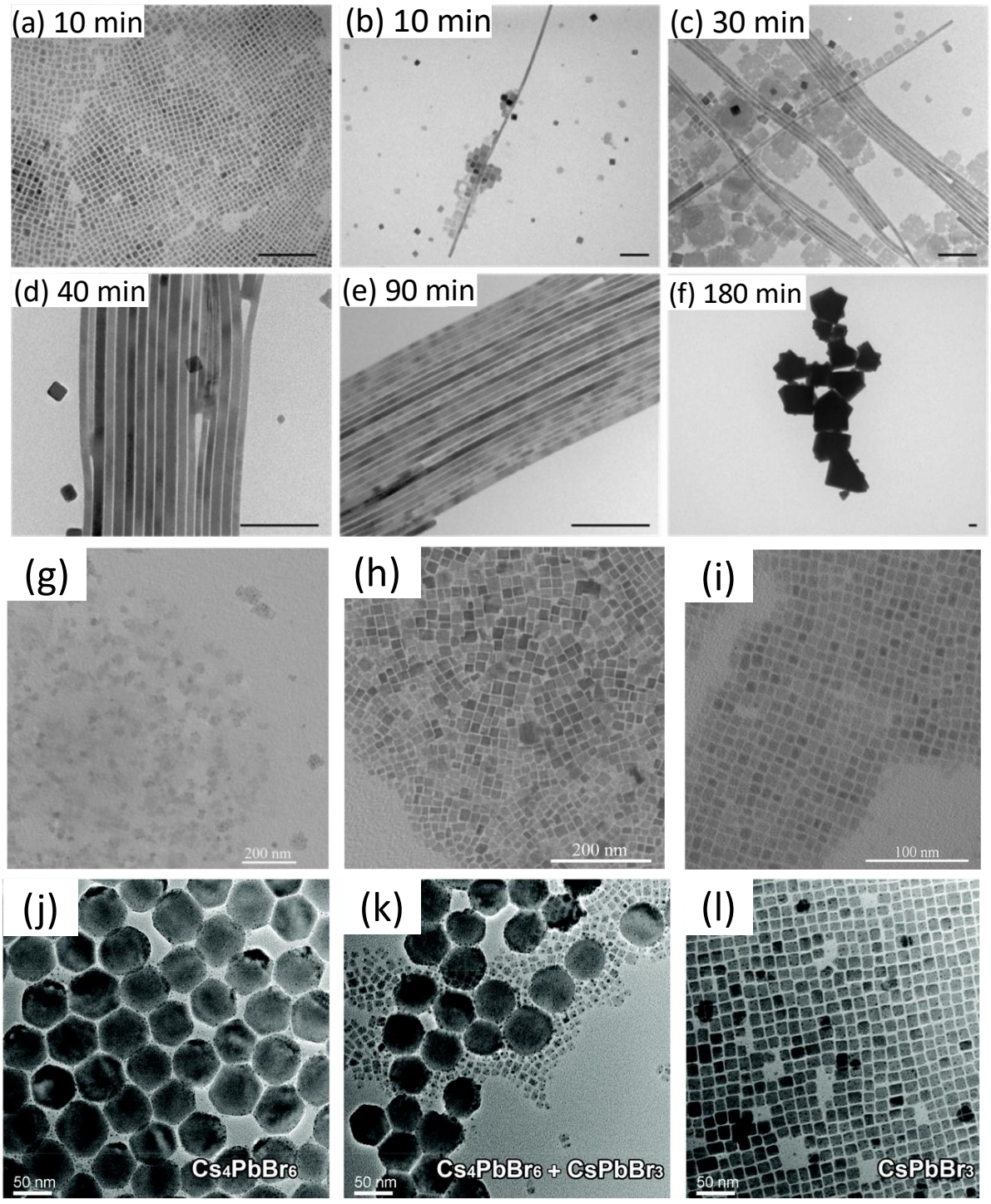


**Figure 3.** (a-f) TEM images of $CsPbBr_3$ NWs obtained at different reaction times. Scale bar corresponds to 100 nm. Reproduced with permission [91], Copyright 2015 American Chemical Society. (g) $CsPbBr_3/Cs_4PbBr_6$ mixture due to excess of Cs-oleate, (h) non homogenous $CsPbBr_3$ due to insufficient Cs-oleate and (i) homogeneous $CsPbBr_3$, respectively. Reproduced with permission [83]. Copyright 2017 Elsevier B.V. (j-l) $CsPbBr_3$ morphologies when the amount of Cs/Pb/Br was fixed at (a) 4–1–6, (b) 4–4–6, and (c) 4–6–6 mmol. Reproduced with permission [93], Copyright 2019 Royal Society of Chemistry.

It should be pointed that the aging of $CsPbBr_3$ seed-clusters at 230 °C results in the formation of polyhedron-shaped NCs that transform into hexapods with the addition of OAm-HBr solution (Figure 4.a-i). Polyhedrons and hexapods exhibit lower PL intensity compared to NCus, which makes them ideal for photocatalytic reactions [98]. Simultaneously, Bera et al, replaced $PbX_2$ with PbO and a-halo ketone i.e., phenacyl bromide, and found a synergic effect between phenacyl bromide and OAm forming tertiary amine upon aging at 180-220 °C, through successive nucleophilic substitution (SN2) reactions (Figure 4.j). Bulky tertiary amine has a key role in synthesizing multifaceted morphologies due to the stabilization of dodecahedron facets (Figure 4.k) [99]. The shaping control of these MHPs leads to self-organization and self-assembly that could be developed to synthesize periodic nanostructure (Figure 4.k and 4.i). Such a multifaceted synthetic approach could be beneficial for photocatalysis due to higher surface availability.

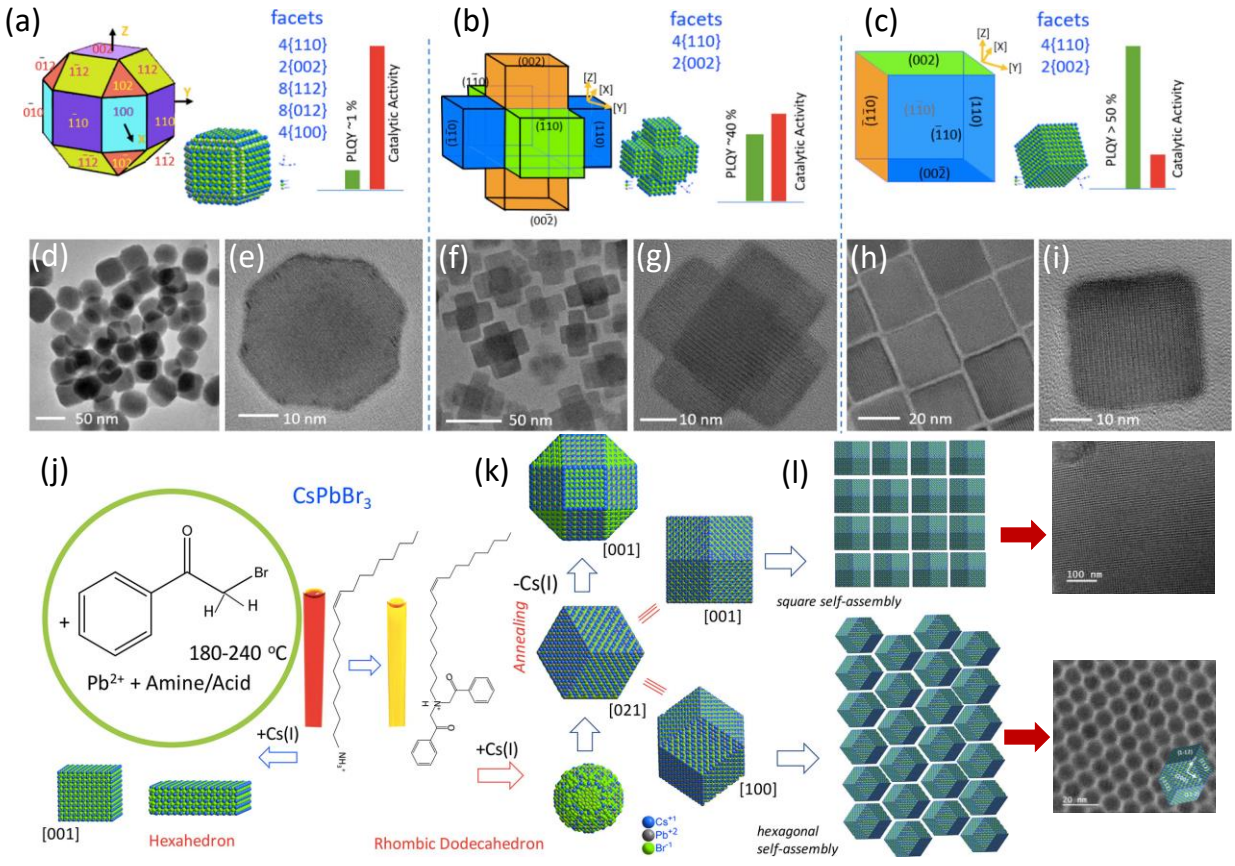


**Figure 4.** Schematic representation of (a) polyhedron, (b) hexapod, (c) cube-shaped MHPs, with their corresponding TEM images (d, e, f, g, h, i); (j) Schematic representation of multifaceted NCs synthesis using PbO and phenacyl bromide, and the synergic effect of phenacyl bromide and OAm forming tertiary amine upon aging at 180-220 °C upon immediate (red) and delayed (yellow) Cs injection, (k) nucleation of quasi-spherical dots, and formation of 12

faceted rhombic dodecahedron and 26 faceted rhombicuboctahedron, (l) Self-assembly patterns of dodecahedrons in square and hexagonal close packing. Reproduced with permission [98, 99]. Copyright 2020 American Chemical Society.

The hot-injection method provides well-dispersed and uniformed NCs, with controllable morphology, and it allows the direct synthesis of mixed halide perovskites. Nevertheless, it is a time-consuming method offering a very low yield. In light of what was previously discussed about ligand chain length, one should notice that the purity of OAm used in different studies varies from 70 % to more than 90 % [20, 84, 87, 96]. OAm can contain up to 43 % of its trans isomer, shorter chain, and unsaturated amines as well as oxygen-incorporated impurities [100]. Hence, replacing OAm would be one of the interests of ongoing research that will lead to scaling up MHP production for reproducible synthetic methods [101, 102].

### *2.1.2. Ligand-assisted reprecipitation (LARP) method*

The LARP is a room-temperature method involving the mixing and dissolving of CsX and $PbX_2$ (or their anionic mixtures) with OA and OAm in polar solvents, such as dimethyl formamide (DMF) and dimethyl sulfoxide (DMSO). Then DMF or DMSO solution is transferred dropwise in a non-polar solvent, such as toluene (Figure 5.a). Since the solubility of MHPs in toluene is lower than $10^{-7}$ g $mL^{-1}$, they recrystallize under stirring due to the supersaturation. This method produces NCus with a well-defined monoclinic crystalline phase, with sizes in the range of 9 to 13 nm. The LARP method provides surface self-passivation with halide anions leading to superior PLQY compared to the one obtained by the hot injection method [71]. Morphology can be engineered by varying reaction time and capping agent ratio [103].

An alternative approach aiming at pre-dissolving a mixture of $Cs_2CO_3$ and PbO in OA at 120 °C is proposed to avoid the use of polar solvents that can damage NCs, i.e. DMF and DMSO. Upon cooling to room temperature, toluene and OA are added to the reaction mixture, followed by ammonium-bromide injection, yielding uniform MHPs with an average size of 7.8 nm. More importantly, this method allows oleylamine free and gram-scale MHPs production, yielding a uniform size of 8.4 nm (Figure 5.b,c) [72]. The LARP method offers rapid MHPs preparation at ambient conditions with high PLQY, competitive to the time and energy-consuming hot-injection synthesis.

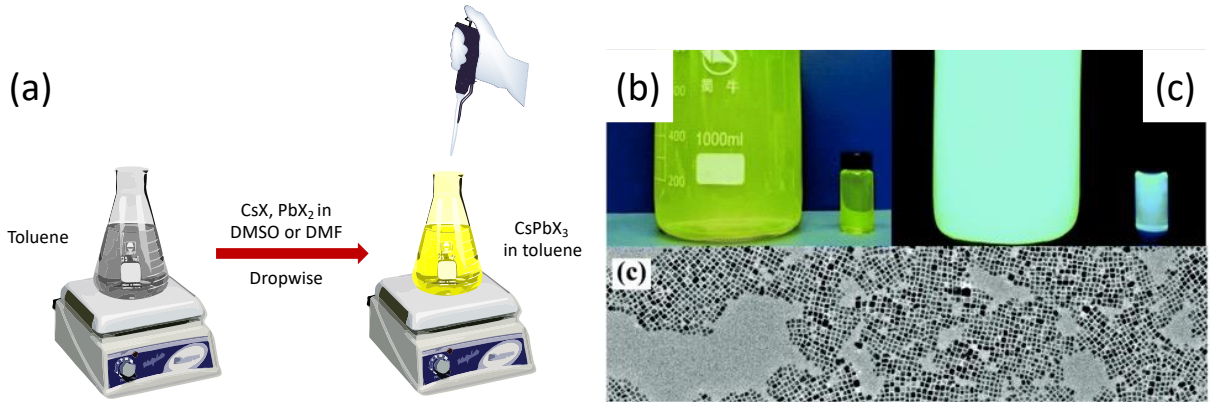


**Figure 5**. (a) Schematic representation of LARP method, (b) colloidal solution of gram-scale synthesis of $CsPbBr_3$ before and (c) after illumination under UV light. Reproduced with permission [72]. Copyright The Royal Society of Chemistry 2016.

### *2.1.3. Single-step microwave-assisted synthesis (MW)*

The MW method offers efficient, quick, and controllable preparation of $CsPbBr_{3-y}X_3$ nanocubes, nanoplates, and nanorods in only four to five-minute time due to its homogenous, selective, and high-rate heating [104, 105]. The reaction time under 800 W should not exceed 4-5 min at the risk of losing the uniformity of the NCs [61]. To the best of our knowledge, only a few research groups have explored this procedure and its advantages [57–61]. Under microwave, a quartz tube containing a mixture of CsOAc, $PbX_2$, trioctylphosphine oxide (TOPO), OA, OAm, and ODE is heated up to 160 °C under air, yielding orthorhombic nanocubes of ~10.8 nm (Figure 6.a). By decreasing the temperature to 80 °C, nanoplates could be formed, while the pre-dissolving of precursors leads to nanorod morphology. The morphology of $CsPbI_3$ can be tuned by varying Cs/Pb ratio (NRs), by replacing OA with octylamine (NWs), or by doubling ODE, OA, and OAm amount (NPLs) [58]. Raising the temperature above 160 °C leads to non-uniform size distribution and agglomeration due to OAm/OA poor chelating effect. The microwave-assisted method offers control of the heating rate, demonstrating increasing particle size from 10.8 to 15.1 nm when the heating rate is decreased from 28 to 12 °C $min^{-1}$. Slowing down the heating rate to 8 °C $min^{-1}$ leads to larger size NPs of 150 nm.

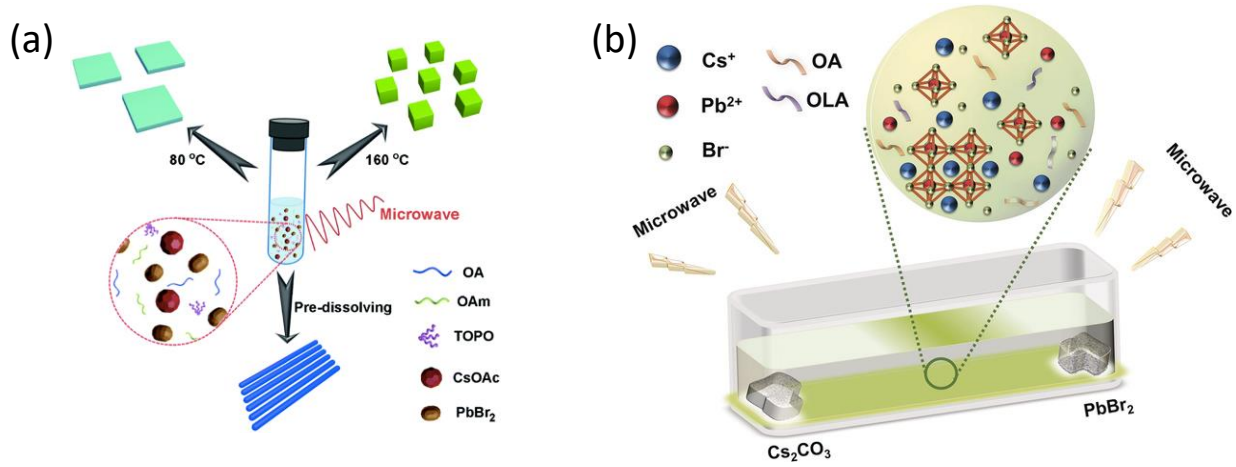


**Figure 6**. (a) Schematic representation slowed down MW-assisted synthesis Reproduced with permission [57]. Copyright 2018 Wiley-VCH Verlag GmbH &Co. KGaA,Weinheim. (b) Schematic representation of one-pot MW-assisted synthesis. Reproduced with permission [58]. Copyright The Royal Society of Chemistry 2017.

Slowing down the reaction rate while the reactants are separated on two different endings of the reactor, and a mixture of OAm, OA, and ODE is slowly poured into it, revealed the nucleation mechanism, confirming the formation of corner-sharing $PbX_6$ octahedra, being later stabilized by $Cs^+$ cations, so-called Lamer crystal growth (Figure 6.b). After 25 minutes, cubic well-crystalized $CsPbBr_3$ NCs are formed, with an edge length of 10-24 nm [57]. MW-assisted synthesis is a versatile method that offers the preparation of NCs with different morphologies and anion stoichiometry. It is an open-air and rapid method that produces uniform MHP with either monoclinic, orthorhombic, or cubic crystal lattice, owing to its highly controllable and rapid heating.

### *2.1.4. Ultrasonication synthesis method (US)*

The US method is a simple room temperature method that includes direct mixing of precursors ($Cs_2CO_3$, $PbX_2$, OAm, OA, and ODE/mineral oil) without any pretreatment and pre-dissolving, followed by direct tip sonication at the energy of 30 W for 10 minutes (Figure 7.a) [49]. The US method is adequately adapted for the synthesis of mixed $CsPbBr_{3-y}X_y$ perovskites (Figure 7.b). The average size of $CsPbBr_{3-y}X_y$ NCus obtained through the seeded mechanism is in the range of 8-20 nm. Variation of Cs/Pb ratio allows tuning of NPLs thickness. This method provides high PLQY, comparable to those obtained by the hot-injection method, at ambient temperature and open air, and it could be potentially scalable when the amount of each precursor is increased by

tenfold (Figure 7.c) [49]. Increasing the amount of precursors for the factor of 10, and extending the reaction time to 30 minutes yields the supercrystals of a few hundred nm size (Figure 7.d), exhibiting redshifted PL due to electron coupling caused by self-assembling (Figure 7.e) [63]. *Rao et al.* demonstrated the possibility of morphology and size control via capping ligands, ultrasound power (90-120 W), and reaction time adjustment, leading to the NCus, NPLs, NWs, and QDs. In another study, MHP NCus expressed enhanced photo- and thermostability (Figure 7.f,g) compared to NCs synthesized by room temperature LARP method, due to hydrophobic liquid paraffin used as a solvent, which protects NCs surface from moisture, oxygen, and halogen hydrogen bonding from oxidation [62]. Moreover, ultrasonication can control phase transformation, i.e., $Cs_4PbBr_6$ could be prepared using an excess of OAm under 40-minute-ultrasonication at 90 W [62]. It was also denoted that the immersion height of the tip should not exceed more than 20 % of the total liquid height for the best PLQY effect [106]. The US method allows the preparation of MHPs in polar alcohols such as butanol [107].

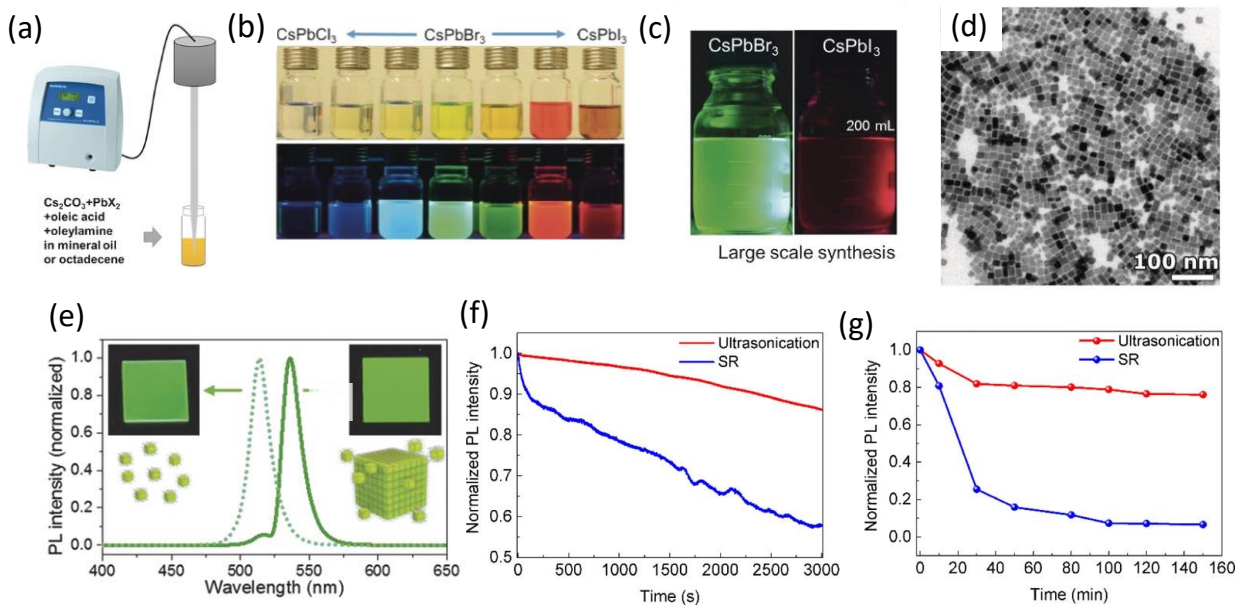


**Figure 7**. (a) Schematic representation of one-step tip sonication synthesis, (b) photographs of halide substitution reaction, and (c) large-scale synthesis, (d) TEM image of $CsPbBr_3$, Reproduced with permission [49], Copyright 2016 Wiley-VCH Verlag GmbH &Co. (e) PL spectra of individual and supercystals. Reproduced with permission [63], Copyright 2018 WILEY-VCH Verlag GmbH & Co. KGaA, Weinhei. (f) Photostability of $CsPbBr_3$ NCu colloidal solution under 365 nm continuous excitation, (g) thermostability of $CsPbBr_3$ NCu film at 80 °C, synthesized by ultrasonication (red) and at room temperature (blue). Reproduced with permission [62], Copyright 2018 American Chemical Society.

*2.1.5. Solvothermal synthesis (SV)*

The SV process is a fast and simple method aiming at dissolving precursors in a reactive medium and growing MHPs at elevated temperature and pressure. The pre-treatment of precursors (CsOAc, $PbX_2$, OAm, OA and ODE) before the reaction directs the morphology of MHPs. In the case where non-pre-treated precursors are inserted in the autoclave and heated up to 160 °C for 30 minutes under air, $CsPbBr_3$ and $CsPbI_3$ NCus are obtained with a size of 8.2 nm and 12.5 nm, respectively (Figure 8, a-e). Pre-dissolving precursors in ODE, yield orthorhombic green emitting $CsPbBr_3$, blue emitting $CsPb(Br/I)_3$, and $CsPb(Cl/Br)_3$ nanowires with strong quantum confinement (Figure 8.f-h) [67]. *Zheng et al.* demonstrated the formation of $CsPbX_3$ NPLs and NSs through the self-assembly of NRs. The thickness was controlled up to 1 μm by varying reaction time and mixing of long and short-chain ligands, under an inert atmosphere at 160 °C. The final MHPs displayed a relatively low PLQY of 20 % (Figure 8.i-q) [69].

Apart from NRs self-assembling, NPLs with outstanding tunable lateral size can be synthesized by either temperature variation (60-180 °C) or reaction time, providing NPLs with either extended or reduced lateral size, respectively [65]. It is worth noting that in both cases NPLs thickness remains constant (∼4.2 nm) [65].

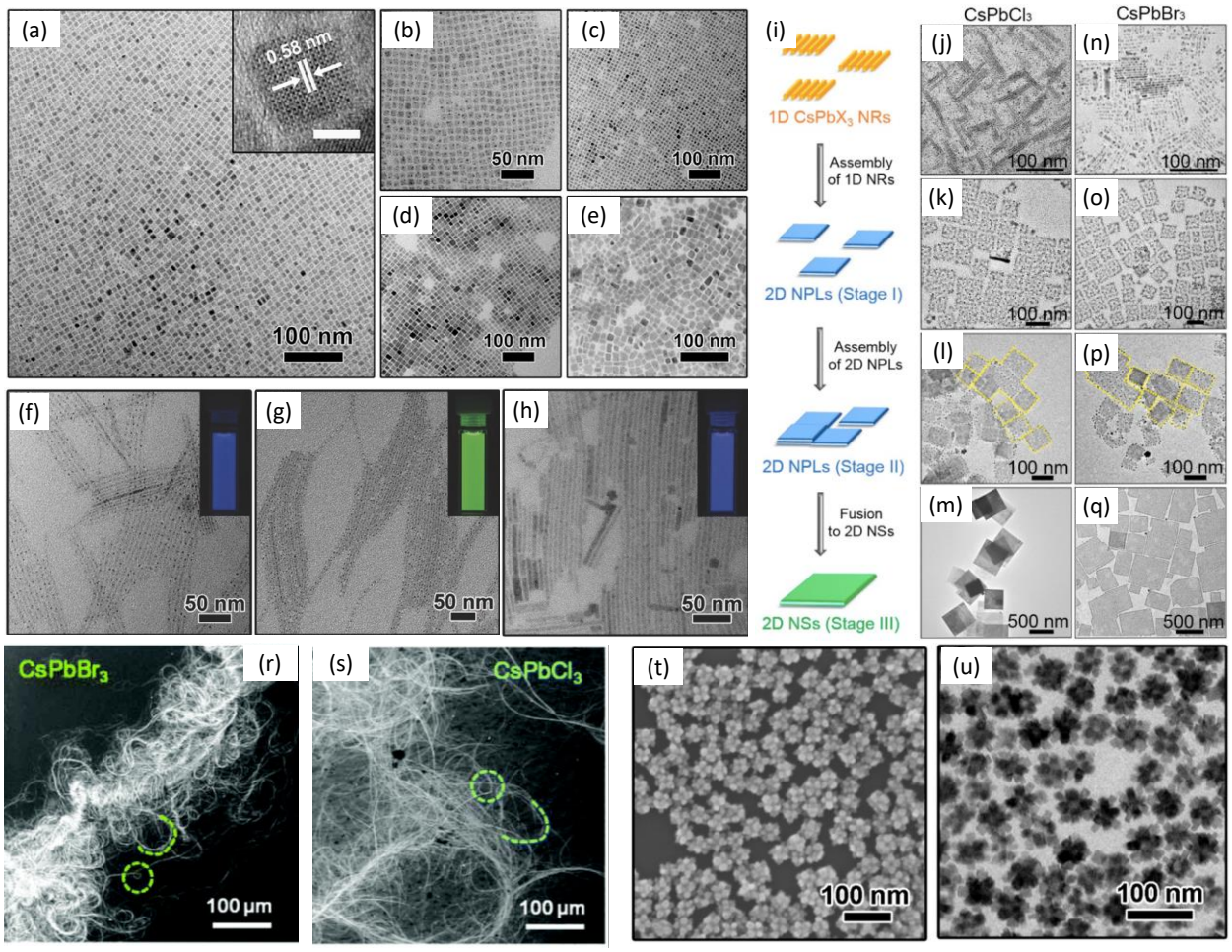


**Figure 8**. Morphology analysis of MHPs materials. TEM images of a) $CsPbBr_3$ and HRTEM (inset), b) $CsPbCl_3$, c) $CsPb(Cl/Br)_3$, d) $CsPb(Br/I)_3$ and e) $CsPbI_3$ NCus, f) $CsPbBr_3$, g) $CsPb(Br/I)_3$, and h) $CsPb(Cl/Br)_3$ ultrathin nanowires, with $CsPbX_3$ solution in hexane excited under UV illumination ($\lambda$ = 365 nm) (inset). Reproduced with permission [67], Copyright 2017 WILEY-VCH Verlag GmbH & Co. KGaA, Weinheim. (i-q) TEM images of $CsPbBr_3$ and $CsPbCl_3$ NPLs and NSs obtained through self-assembly of NRs. Reproduced with permission [69], Copyright 2018 American Chemical Society. (r, s) SEM images of ultrathin $CsPbB_3$ and $CsPbCl_3$ NWs with ultra-high aspect ratio. Reproduced with permission [66], Copyright 2018 The Royal Chemical Society. (t, u) SEM and TEM image of $CsPbBr_3$ nanoflowers. Reproduced with permission [70], Copyright 2018 Elsevier Ltd.

The impressive $CsPbB_3$ and $CsPbCl_3$ NWs with ultra-high aspect ratio could be obtained at 100 °C (72 h), when using pre-dissolved $PbX_2$ and $Cs_2CO_3$ as precursors, exhibiting PLQY of 75 % (Figure 8.r,s) [66]. The solvothermal method provides the possibility of designing nanoflowers under an inert atmosphere at 120 °C, through the seed-mediated mechanism, with PLQY of 50 % (Figure 8.t,u) [70]. The mechanism of nanoflower synthesis considers the formation of

rhombohedral $Cs_4PbBr_6$ seeds in a Cs-rich environment at the very beginning of the reaction due to faster dissolution of CsOAc than $PbBr_2$, following the complete transformation to the cubic $CsPbBr_3$ after 30-minute-long reaction. The SV method offers one-step synthesis providing NCs with versatile morphologies. However, it can be time-consuming compared to the previously described methods. Even though some reports present SV as a large-scale method, it is limited by the reactor volume, and it does not provide more than 0.2 g per batch of synthesis.

*2.1.6. Green synthetic procedures*

The development of green synthetic procedures is an essential step for scaling up MHP production. Such methods usually consider either solvent-free reactions, i.e., solid-state reactions, or green solvent approach. Finding a perfect eco-friendly procedure is an onerous task, and certain compromises must be taken into account, e.g., solvent-free synthesis requires considerable energy consumption and an inert environment. *Ng et al*. adapted the LARP method by replacing toluene and OAm with ethyl acetate and octylamine, respectively [108]. This approach reduces solvent waste by 62.5% and total ligand concentration by 60%, with an astonishing yield of 70% per reaction. Liu et al. reported the green solvent synthesis of $CsPbBr_3$ NCs in water, using organic building block, 2-methylimidazole (MEIM). The organic layer helps coordination chemistry by absorbing metallic precursors, favoring NCs synthesis. The ground $PbX_2$ and CsBr are immersed in MEIM aqueous solution and stirred for 3h. In such a way, $CsPbBr_3$/MEIM of 8-10 nm diameter size NCs were formed, displaying excellent photostability [78].

*Wang et al.* reported solid-state preparation of thermally stable $CsPbBr_3$ embedded in $Al_2O_3$ mesoporous matrixes, by mixing CsX, $PbX_2$, and Al-isopropoxide (AIP), followed by annealing at 800 °C for 10 min under nitrogen atmosphere (Figure 9.a). The carbonization of AIP at 800 °C produces a substantial amount of carbon, permitting MHP stability preservation. Subsequently, decarbonization is performed by calcination at 500 °C under an ambient atmosphere, achieving yellow $CsPbBr_3@Al_2O_3$ NCs. Without any purification, nanocubes could be achieved with a high PLQY of 70 % (Figure 9.b-d). Moreover, 500 g of $CsPbBr_3@$ $Al_2O_3$ could be obtained per one synthesis (Figure 9.e), being well crystallized, but not quantum-confined (Figure 9.f-h) [79]. The green and sustainable synthesis of MHP synthesis could also be advanced through the contribution of machine learning and robot-based high-throughput screening (HTS), i.e., automated synthesis [109, 110].

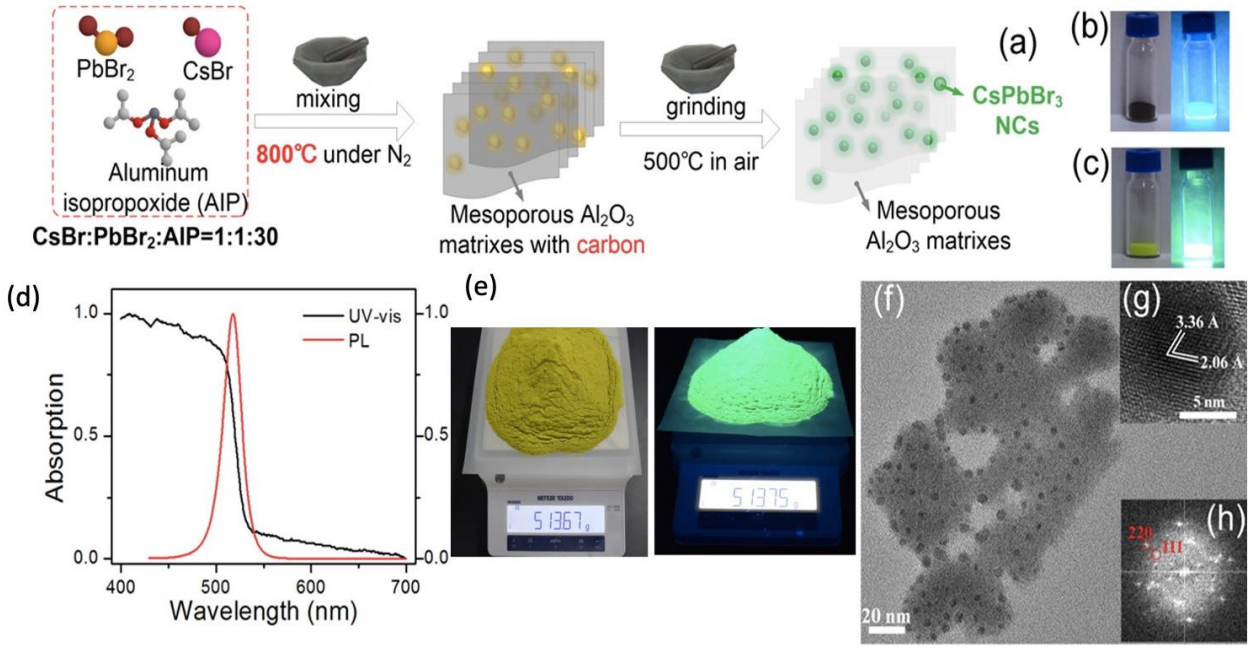


**Figure 9.** Large-scale production of $CsPbBr_3$@ $Al_2O_3$ powder. (a) Schematic representation of the high-temperature solid-state reaction synthesis. (b) Photograph of black powders after calcination under nitrogen atmosphere. (c) Photographs of final products after annealing under an ambient atmosphere. (d) Absorption and PL spectra. (e) Photography of $CsPbBr_3$@$Al_2O_3$ powder. (f) TEM image of $CsPbBr_3$@ $Al_2O_3$. (g) HRTEM image of one individual CPB NC, and (h) the corresponding Fast Fourier Transform image. Reproduced with permission [79], Copyright 2019 American Chemical Society.

### *2.2. Post-synthetic reactions and their influence on MHP's optical properties*

Different synthetic pathways yield cubic $CsPbBr_3$ nanocrystals, however, photoluminescence quantum yields and lifetimes, experience certain discrepancies. It is worth noting that purification has an important influence on PL [80].

The origin of the excellent optical properties of MHP lies in its intrinsic defect-tolerant electronic structure, stemming from the lack of bonding-antibonding interactions between conduction (CB) and valence band (VB) [111]. According to Kang and Wang simulations, the majority of intrinsic defects correspond to the shallow trap states, which do not contribute dramatically to the non-radiative recombination [111], rendering MHPs as highly defect-tolerant semiconductors with high PLQY (>90%) and suppressed PL blinking [112]. Moreover, they demonstrated that Br-rich conditions introduce high defect concentration, whereas moderate or Br-poor condition increases the energy formation of Cs, Br, and X vacancies, interstitial, and antisite defects above 1 eV [111].

Hence, when choosing synthetic conditions, one should refer to these findings in order to obtain high PL quantum yields and long PL lifetimes.

Herein, we will discuss various post-synthetic procedures and their influence on MHP's structural, morphological, and optical properties. Besides direct ionic exchanges, the presence of secondary phases such as $Cs_4PbBr_6$, and surface coating of MHPs could have a drastic impact on the optical properties of MHPs.

**Anion exchange reactions** have introduced an easy and rapid way of tuning MHP stoichiometry and the optical bandgap energy. Possible exchange reactions are Cl-Br-I or I-Br-Cl, but Cl/I perovskite cannot be obtained due to the difference in the atomic radii. Kovalenko and Manna's group were the first to report anion exchange upon MHP synthesis. Kovalenko's group used as the anion source $PbBr_2$, $PbI_2$, OAmX, and MeMgX previously dissolved in ODE at a higher temperature, then kept at 40 °C, followed by injection of MHP dispersed in toluene (particle size ~10 nm) [40]. Manna's group reported room temperature anion exchange using methylammonium bromide (MA-Br), octadecylammonium halides (ODA-X), OAmX, and tetrabutylammonium iodide (TBA-X) (particle size ~8-9 nm) (Figure 10) [113]. Mandal's group reported anion exchange with HCl and HI acid diluted in DMF (particle size ~11 nm) [52]. It should be noted that precursors with MA group could trigger Cs substitution, hence they should be avoided if the exchange of A cation is not the aim.

Despite the values varying from one direct method to another, they are very similar in proving unambiguously dramatic decay of PLQY with Cl prevalence in the structure, while Br/I mixtures express higher PLQY than pure $CsPbBr_3$, finally resulting in a high quantum yield for pure $CsPbI_3$ [60, 61]. However, anion exchange at room temperature demonstrated dramatic decay of PLQY, upon exchange of bromine with both chloride and iodine (Figure 10.c) [113], while anion exchange at 40 °C retained high quantum yields comparable to the direct synthesis [40].

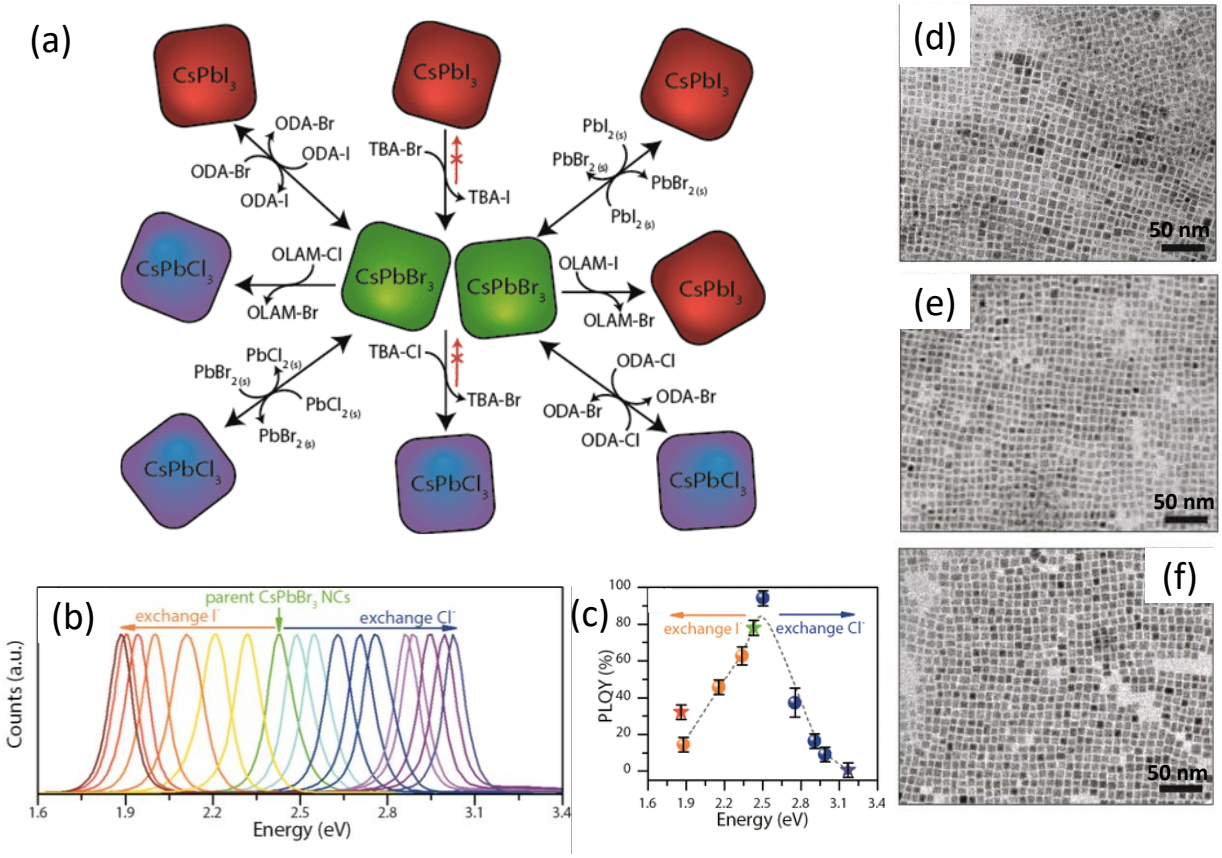


**Figure 10.** (a) Schema of anion exchange at RT with different precursors, (b) PL spectra of anion exchanged NCs, (c) PLQY recorded on the exchanged NCs (dots) as well as on the directly synthesized NCs (stars), TEM images of the anion exchanged (d) $CsPbBr_{3-y}Cl_y$, (e) pristine $CsPbBr_3$ NCs, (f) and anion exchanged $CsPbBr_{3-y}I_y$. Reproduced with permission [113], Copyright 2015 American Chemical Society.

**Cation exchange reaction** of Cs with MA was recognized in the above-mentioned reaction when MABr was used as a precursor for anionic exchange. Substitution of Cs with MA or FA organic moieties could be easily achieved; however complete substitution of B cation leads to distortion of $PbX_6$ octahedra and cubic crystal lattice. Partial substitution of Pb appeared to be successful, and it was achieved by metal bromide salts ($MBr_2$, M = $Sn^{2+}$, $Zn^{2+}$, and $Cd^{2+}$) dissolved in toluene in the presence of OAm, with preservation of the pristine size and shape (Figure 12.a-e), the main disadvantage of this method is a lack of MHP precipitation [53]. Partial substitution of Pb with divalent cations $Sn^{2+}$, $Zn^{2+}$, and $Cd^{2+}$ allows tuning of PL from 452 to 512 nm, with PLQY over 60 %, due to the change in the electronic structure upon creation of a shorter Pb-halide bond. Such lattice distortion leads to stronger interactions between Pb and halide orbitals, and consequently to the increased MHP band gap. It is worth noting that in the case of $Sn^{2+}$ partial substitution, observed PL and absorption fingerprints stem from $PbBr_6$, while the additional absorption band in

the red region corresponds to $SnBr_6$ octahedra (Figure 12.d) [53]. It is well known that $CsPbCl_3$ suffers from very low PLQY being less than 10 %, doping with $Cd^{2+}$ drastically enhances its PL features while keeping PL peak position and spectral width (Figure 12.e) [114].

Further MHP doping was achieved with $Cu^{2+}$, $Ni^{2+}$or $Co^{2+}$, resulting in PL enhancement (Figure 12.f-i) [41–45, 54–56]. Interestingly, nickel and copper at excessive dopant concentrations lead to PL quenching (Figure 12.g, i) [45, 56]. Such behavior indicates non-radiative electron transfer that could enhance the charge-carrier separation, allowing efficient photocatalytic reactions. Doping of $CsPbCl_3$ NCu and $CsPbBr_3$ NPLs with $Mn^{2+}$ causes the appearance of a new PL band in higher energy region, at ambient conditions (Figure 12.j, k) [60, 115, 116], while $CsPbBr_3$ NCus experience such emission only below 225K (Figure 12.f) [117].

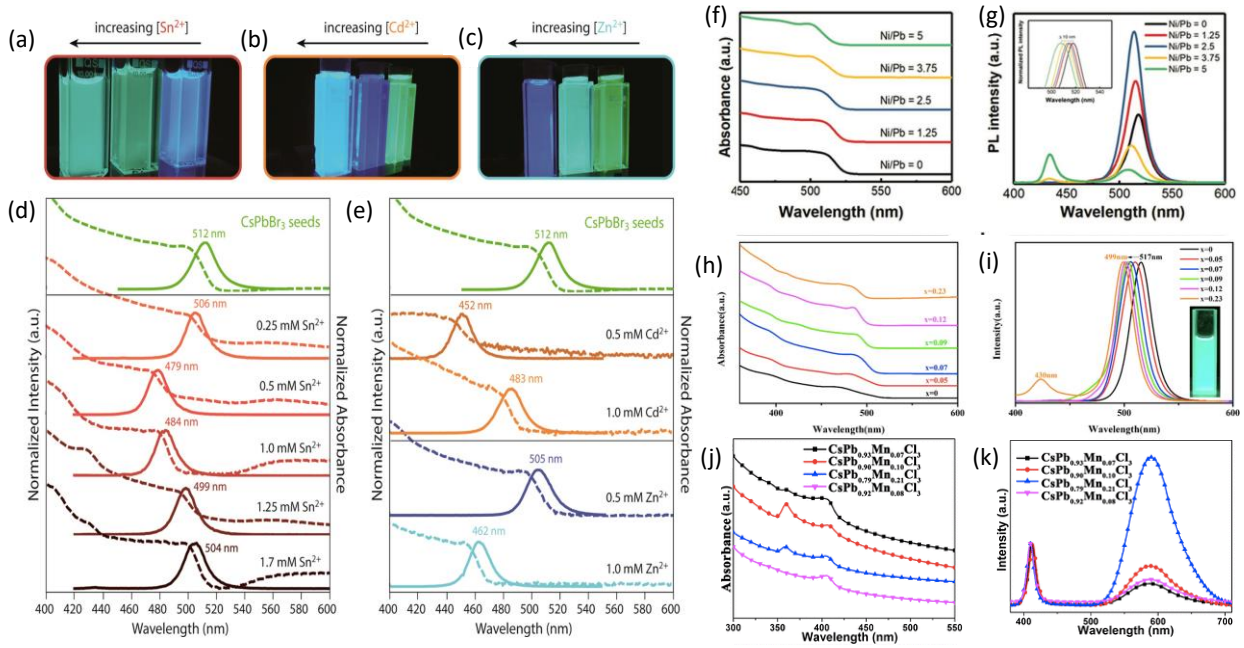


**Figure 11**. MHP doping with different transition metals, and their PL responses. (a-e) Partial substitution of Pb with Sn, Zn, and Cd in $CsPbBr_3$. Reproduced with permission [53], Copyright 2017 American Chemical Society; (f,g) $CsPbBr_3$ doped with $Ni^{2+}$. Reproduced with permission [45], Copyright 2021 Wiley-VCH GmbH; (h,j) $CsPbBr_3$ doped with $Cu^{2+}$. Reproduced with permission [55], Copyright 2019 American Chemical Society, and (j,k) $CsPbCl_3$ doped with $Mn^{2+}$. Reproduced with permission [60], Copyright 2017 American Chemical Society.

Apart from divalent doping, MHP could be modified by trivalent cations i.e., $Al^{3+}$, $Ce^{3+}$, or $Bi^{3+}$. A DFT study demonstrated that $Ce^{3+}$/$Bi^{3+}$ occupy either $Pb^{2+}$ anti- or interstitial sites in the MHP host lattice, at Br rich/moderate or poor condition, respectively (Figure 13.a-c) [47]. The $Bi_{Pb}$ antisite has a transition level energy at 0.59 eV and interstitial $Bi_i$ at 0.7 eV below conduction band

minimum (CBM), while $Ce_{Pb}$ and $Ce_i$ transition levels are located at 0.2 eV below CBM for both orthorhombic and cubic MHP host. These transition levels are known as the deep and shallow trap states introduced through the doping [47]. $Ce^{3+}$ shallow traps improved PLQY, which evolved from 41% to 89%, without influencing defect-tolerant properties [46–48]. On the contrary, doping with bismuth negatively affects photoluminescence due to the formation of the deep trap states (Figure 13.d, e) [47]. The $Ce^{3+}$ and $Bi^{3+}$ doping leads to the formation of shallow and deep traps, respectively. The formation of a shallow trap enhances the PL, which translates to higher recombination of photogenerated $e^-/h^+$, which could be detrimental to photocatalytic reaction. However, $Bi^{3+}$ doping generates a deep trap that lowers the charge carrier recombination, and induces a PL quenching and longer $e^-/h^+$ lifetime, which could lead to improved photocatalytic efficiency. In contrast, the same group reported that defects created in the $CsPbBr_3$ using in situ $Bi^{3+}$ doping using a hot-injection strategy lead to the formation of shallow defects (also known as trap states) with no modification of the bandgap structure [118]. The invalidity of the bandgap engineering using $Bi^{3+}$ doping was also reported by Miyasaka's group [48], indicating the formation of localized states. Further doping with aluminum results in blue-shifted luminescence of $CsPbBr_3$ and $CsPb(Br/I)_3$, with PLQY and PL lifetime being significantly decreased [119].

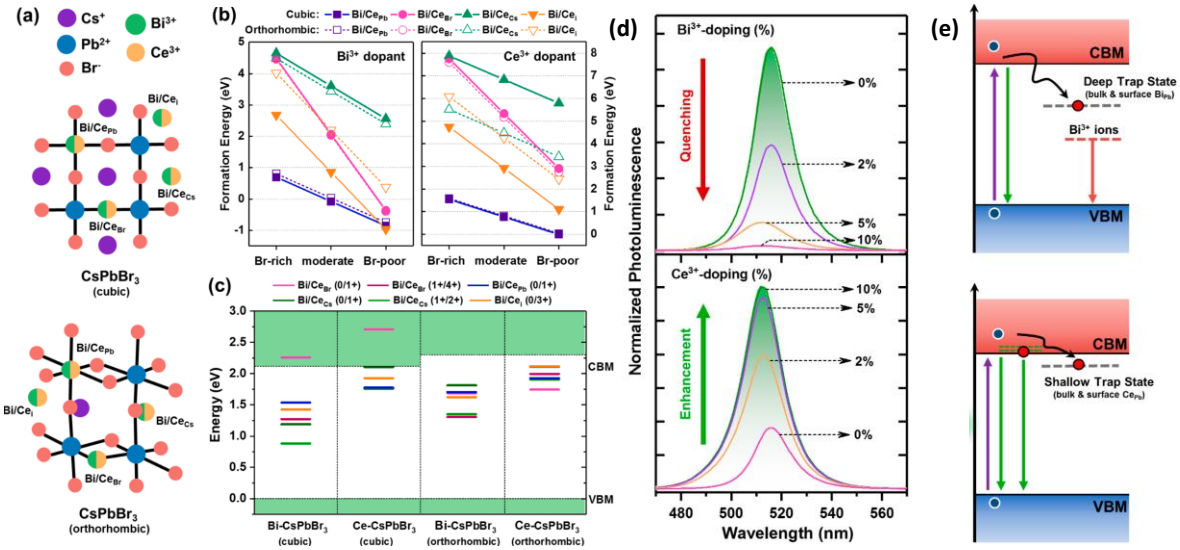


**Figure 12.** (a) Schematic representation of the cubic- and orthorhombic $CsPbBr_3$ crystal phase with $Bi^{3+}$ and $Ce^{3+}$ dopants at Cs, Pb, and Br sites ($Bi/Ce_{Cs}$, $Bi/Ce_{Pb}$, and $Bi/Ce_{Br}$) and with $Bi^{3+}$ and $Ce^{3+}$ interstitials ($Bi/Ce_i$), (b) calculated doping formation energies, and (c) doping charge-transition levels for $Bi/Ce_{Cs}$, $Bi/Ce_{Pb}$, $Bi/Ce_{Br}$, and $Bi/Ce_i$ in cubic and orthorhombic $CsPbBr_3$ crystal phase (HSE+SOC level of theory), (d) normalized PL spectra of $CsPbBr_3$ NCs upon $Bi^{3+}$ and $Ce^{3+}$ doping (2, 5, and 10 mole %), (e) and schematic representation of energetic diagrams

depicting the PL quenching/enhancing process in $Bi^{3+}$-doped and $Ce^{3+}$-doped $CsPbBr_3$. Reproduced with permission [47], Copyright 2019 American Chemical Society.

**Post-conversion of $Cs_4PbX_6$.** The synthesis of $Cs_4PbX_6$ is very similar to the hot injection method. Cs and Pb salts, together with OAm and OA, are dissolved in ODE at 150 °C and then cooled down to either 80°C, 100°C, or 60 °C for $PbBr_2$, $PbCl_2$, and $PbI_2$, respectively. Then Cs-oleate is quickly injected, and the reaction mixture becomes white. Depending on the desired size, the reaction is quenched by immersion in an ice-water bath for 0-10 minutes. In order to obtain MHPs, zero-dimensional $Cs_4PbBr_6$ are dispersed in toluene, and a solution of $PbBr_2$ is injected, leading to the formation of the $CsPbBr_3$ [73]. The same quenching principle can be applied in solvothermal reaction for the preparation of $CsPbBr_3$ NPLs, but also, $Cs_4PbX_6$ can be prepared by treatment of $CsPbBr_3$ with CsX [65]. MHPs can be also obtained upon calcination of $Cs_4PbX_6$ at 150-250 °C, however, conversion is not complete. It is rather a reaction with Prussian blue in a solution that succeeds full conversion [74], and water-triggered conversion in a two-phase hexane/water solution that yields MHPs (Figure 10.a) [75]. Due to the surface decorated with OH groups, the stability and PL properties of $CsPbBr_3$ are improved (Figure 10.b-d) [76].

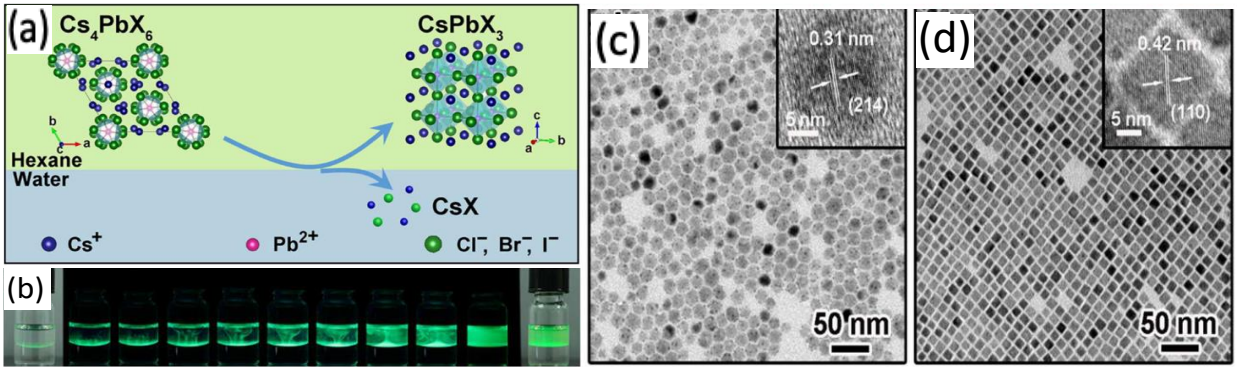


**Figure 13.** (a) Schematic representation of crystal structure and transformation process from $Cs_4PbX_6$ to $CsPbX_3$ upon water treatment. (b) Colloidal solutions of $Cs_4PbX_6$ to $CsPbX_3$ in hexane under UV illumination ($\lambda$ = 365 nm) during transformation. TEM and HRTEM (insets) images of (c) $Cs_4PbBr_6$ and (d) $CsPbBr_3$ NCs. Reproduced with permission [75], Copyright 2017 American Chemical Society.

The co-existence of the secondary phase significantly alters the PL quantum yield of MHPs, although the origin of $Cs_4PbBr_6$ green emission remain unclear. It is widely accepted that the green emission is a consequence of $CsPbBr_3$ traces, however, some studies are claiming defect-induced emission originates either from Br vacancies, polybromide, self-trapped excitons, or interstitial

hydroxyl [9]. According to Wang et al, there should be distinguished three different types of $Cs_4PbBr_6$-based materials: pure UV active non-emissive $Cs_4PbBr_6$ (P-$Cs_4PbBr_6$), defective-$Cs_4PbBr_6$ (D-$Cs_4PbBr_6$), and $CsPbBr_3$/$Cs_4PbBr_6$ hybrid (H- $Cs_4PbBr_6$), depending on their different structural and PL properties [9]. We will not focus on the intrinsic photoluminescent properties of $Cs_4PbBr_6$, but on its influence on charge carrier dynamics of $CsPbBr_3$. The impact of $Cs_4PbBr_6$ on photoluminescence can be understood through the temperature-dependent PL measurements (Figure 14.a-d) [120]. In the temperature range of 300 to 77 K, pure $CsPbBr_3$ films exhibit improved PL intensity as expected in such conditions: lower vibrational population in the crystal lattice results in less phonon-electron interactions, allowing recombination of charge carriers (Figure 14.e). The presence of $Cs_4PbBr_6$ impurities gives rise to the shallow trap states near the conduction band (Figure 14.f), which could be only thermally activated, leading to enhanced PL lifetime (Figure 14.g). These states are considered shallow since the minimum ionization energy, $k_bT$, needed for the electron de-trapping, is achieved at the ambient temperature.

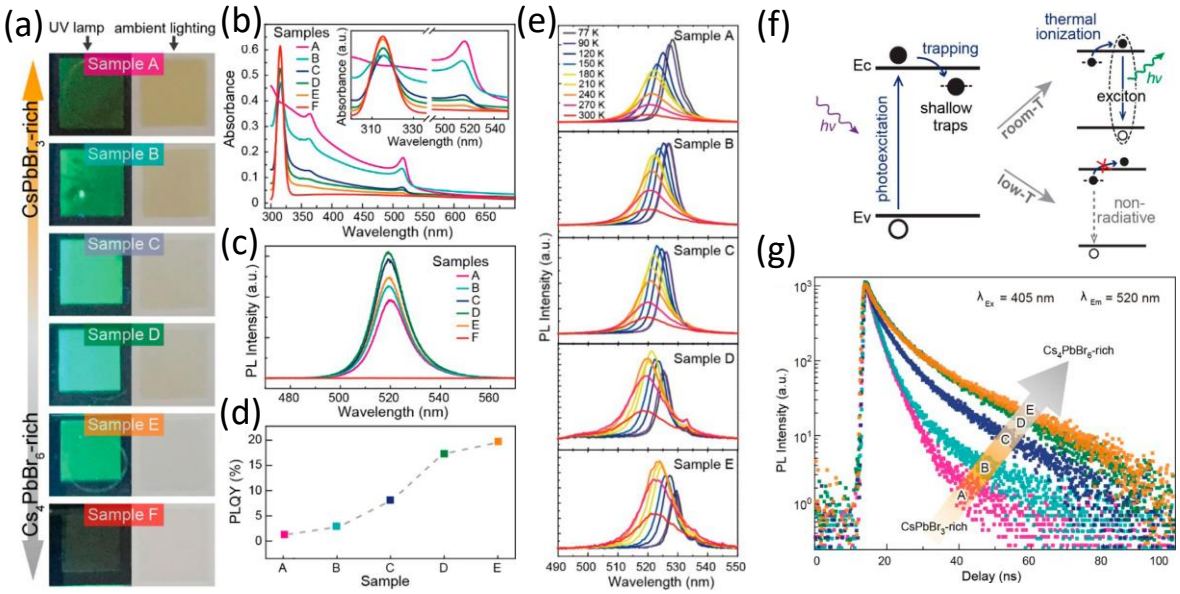


**Figure 14.** (a) Thin films of $CsPbBr_3$ with the increasing amount of $Cs_4PbBr_6$ (A-F); (b) absorption, (c) PL spectra, and (d) maximum PLQY for different samples (A-F); (e) temperature-dependent PL (f) schematic representation of trapping mechanism and (g) PL decay for samples (A-F). Reproduced with permission [120], Copyright 2017 American Chemical Society.

**Encapsulation of metal halide perovskites**. MHPs undergo severe damage due to the high sensitivity to moisture when submitted to UV light and they need to be protected from a highly humid environment [121]. A significant improvement of the MHPs stability has been achieved by crosslinking C=C double bond structure [49], organic ligands [20, 122], and polymer matrices [123], forming a hydrophobic coating. Thermal and humid resistance of $CsPbI_3$ was also achieved by Br doping and PTA organic cation surface passivation, leading to enhanced efficiency conversion.[124] Other strategies aimed at encapsulating MHPs in graphene oxide, $SiO_2$, $TiO_2$, and $AlO_x$, forming a protective shell [125–133]. The core-shell nanostructure showed higher stability in a humid environment. The $TiO_2$ shell coating was also proposed as a protective layer for the MHPs, exhibiting improved chemical stability, and remarkable (photo)electrochemical properties [132].

The encapsulation of $CsPbBr_3$ with different amorphous metallic oxides $MO_2$ (M = Ti, Si, Sn) allowed greater stability of MHP while preserving its morphological and structural properties [131, 133–135]. Encapsulation does not impact absorption spectral lines, except the $SnO_2$ coating layer that causes a blue shift in both absorption and PL spectra due to the chloride impurities in the commercially available $SnO_2$ precursor, forming $CsPbBr_{1-x}Cl_x@SnO_2$ (Figure 15.a-d) [135]. This approach enables a simultaneous core@shell structure design and optical band gap tuning. The shell is usually amorphous with a thickness of 1-3 nm (Figure 15.e-h). Due to the CB and VB alignment of $SnO_2$, $TiO_2$, and MHP, electron transfer from MHP to metallic oxide is possible, resulting in the photoluminescence quantum yield (PLQY) reduction from 37 % to 7 % ($TiO_2$) and 3 % ($SnO_2$) [134]. Silica acts as an insulating layer enhancing the radiative recombination and PL emission intensity, resulting in a quantum yield of 64 % versus 37 % for pristine $CsPbBr_3$. The reason behind such PL improvement lies in surface defect passivation. Besides amorphous $MO_2$ layers, attempts to encapsulate MHP in crystalline $TiO_2$ were successful (Figure 15.j-k). A core@shell crystalline structure formed upon calcination at 300 °C under argon, displayed enhanced stability (Figure 15.l-n) as well as superior photoelectrochemical properties [132].

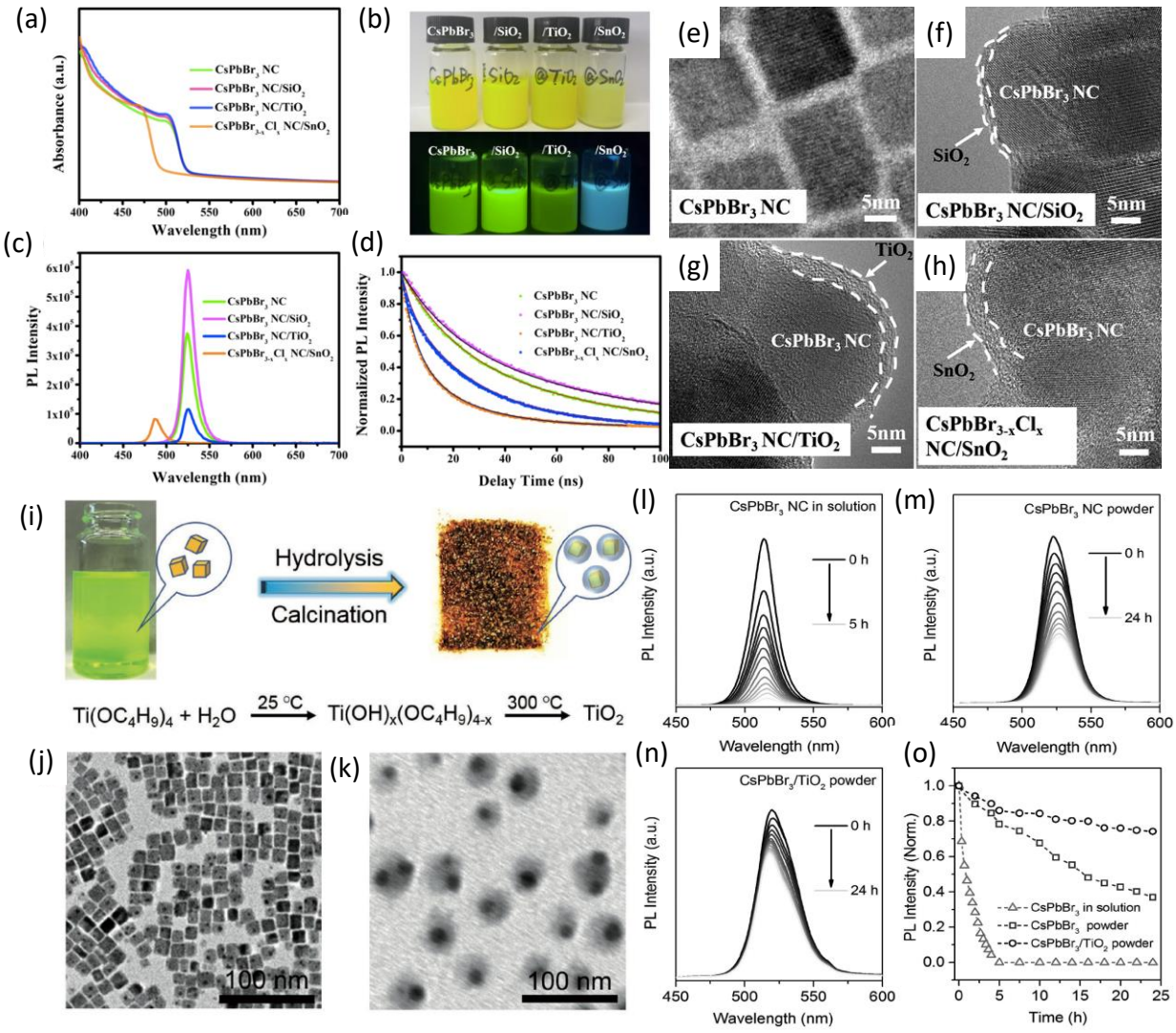


**Figure 15**. (a) UV–vis spectra, (b) sample photographs under day and UV light (λ = 365 nm) (c) PL spectra, and (d) time-resolved PL decay curves of $CsPbBr_3$ NC, $CsPbBr_3$ NC/$SiO_2$, $CsPbBr_3$ NC/$TiO_2$, and $CsPbBr_3$ NC/$SnO_2$. (e-h) TEM images of $CsPbBr_3$ NC, $CsPbBr_3$ NC/$SiO_2$, $CsPbBr_3$ NC/$TiO_2$, and $CsPbBr_{3-x}Cl_x$ NC/$SnO_2$. Reproduced with permission [134], Copyright 2018 American Chemical Society; (i) Schematic illustration of $CsPbBr_3$/$TiO_2$ core/shell NCs synthesis; TEM images of (j) $CsPbBr_3$ NCs and (k) $CsPbBr_3$/$TiO_2$ core/shell NCs after calcination at 300 °C for 5 h. Photostability of (l) $CsPbBr_3$ NCs in toluene, (m) $CsPbBr_3$ NCs powder, and (n) $CsPbBr_3$/$TiO_2$ NC powder under UV light by monitoring the relative PL intensity of the samples; (o) the comparison of relative PL intensity for the three samples. Reproduced with permission [132], Copyright 2017 WILEY-VCH Verlag GmbH & Co. KGaA, Weinheim.

## 3. Charge-carrier lifetime: transient absorption spectroscopy, time-resolved photoluminescence, and time-resolved microwave conductivity

The long carrier lifetime and long diffusion lengths exceeding to micro-scale are rendering MHP perfect for photovoltaics and photocatalytic reactions, where charge carrier separation is pivotal [136–138]. Hence, substantial research on MHP's photophysics has been conducted to understand the excited state, trapping, and recombination dynamics, by means of various techniques such as transient absorption (TAS), time-resolved photoluminescence (TRPL),[139] time-resolved terahertz spectroscopy (TRTS) [140–142], time-resolved microwave conductivity (TRMC) [143, 144], and two-dimensional electronic spectroscopy (2DES) [27].

Ultrafast spectroscopy i.e., TAS, is focused on the exciton dynamics and many-body interactions, i.e., biexciton effect, state filling, and Auger non-radiative recombination. TAS also provides information on carrier-phonon interactions, charge-carrier trapping, and exciton radiative recombination, further being complemented with TRPL. Charge-carrier diffusion and mobility could be investigated by techniques such as 2DES, TRTS, and TRMC. Along with previously mentioned experimental techniques, molecular simulation studies provide complementary information on carrier-carrier and carrier phonon interactions [145].

### 3.1. Ultrafast charge-carrier dynamics: transient absorption spectroscopy (TAS)

TAS is a powerful tool for the investigation of rapid carrier processes due to its adaptable set-up (e.g. two pump excitation, pump-push-probe, and circular polarized probe beam) that allows differentiation of symmetric and asymmetric biexcitons, the role of cold carriers, and exciton spin relaxation lifetime, respectively [146–148]. In general, pump-probe measurements shed light on hot-carrier intraband cooling dynamics in fs time scale exceeding to pico- and nanoscale, discerning trapping and recombination processes while considering quantum confinement [149], cation and anion type [150, 151], excitation energy and fluence dependence [152, 153].

Typically, TA spectra of $CsPbBr_3$ obtained on above-band-edge using 350 nm excitation wavelength consist of photoinduced bleach (PB1), so-called ground state bleach (GSB), which corresponds to the bend-to-bend exciton transition (Figure 16.a,b). At early delay times ($\Delta t \leq 1$ ps), PB1 signal is redshifted ($\delta_{xx}$) due to the formation of the biexciton [153]. Biexciton formation is a consequence of attractive Coulombic forces that bound two neutral excitons forming a biexciton [154]. Simultaneously with PB1, photoinduced absorption (PA2) at lower energies arises, representing a hot exciton cooling fingerprint, i.e., the intraband transition of the excited

state (Figure 16.a,b). PA2 could also be a signature of bandgap renormalization (BGR) [149], and a polaron formation in thin films [155]. High energy tail (PB2) could be assigned to either BGR or hot exciton bleaching [153]. Photoinduced absorption above the bandgap (PA1) arises from forbidden exciton transitions in strongly confined MHP, and bandgap renormalization in weakly confined/bulk MHP [152, 156]. After $\Delta t > 1$ ps, redshift and PA2 disappear, and only symmetric pronounced bleach is observed, representing continuum bleach due to the state-filling effect.

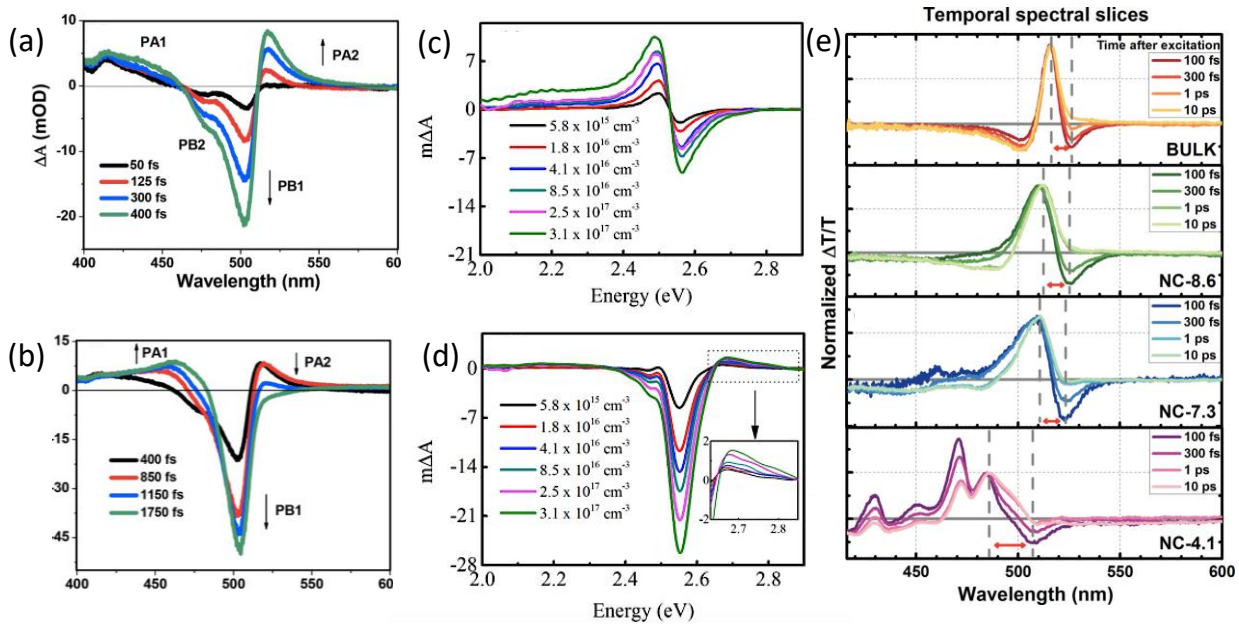


**Figure 16.** (a,b) Typical TA spectra of $CsPbBr_3$ obtained on above-band-edge using 350 nm excitation wavelength consisting of photoinduced absorption (PA1, PA2) and bleach (PB) at different delay time. Reproduced with permission [153], Copyright 2017 The Royal Society of Chemistry. (c,d) Influence of excitation fluence. Reproduced with permission [157], Copyright 2018 The American Physical Society, and (e) quantum confinement on spectral lines panel. Reproduced with permission [149], Copyright 2017 American Chemical Society.

High charge-carrier densities obtained at high excitations fluence (Figure 16.c,d) demonstrated bandgap renormalization in weakly confined/bulk MHPs, observed as broadening (Figure 16.c) of the bleach signal (high-energy tail), and PA1 band at the longer delay (Figure 16.d), which are attributed to shifting in the density of states upon BGR. Furthermore, high excitation fluences lead to slower charger-carrier relaxation due to the many-body interactions i.e. non-radiative Auger recombination, phonon bottleneck, and polaron screening [152, 158]. The right choice of the excitation energy successfully determines trapping processes in VB and CB discerning trapping states at low or high energy levels [153]. The effect of the quantum confinement on charge carrier

dynamics appeared to be important only for very small NPs, resulting in a multimodal bleach shape (Figure 16.e), whereas weakly confined NPs (> 7 nm) exhibit bulk-like photophysics [149]. Notably, the phonon bottleneck is independent of the size of NPs at higher excitation fluences [149]. *Li et al.* did not observe any multimodal GSB shape for NCs < 7nm, on the contrary, they demonstrate exciton relaxation through ligand-induced non-adiabatic relaxation mechanism in strongly confined $CsPbBr_3$, avoiding a hot bottleneck relaxation path [159].

A great deal of research was dedicated to cation and anion influence on the excited state dynamics. Cs-based halide perovskites showed slower hot-carrier dynamics than organic halide perovskite due to the reduced effect of electron-phonon couplings due to less dominant interactions between Cs and $PbX_6$ octahedra [151, 160]. Describing charge-carrier excited state dynamics upon anion substitution is more complex since the electronic values of the bandgap change. *Chung et al.* demonstrated slower charge-carrier cooling upon partial substitution of bromide with iodide, possibly caused by the change of density of states (DOS), suggesting that holes might contribute mainly to hot carrier relaxation. Simultaneously, *Mondal et al*. demonstrated the migration of holes from bromide to iodide, rendering iodide as a hole-trapping center. A partial substitution of Br with Cl has been quite investigated. However, the influence of Cl on charge carrier dynamics is still elusive. *Soetan et al.* demonstrated that the addition of Cl affects a decrease in BGR energy leading to bandgap narrowing, larger exciton binding energy, and reduced Coulombic interactions [161]. The addition of chloride resulted in a decreased Burstein-Moss effect compared to solely bromide-based MHP, which explains faster hot carrier cooling in mixed Br/Cl MHP. Moreover, at higher pump fluences (13-80 $\mu J/cm^2$) Auger recombination stands out as a dominant decay path, diminishing trapping assisted decay. In another study, *Mandal et al.,* at lower excitation fluences (<3 $\mu J/cm^2$), assigned faster carrier cooling to the near band edge trapping states introduced upon insertion of chloride in the crystal structure [162].

To the best of our knowledge**,** ultrafast charge-carrier dynamics of doped MHP have not been widely investigated, and there are only a few studies dealing with transient metal doping; such as Bi, Ni, and Mn [46, 163–165]. MHP doping with bismuth results in the Burstein-Moss effect since the conduction band is filled with additional electrons. Nanosecond TAS measurement showed slower bleach recovery (36 ns) compared to pure $CsPbBr_3$ (7 ns), implying a change in the electronic band structure that eventually leads to delayed carrier recombination. A slower intraband relaxation and more efficient charge transfer of doped MHPs in the presence of electron

acceptors was observed by fs-TAS, due to the increase of Gibbs free energy (-ΔG) [163]. Doping with nickel also slows down intraband relaxation, probably due to charge separation of the plasmon-MHP conduction band, where hot electrons are transferred at the interface [166]. In the case of Mn-doped $CsPbBr_3$ NPLs, a strong competition was observed between energy transfer and electron transfer. The TA spectra reveal an additional bleach, energetically lower than band bleach, corresponding to the charge transfer, while photoluminescence studies describe energy transfer from NPLs to Mn at a picosecond time scale [165].

### 3.2. Photoluminescence lifetime

Photoluminescence lifetime is essential to understand MHPs' photophysics on pico- and nanoscale. As previously stated, the high-temperature synthetic procedure proved that the prevalence of chloride in MHP results in reduced PLQY and lifetime, whereas the presence of bromide and iodide enhances QY and the PL lifetime (Figure 17.a) [20]. The MHPs obtained through high-temperature synthesis show drastically lower PL loss (10 %) [139] when heated in the range of 80-273 K compared to MHPs synthesized through the LARP method at room temperature (85 %) [71]. The average lifetimes calculated vary in different studies; note that NCs purification substantially affects PL lifetime, ranging from 1 to 112 ns [20, 61, 83]. One should take into account the anion substitution method, since, at room temperature, PL quenching occurs even in the presence of iodide [113].

The most compelling way to investigate the PL of MHPs is through temperature-dependent photoluminescence, which provides valuable information on short and long PL lifetimes, giving insight into trap-assisted nonradiative and radiative recombination. Temperature-dependent PL measurements showed that Cl-based MHPs suffer from PL loss even at $T < 300$ K, while $CsPbBr_3$ and $CsPbI_3$ exhibited higher resistance up to $T = 450$ K (Figure 17.b) [139]. The extended PL lifetime for $CsPbBr_3$ and $CsPbI_3$ is attributed to surface reactions that mostly originate from halogen vacancies and surface defects. TRPL measurements proved that $CsPbBr_3$ expresses a short PL lifetime at $T > 400$ K, due to thermally introduced nonradiative pathways. PL loss appeared to be reversible up to 450 K. Once this temperature is exceeded (> 450 K), the PL loss becomes irreversible. PL loss at elevated temperature could be due to increased anion mobility and ligand loss, which passivates the surface states.

.

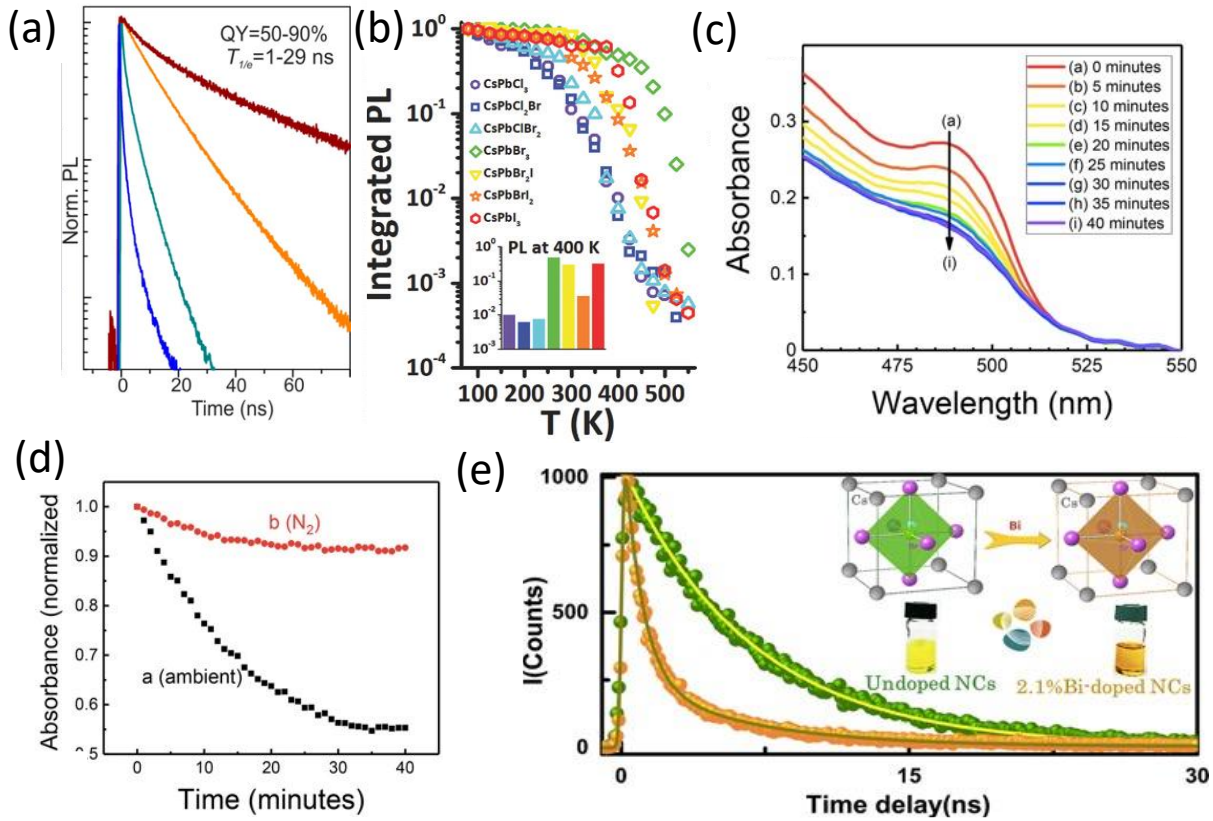


**Figure 17.** (a) Time-resolved PL lifetime from $CsPbI_3$ (red), $CsPb(Br/I)_3$, $CsPb(Br)_3$ to $CsPb(Br/Cl)_3$ (blue). Reproduced with permission [20], Copyright 2015 American Chemical Society. (b) Integrated PL evolution of MHPs containing Cl, Br, I, at different temperatures. Reproduced with permission [139], Copyright 2017 WILEY-VCH Verlag GmbH & Co. KGaA, Weinheim. (c) Absorption spectra of $CsPbBr_3/TiO_2$ films under white light continuous irradiation at ambient atmosphere, (d) normalized absorption of $CsPbBr_3/TiO_2$ recorded at 500 nm irradiated under ambient (black) and nitrogen (red) atmosphere. Reproduced with permission [121], Copyright 2018 American Chemical Society (e) Time-resolved PL lifetime decay of pristine $CsPbBr_3$ and Bi-doped $CsPbBr_3$. Reproduced with permission [163], Copyright 2016 American Chemical Society.

*Nenon et al.* evaluated the PLQY dependence on the concentration of surface halide defects in Br-poor conditions. Their findings showed that an increased concentration of halogen defects has little effect on $CsPbI_3$, moderate on $CsPbBr_3$, and substantial on $CsPbCl_3$ PLQY, meaning that the majority of defects originate directly from halide vacancies, since Pb vacancies would introduce the same effect to all $CsPbX_3$ NCs. Their ab initio calculations demonstrated that $CsPbCl_3$ consists of localized mid-gap traps that are responsible for trap-assisted nonradiative recombination, while $CsPbBr_3$ and $CsPbI_3$ consist of slightly localized electrons and completely delocalized holes,

resulting in higher PLQY. Surface passivation could enhance both PLQY and PL lifetime of $CsPbBr_3$ and $CsPbI_3$ through the exchange of hard oleate with soft carboxylates such as hexylphosphonate and benzoate, through the coordination of soft Pb binding sites with soft X-ligand carboxylates, while Cs vacancies are passivated with oleylammonium ligands [167]. *Hutter and Savenije* further investigated the mechanism of charge-carrier recombination in $CsPbI_3$ by means of temperature-dependent TRMC. The authors demonstrated that charge-carrier mobility and recombination dynamics in $CsPbI_3$ and $MAPbI_3$ are only limited by phonon scattering. In other words, MHPs' charge-carrier dynamics strongly depend on the $PbI_6$ framework, being completely independent of the A cation type. What is more, their findings indicate thermally enhanced second-order recombination, which could be a signature of an indirect recombination pathway [143].

Although the presence of chloride is considered non-beneficial for photoluminescence, it could slightly improve PL lifetime when added in small amounts to the mixed Br/I perovskite. In such a way, chloride becomes a lead defect ($V_{Pb}$) healer when added in small quantities, acting as a hole repellent, further reducing trapping and enhancing PL [168]. As previously stated, photoluminescence lifetime could be improved in the presence of $Cs_4PbBr_6$ impurities (Figure 14), and doping with different metals, such as Ni, Cu, Co, and Ce, that are discussed above. A more detailed discussion on the $Cs_4PbBr_6$ phase is given in the previous chapter and a detailed review by *Wang et al* [169].

From the photocatalytic point of view, long-lived charge carriers are needed for optimal and efficient photochemical reactions. Assuming that the reactions occur at the μs scale, quenching the PL signal could be interpreted as a non-radiative phenomenon, thus beneficial for charge carrier separation and their lifetime. PL lifetime could be manipulated through an adjusted synthetic approach previously discussed, i.e., room-temperature synthesis, multifaceted morphology, doping with metallic cations, and coating with appropriate semiconductors forming core@shell nanostructure [121, 132]. In the case of coupling with $TiO_2$ as a semiconductor, the electron transfer from MHP to $TiO_2$ enhances charge-carrier separation. Interestingly, a thin $TiO_2$ layer could favor a Z-scheme electron transfer when optimal VBM and CBM are well adjusted, enhancing PL signal [169]. An efficient electron transfer occurs when nanostructures are excited under an inert atmosphere, avoiding electron capture by oxygen, which causes the accumulation of charges, leading to the corrosion of MHP (Figure 17.c,d) [121]. The MHPs doping is another way of suppressing PL by directly influencing electronic band structure. So far one of the most

interesting dopants is bismuth, which can significantly suppress PL even at very small amounts (Figure 17.g) [163]. In addition, PL lifetime can be diminished by Zn, Cd, Sn, Al doping and excessive amounts of Ni and Cu [45, 53, 56].

### 3.3. Charge-carrier diffusion lengths in $CsPbX_3$

MHPs are known for their long carrier diffusion length ($L_D$) exceeding > 9.2 μm [140]. A direct study performed by scanning photocurrent microscopy (SPCM) on the single crystal of $APbX_3$ (A = MA, FA, Cs, X = Br, Cl, I) revealed that Cs-based halide perovskites experience $L_D$ at the micrometer scale, however shorter than their organic counterparts. The diffusion lengths $L_D$ decrease in the order MA > FA > Cs, where the difference between MA and Cs is 50 %. Interestingly, unbalanced diffusion of electrons $L_D^{e-}$ and holes $L_D^{h+}$ in all $APbBr_3$ nanocrystals appeared to be of one order of magnitude difference between $L_D^{h+}$ (cc. 10-50 μm) and $L_D^{e-}$ (cc. 1-5 μm) in $APbBr_3$ (A = MA, FA, Cs) nanocrystals.

It is important to note that $L_D^{h+}$ of $MAPbBr_3$ and $MAPbI_3$ do not depend strongly on halide type, whereas $L_D^{e-}$ are strongly dependent on anionic substitution. $MAPbBr_3$ experienced five times smaller $L_D^{e-}$ and 1.3 times smaller $L_D^{h+}$ than $MAPbI_3$. This behavior was confirmed by indirect TRMC measurements. These results are of great significance for the best choice of photocatalyst and solar cell efficiency [27].

## 4. Photocatalytic applications of metal halide perovskites

Designing an efficient photocatalyst with a suitable bandgap energy potential for hydrogen evolution remains a challenge. Hydrogen is considered as a promising chemical fuel, and studies are ongoing considering its production and storage [170–172]. Besides hydrogen production, $CO_2$ reduction, and degradation of organic molecules have been gaining tremendous interest in the photocatalytic community. The main obstacle to the employment of MHPs in photocatalysis is their inherent instability in polar solvents, and upon exposure to UV irradiation, which enhances the interactions between MHP (e.g. $CsPbBr_3$), $CO_2$, $O_2$, and $H_2O$, resulting in PbO formation (i.e. anodic corrosion) (Eq. 5,6) [173]:

$$2CsPbBr_3 \cdot H_2O + 0.5O_2 + CO_2 \rightarrow 2CsBr + PbCO_3 + Pb(OH)_2 + 2HBr + Br_2 \quad (5)$$

$$Pb(OH)_2 \rightarrow PbO + H_2O \quad (6)$$

The least stable cubic iodide-based MHPs (e.g. $CsPbI_3$) retain their structural properties only at temperatures above 645 K, and suffer from quick phase transition, resulting in a so-called yellow non-perovskite phase (δ-orthorhombic $CsPbI_3$ nanocrystals), which limits their application [19, 174, 175]. In order to protect MHPs, a straightforward approach considers covering MHPs with a stable and robust overlayer, which would act as a barrier, preventing direct contact with the surrounding media, simultaneously allowing charge diffusion. What is more, polar medium can be substituted with either less polar or non-polar medium (e.g., ethyl acetate) allowing their wider application [176].

The photocatalytic performances of these materials have been intensively explored. The studies showed effective enhancement of the photocatalytic efficiency for $CO_2$ reduction when inorganic MHPs (e.g. $CsPbBr_3$) were coupled to graphene oxide  titanium dioxide,[133] zeolite [177], and $Re(CO)_3Br(dcbpy)$ (dcbpy = 4,4'- dicarboxy-2,2'-bipyridine) complex molecule as the active material [178]. The heterojunction improves the efficiency of charge-carrier photogeneration (i.e. electron-hole separation) and $CO_2$ capture. Mixed metal halide perovskite $CsPb(Br_{0.5}/Cl_{0.5})_3$ demonstrated the effective removal of $CO_2$ from ethyl acetate saturated solution [176]. Several methods have been proposed to enhance the stability and, thus, the photocatalytic activity of MHPs for $CO_2$ reduction [179], $H_2$ generation [180], and toluene/ benzyl alcohol oxidation [181]. Herein, we will introduce some efficient strategies to boost the photocatalytic performance of MHPs, including surface and morphological modifications, doping with metals, and encapsulation with non-toxic and stable oxides such as $TiO_2$ and $SiO_2$.

### 4.1. Surface and morphological modifications of metal halide perovskites

Typically, $CsPbBr_3$ nanocrystals are prepared by ionic metathesis, which considers the injection of Cs-oleate into the solution of $PbBr_2$ in oleic acid (OA), oleylamine (OAm), and octadecene (ODE), at elevated temperature. In the preparation of metal-halide-perovskite nanocrystals, capping ligands are indispensable for colloidal stability and shape control. However, long alkyl-chain capping ligands used in conventional MHP NCs synthesis (e.g., OAm and OA) are unfavorable for $CO_2$ adsorption, since they hinder the efficient carrier separation on the surface of MHP NCs and thus reduce the photocatalytic activity [182]. To meet these challenges, employing small organic molecules as capping ligands could be an ideal solution. *Ying Xu et al,* functionalized $CsPbBr_3$ NCs with short-chain glycine molecules ($CsPbBr_3$-Gly) and compared their

photocatalytic performance in $CO_2$ reduction reaction ($CO_2RR$) with $CsPbBr_3$ NCs functionalized with long-chain OA and OAm ligands ($CsPbBr_3$-OA/OAm) [183]. $CsPbBr_3$-Gly NCs were prepared by simple ligand exchange of as prepared $CsPbBr_3$-OA/OAm upon adding to a saturated solution of glycine (Figure 18.a, insert). $CsPbBr_3$-OA/OAm NCs show a poor photocatalytic activity for $CO_2$ reduction in water, with CO formation rate of 4.8 μmol $g^{-1}$ $h^{-1}$. However, $CsPbBr_3$-Gly NCs exhibit an excellent yield with CO generation rate of 27.7 μmol $g^{-1}$ $h^{-1}$, being 5 times higher than that of $CsPbBr_3$-OA/OAm, with reproducible yields for three consecutive cycles. The enhanced photocatalytic performance of $CsPbBr_3$-Glycine NCs could be mainly attributed to the reduced hindrance of short-chain ligands, together with the strong interaction of glycine with $CO_2$ [183]. Moreover, replacing OA and OAm with glycine leads to a significantly higher photocurrent density compared to $CsPbBr_3$-OA/OAm NCs (Figure 18b), demonstrating enhanced charge-carrier separation of $CsPbBr_3$-Gly. From the EIS Nyquist plots, one can observe a smaller semi-circle for $CsPbBr_3$-Gly, indicating significantly lower charge transfer resistance (Figure 18c) [183].

The conventional OA could be also replaced by a shorter acetic acid, after the treatment of $CsPbI_3$ with methyl acetate. The obtained MeAc-$CsPbI_3$ proved to be more active in photocatalytic polymerization of 3,4-ethylenedioxythiophenereaction in nonpolar solvents (toluene and dichloromethane) than pristine $CsPbI_3$. The increase of photoactivity was attributed to an improvement in the charge transport, originating either directly from OA replacement or from introduced surface defects [184].

Morphology tuning is one strategy that has been proposed to improve the photocatalytic activity, assuming that the charge ($e^-/h^+$) separation and photocatalytic reactions are driven by the facet orientation. The multifaceted NCs could be an excellent strategy for efficient adsorption/desorption of reactants/products. Nanocrystal morphology modification could increase the number of active sites and boost the photocatalytic performance of $CsPbX_3$. Multifaceted polyhedron six-armed hexapods, and conventional six-faceted $CsPbBr_3$ NCs demonstrated an interesting photocatalytic activity in $CO_2$ reduction reactions (Figure 18.d) [179]. Among these, six-faceted nanocrystals showed the lowest catalytic activity for $CO_2$ reduction, with the maximum yield of CO and $CH_4$ being 16.4 and 7.4 μmol $g^{-1}$, respectively. The hexapod structure exhibited medium photocatalytic activity, while the polyhedron $CsPbBr_3$ NCs with 26 facets indicated the strongest photocatalytic activity among the three structures yielding 130.7 and 58.8 μmol $g^{-1}$ of CO and $CH_4$, respectively. This confirmed that charge-carrier separation is more efficient in

multifaceted $CsPbBr_3$ nanocrystals than in standard six-faceted cube nanostructures. Cube-shaped nanostructures showed efficient carrier recombination with high PLQYs (> 50 %). However, the charge carriers in multifaceted structures were trapped and resulted in poor emission with PLQY ~ 1 %, demonstrating enhanced photocurrent and lower charge-carrier resistance (Figure 18.e,f) and enhanced photocatalytic performance [179].

In addition to multifaceted MHPs, 2D structures exhibited unique advantages, including increased stability in aqueous systems, abundant active sites for $CO_2$ reduction, and reduced bulk recombination [185]. The 2D $CsPbBr_3$ nanosheets possess a higher bandgap than nanocubes, revealing stronger driving forces that trigger the reduction of $CO_2$ to CO, and $H_2O$ to $O_2$ (Figure 18.g). The $CsPbBr_3$ nanosheets with a thickness of 4 nm exhibited high photocatalytic activity in $CO_2$ reduction, with a CO formation rate of 21.6 μmol $g^{-1}$ $h^{-1}$, which is 3.8 times higher than that of $CsPbBr_3$ NCs (5.7 $\mu$mol $g^{-1}$ $h^{-1}$) (Figure 18.h) [185]. High photocurrent density further reinforces 4 nm $CsPbBr_3$ NSs photocatalytic performance, indicating significantly higher charge-carrier separation compared to NCs, and NSs with different thicknesses, i.e., 2, 3, and 4.6 nm $CsPbBr_3$ (Figure 18.i). The 2D $CsPbBr_3$ demonstrated excellent stability and performance for up to 30 h (Figure 18.j).

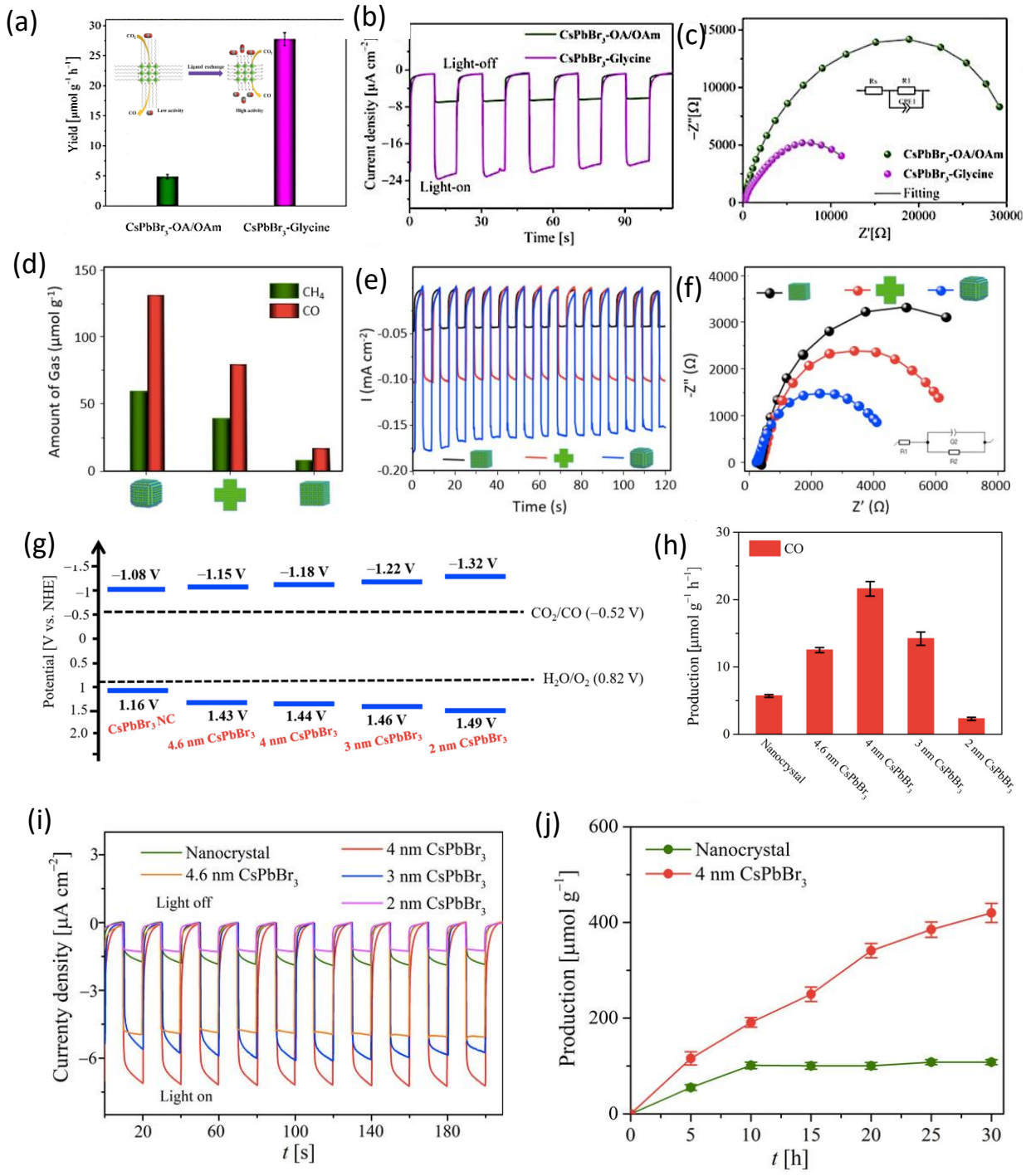


**Figure 18**. (a) Photocatalytic evolution of CO generated upon $CO_2$ reduction with $CsPbBr_3$-OA/OAm and $CsPbBr_3$-Gly NCs as the photocatalysts, and ligand exchange in $CsPbBr_3$ (insert), (b) I-t curves at a bias potential of -0.4V (vs. Ag/AgCl), and (c) EIS Nyquist plots of $CsPbBr_3$-OA/Oam and $CsPbBr_3$-Gly. Reproduced with permission [183], Copyright2020 Wiley-VCH GmbH (d) $CH_4$ and CO evolution during $CO_2$ reduction reaction using multifaceted polyhedron, six-armed hexapods, and conventional six-faceted $CsPbBr_3$, (e) I-t curves and (f) EIS Nyquist plots of the multifaceted polyhedron, six-armed hexapods, and conventional six-faceted $CsPbBr_3$. Reproduced with permission

[179], Copyright 2020 American Chemical Society. (f) The schematic illustration of band structures of $CsPbBr_3$ NCs and $CsPbBr_3$ NSs, (g) The comparison of CO production with $CsPbBr_3$ NCs and $CsPbBr_3$ NSs as photocatalysts. (h) I–t curves of $CsPbBr_3$ NCs and $CsPbBr_3$ nanosheets measured at a bias potential of 0.4 V (vs Ag/AgCl), (i) CO evolution using $CsPbBr_3$ NCs and 4 nm $CsPbBr_3$ NSs during 30h photocatalytic $CO_2$ reduction. Reproduced with permission [185], Copyright 2021 Wiley-VCH GmbH.

### 4.2. Anion substitution

Mixed halide perovskites proved to be more photoactive compared to solely $CsPbBr_3$. For example, polymerization of 2,2′,5′,2″-ter-3,4-ethylene-dioxythiophene (TerEDOT) over a series of mixed MHPs ($CsPbX_3$, X = I, $I_{0.67}Br_{0.33}$, $I_{0.5}Br_{0.5}$, $Br_{0.67}I_{0.33}$, Br) demonstrated higher photocatalytic activity when iodine was added in the crystal structure. It was shown that $CsPbI_3$ QDs exhibited the most efficient performance due to their narrow bandgap and low exciton binding energy, which was further confirmed with high charge-transport efficiency (Φ) [184]. A series of 2D $CsPbBr_{3-x}I_x$ (x = 0.3, 0.6, 0.9) nanosheets was also investigated for $CO_2$ reduction. Compared with $CsPbBr_3$ nanosheets, all the $CsPbBr_{3-x}I_x$ exhibit improved photocatalytic activity (Figure 19.a,b), due to the enhanced visible light-harvesting capacity by replacing $Br^-$ with $I^-$ [185]. However, an excess of iodide content can result in the lower photocatalytic performance of $CsPb_{3-x}I_x$, probably due to the decrease in the thermodynamic driving force for catalytic $CO_2$ photoreduction.[185] Fourfold higher amount of bromide in $CsPbBr_{2.4}I_{0.6}$ proved optimal for best photocatalytic activity and charge-carrier separation (Figure 19.c) [185]. Recently, M. Knezevic et al. demonstrated photocatalytic hydrogen generation using $CsPbBr_{1.95}I_{1.05}$@$TiO_2$, reaching 250 μmol $g^{-1}$ of $H_2$ after 3h of irradiation. An optimal room-temperature substitution of bromide with iodide is crucial for hydrogen generation together with a thin $TiO_2$ overlayer, essential in both MHP stability and interfacial charge transfer.[186]

Anion substitution strategy was also used to boost the photocatalytic performance of $CsPb(Br_xCl_{1-x})_3$ (x = 1, 0.7, 0.5, 0.3, 0) for $CO_2$ reduction, indicating that $CsPbBr_{0.5}Cl_{0.5}$ was the best catalyst, with a total generation rate of CO and $CH_4$ up to 875 μmol $g^{-1}$, which is almost 4.5 and 9.1 times higher than of pristine $CsPbBr_3$ and $CsPbCl_3$, respectively (Figure 19.d) [187]. Furthermore, the selectivity toward CO and $CH_4$ of all $CsPb(Br_xCl_{1-x})_3$ was up to 99%, and the common $H_2$ byproduct was not obtained (Figure 19.e). The high yield of $CsPb(Br_xCl_{1-x})_3$ in $CO_2$ photoreduction was explained by the efficient charge separation and moderate stability in mixed-halide perovskites [187]. Transient photocurrent responses were also used to explain the

predominant photocatalytic activity of $CsPb(Br_{0.5}Cl_{0.5})_3$, revealing slightly higher charge carrier density of $CsPb(Br_{0.5}Cl_{0.5})_3$, being essential for charge-carrier separation (Figure 19.f).

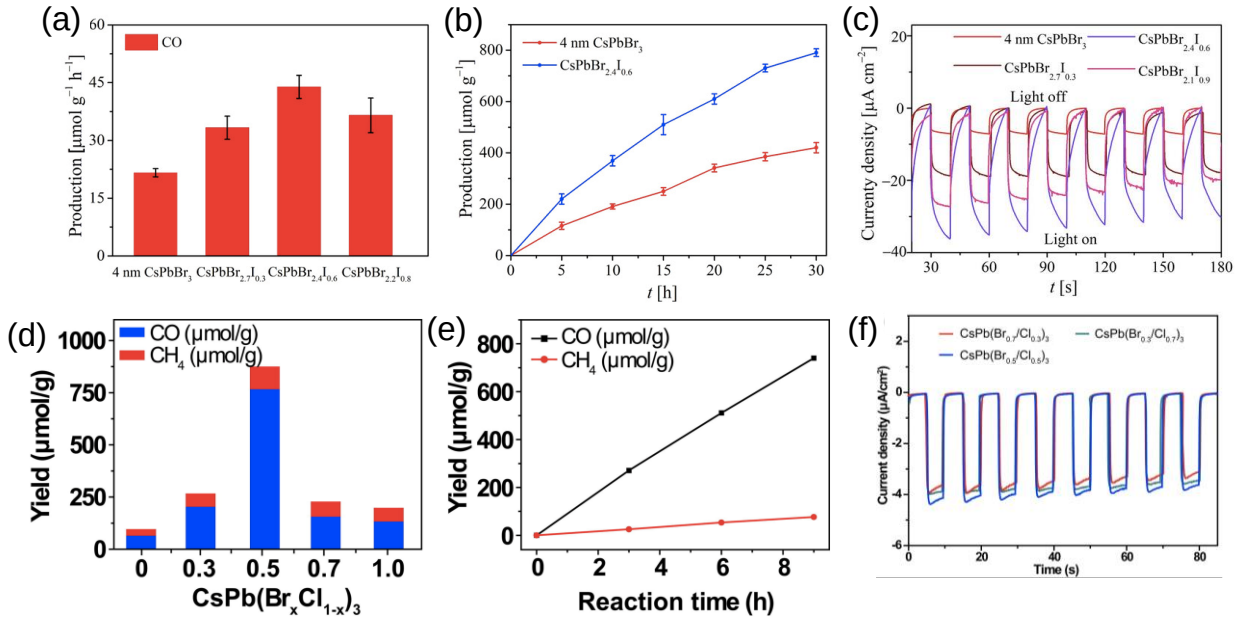


**Figure 19.** (a) The photocatalytic evolution of CO upon anion substitution of bromide, and (b) CO evolution during 30h photocatalytic reaction using 4 nm $CsPbBr_3$ nanosheets and $CsPbBr_{3-x}I_x$ nanosheets. (c) I-t curves of 4 nm $CsPbBr_3$ and $CsPbBr_{3-x}I_x$ nanosheets. Reproduced with permission [185], Copyright 2021 Wiley-VCH GmbH. (d) The evolution of CO and $CH_4$ using $CsPb(Br_x/Cl_{1-x})_3$ (X = 1, 0.7, 0.5, 0.3, 0), (e) CO and $CH_4$ generation rate using $CsPb(Br_{0.5}/Cl_{0.5})_3$ as catalyst. (f) Transient photocurrent responses of mixed halide $CsPb(Br_x/Cl_{1-x})_3$ (x = 0.7, 0.5, 0.3) NCs. Reproduced with permission [187], Copyright 2018 Elsevier Inc.

### 4.3. Doping with metals

Doping with metals represents a valid approach to elevate the photocatalytic performance of $CsPbX_3$. *Sanjib et.al*, successfully demonstrated the photocatalytic performance of 3%Fe(II)-doped $CsPbBr_3$ and its selectivity towards $CH_4$ instead of CO (Figure 20.a) [188]. EIS Nyquist plots show excellent charge-carrier separation in Fe-doped MHP due to the electron transfer (Figure 20.b), as well as high photocurrent response for 3% doping, i.e. 25% in crude solution (Figure 20.c). Moreover, the Fe: $CsPbBr_3$ photocatalyst does not require any additional carrier transportation material or heterostructures like other $CsPbBr_3$ systems (e.g., $CsPbBr_3$/graphene quantum dots, g-$C_3N_4$ and Pd-nanosheets) [188]. Besides Fe(II)-doped $CsPbBr_3$ perovskite NCs, Mn-doped $CsPb(Br/Cl)_3$ mixed-halide MHPs for $CO_2$ photoreduction were reported [189]. A series of $CsPb(Br/Cl)_3$:Mn perovskites, (samples: 1-4, Pb : Mn = 4:1, 2:1, 2:3, 3:7) showed good

photocatalytic activities in $CO_2$ conversion to CO and $CH_4$, with 2:1 ratio demonstrating the highest yield, reaching 1917 µmol $g^{-1}$ and 82 µmol $g^{-1}$ for CO and $CH_4$, respectively, being 14.2 and 1.4 times higher than those of $CsPbBr_3$. Zhang group reported improved photocatalytic performance of cobalt-doped $CsPbBr_3/Cs_4PbBr_6$ for $CO_2$ reduction [190]. $CsPbBr_3/Cs_4PbBr_6$ nanocrystals with 0.5-3% cobalt doping were employed as photocatalysts for $CO_2$ reduction in pure water due to the increased stability upon coating with hexafluorobutyl methacrylate hydrophobic surface layer. $Co_{2\%}@CsPbBr_3/Cs_4PbBr_6$ heterojunction perovskite showed the highest efficiency for photocatalytic $CO_2$ conversion into CO and $CH_4$, with an impressive overall yield of 247 µmol $g^{-1}$under visible light irradiation (Figure 20.d). Co-doping extends the PL lifetime of photogenerated electrons, making transporting them to the acceptor in the reduction process easier. Electrochemical impedance spectroscopy (EIS) and photocurrent response measurements were also used to investigate the effect of Co doping on charge-carrier transfer and separation efficiency (Figure 20.e,f) [190]. The Nyquist plot of $Co_{2\%}@CsPbBr_3/Cs_4PbBr_6$ NCs experience a much smaller semicircle diameter than pristine $CsPbBr_3/Cs_4PbBr_6$ NCs, indicating that Co doping creates more active sites and hence promotes charge transfer from NCs to other components in the reaction system.

*Ling Ding et.al.* reported photocatalytic activity of $Zn^{2+}$- doped $CsPbBr_3$ NCs for hydrogen generation from water, with $Na_2S$ and $Na_2SO_3$ used as the sacrificial agent [191]. In $Zn^{2+}$ doped $CsPbBr_3$, photogenerated electrons are transferred to Zn active site, where proton reduction occurs. Zn-doped MHPs nanocrystals outperformed pure $CsPbBr_3$ NCs in the evolution of hydrogen in water, with a hydrogen production rate of 127 µmol $g^{-1}$ [191].

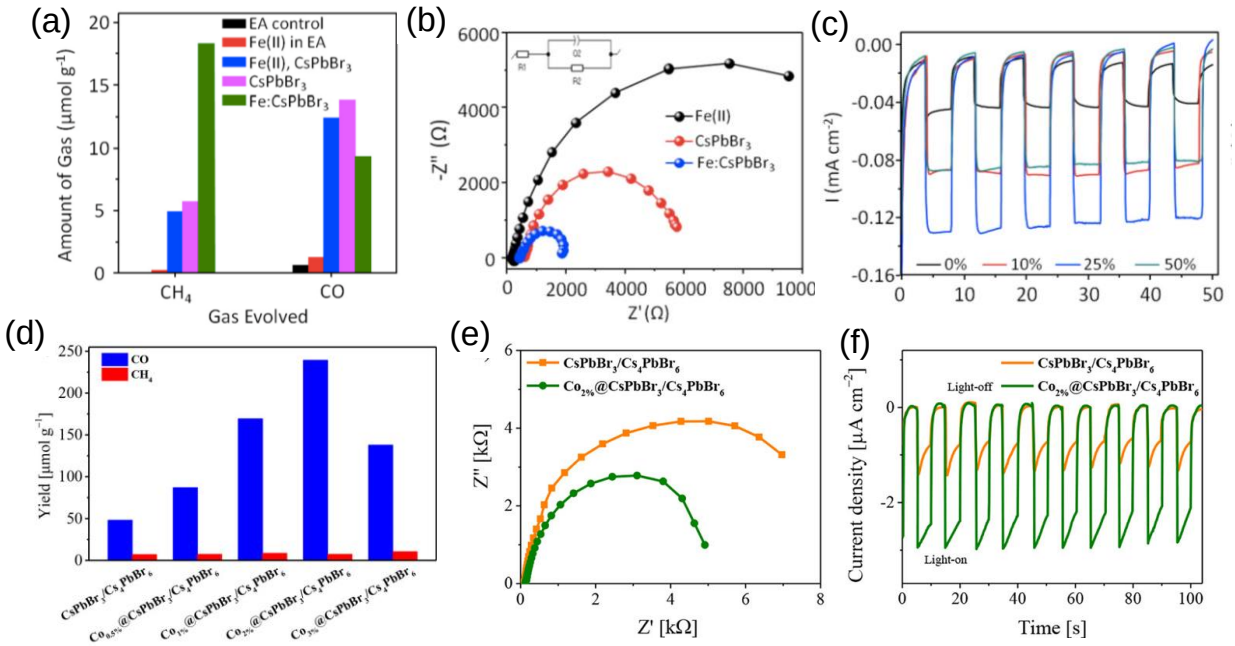


**Figure 20.** (a) the evolution of $CH_4$ and CO using Fe-doped $CsPbBr_3$, (b) EIS Nyquist plots, and (c) I–t curves at a bias potential of -0.4 V (vs. Ag/AgCl) of Fe-doped $CsPbBr_3$, where 25% represents the amount of Fe in crude solution corresponding to 3%Fe doping. Reproduced with permission [188], Copyright 2019 American Chemical Society. (e) EIS Nyquist plots, and (f) I–t curves at a bias potential of -0.4 V (vs. Ag/AgCl) of $CsPbBr_3/Cs_4PbBr_6$ and $Co_{2\%}@CsPbBr_3/Cs_4PbBr_6$. Reproduced with permission [190], Copyright 2019 Wiley-VCH Verlag GmbH & Co. KGaA,Weinheim.

### 4.4. Construction of heterojunctions with perovskites

$CsPbX_3$ coupled with metal complexes that can serve as co-catalysts is also regarded as a useful strategy to enhance photocatalytic performance, i.e., Ni(tpy) [192] and $Re(CO)_3Br(dcbpy)$ [193]. Ni(tpy) can supply specific catalytic sites and serve as electron sinks to avoid electron-hole recombination in $CsPbBr_3$ NCs. As a result, the yield of $CO/CH_4$ increased dramatically, reaching 1724 μmol $g^{-1}$ $CO/CH_4$, which is nearly 26 times higher than that of pristine $CsPbBr_3$ (Figure 21.a,e). The introduction of $Re(CO)_3Br(dcbpy)$ onto $CsPbBr_3$ nanocrystals can serve as a co-catalyst with high catalytic activity and CO selectivity (Figure 21.b,f).

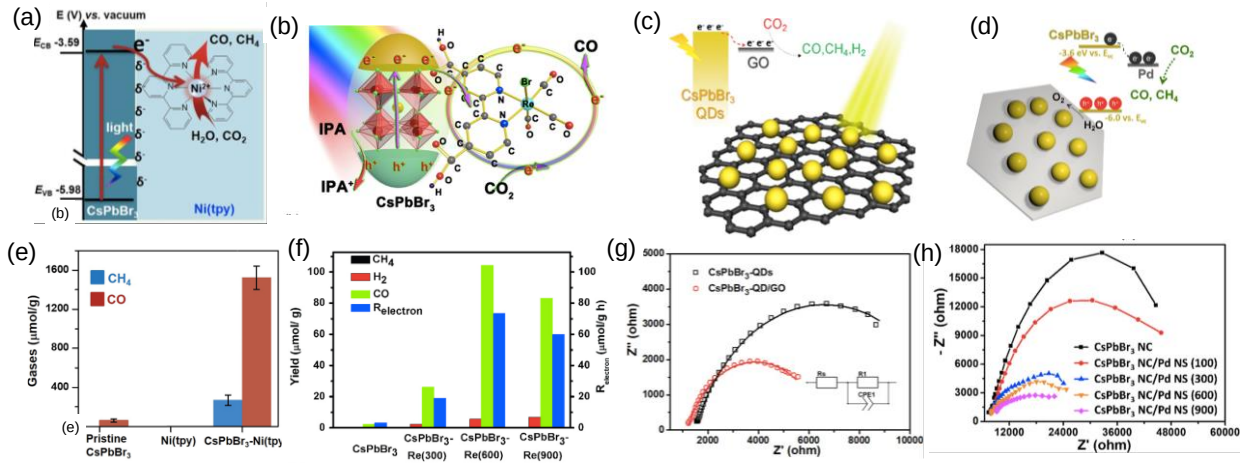


**Figure 21.** Schematic representation of $CO_2$ photoreduction over (a) $CsPbBr_3$-Ni(tpy),[192] (b) $CsPbBr_3$-$Re(CO)_3Br(dcbpy)$,[193] (c) $CsPbBr_3$ QD/graphene oxide (GO),[194] and (d) $CsPbBr_3$ NC/Pd NS photocatalysts.[195] The yield of $CO_2$ reduction products using (e) $CsPbBr_3$-Ni(tpy) [192] and (f) $CsPbBr_3$-$Re(CO)_3Br(dcbpy)$ as photocatalysts [193]. EIS Nyquist plots of (g) $CsPbBr_3$/graphene oxide (GO),[194] (f) $CsPbBr_3$ NC/Pd NSs [195]. Reproduced with permission [192–195], Copyright 2020 American chemical Society, 2019 WILEY-VCH Verlag GmbH & Co. KGaA, Weinheim, Copyright 2017 American chemical Society, and Copyright 2018 American chemical Society, respectively.

Besides metal complexes, other organic molecules were used for coupling with $CsPbBr_3$ in order to enhance the photocatalytic properties through the electron transfer, e.g., methyl viologen, or ferrocene [196–198]. Furthermore, MHPs could be coupled to heterogeneous components such as poly(3-hexylthiophene-2,5-diyl) (P3HT) polymer [199], fullerene [200], MXene nanosheets [201], and porous g-$C_3N_4$ (PCN) [202], in order to promote interfacial charge transfer. In such a configuration, MHPs provide better photocatalytic activity than the pristine $CsPbBr_3$, with a good to excellent yield of products, due to the charge separation that determines the yield of the whole process.

For example, in the $CO_2$ reduction reaction using solely $CsPbBr_3$ as a photocatalyst, the amounts of CO and $CH_4$ formed after 12h were 49.5 and 22.9 μmol $g^{-1}$. After the introduction of graphene oxide (GO), the obtained yield slightly increased to 58.8 and 29.6 μmol $g^{-1}$ for CO and $CH_4$, respectively (Figure 21.c) [194]. Although the CO and $CH_4$ generation rate is quite low, GO facilitates charge-carrier separation via electron transfer, as evidenced by the Nyquist results (Figure 21.g and 21.h). However, one must consider the possible carbon oxidation that could lead

to the apparent CO and $CO_2$ yield increase [203]. In order to reinforce GO influence, bandgap modification through anion exchange could be a possible solution. The charge separation efficiency could also be improved by loading $CsPbBr_3$ NCs graphitic carbon nitride, containing titanium-oxide species (TiO-CN) [204]. The introduction of TiO-CN leads to the swift interfacial charge separation between $CsPbBr_3$ and TiO-CN due to their favorable energy offset and strong chemical bonding, which enhanced the photocatalytic activity of $CsPbBr_3$@TiO-CN in the $CO_2$ reduction to CO. Particularly, the rate of CO formation when using $CsPbBr_3$@TiO-CN as photocatalyst is 129 $\mu$mol $g^{-1}$, which was over 3 times and 6 times higher than those of pristine $CsPbBr_3$ and TiO-CN, respectively. Interestingly, Pd NSs can act as an electron acceptor and co-catalyst in $CO_2$ reduction [195]. As a result, the introduction of Pd NSs boosts the photocatalytic performance of $CsPbBr_3$, with a CO generation rate of 12.633 $\mu$mol $g^{-1}$, which is a 2.4-fold increase compared to the pristine $CsPbBr_3$ (Figure 21.d,h).

### 5.5. Encapsulation of perovskites

As previously mentioned, $CsPbX_3$ nanocrystals are unstable in polar reaction systems, and their catalytic activity is reduced. To meet this challenge, encapsulation is considered as an efficient strategy to protect the $CsPbBr_3$ surface as well as to promote their photocatalytic performance. Up to date, several studies have been carried out, including coating with a thin graphdiyne (GDY) layer [205], silica, $TiO_2$, and polymers such as PANI. Under the protection of GDY, the stability of $CsPbBr_3$ in an aqueous photocatalytic system was improved. Moreover, the surface was decorated with Co, and thus the CO formation rate was also increased, reaching 10.2 $\mu$mol $g^{-1}$, which was 3.1 times higher than pure $CsPbBr_3$ (Figure 22.a). Low charge-transfer resistance has been observed for samples containing GDY, demonstrating successful interfacial charge transfer (Figure 22.b) and stability for over 36h long photocatalytic reaction (Figure 22.c). The silica encapsulation demonstrated the effective removal of methyl orange under visible light. Moreover, $CsPbBr_3/SiO_2$ proved to be efficient for generating singlet oxygen through energy transfer [206].
To improve the stability of $CsPbBr_3$ NCs in photocatalytic water splitting reaction, Zou group used conductive polymer-polyaniline (PANI) as the encapsulating material for the nanocrystals. The PANI-coated $CsPbBr_3$ NCs could remain stable for approximately 11 days, while pure $CsPbBr_3$ decomposed into a white precipitate very quickly [180]. The $CsPbBr_3$@PANI was then used for the hydrogen generation achieving high photocatalytic performance, with the $H_2$ formation yield

of 4.81 mmol.$h^{-1}$.$g^{-1}$ and the stability in 120 h [180].

A chemically stable amorphous $TiO_2$ (a-$TiO_2$) has been identified as both an excellent protective layer (Figure 22.d), and an electron transfer layer (Figure 22.e). The photocatalytic performance of $CsPbBr_3$ NC and $CsPbBr_3$ NC/a-$TiO_2$ (anatase crystalline form) was investigated in $CO_2$RR, and the results showed that the yield of reaction products (CO, $CH_4$) increased significantly after the encapsulation with a-$TiO_2$ (Figure 22.f) [207]. The improvement in photocatalytic performances comes from the band position of a-$TiO_2$, which can build band energy offset with $CsPbBr_3$ NC and provide an additional deactivation pathway through electron transfer (Figure 22.e) [207]. The in situ growth of halide perovskites ($Cs_3Bi_2Br_9$, $Cs_2AgBiBr_6$) in a mesoporous titania framework showed enhancement of the $CO_2$RR [208]. The built-in electric field at the interface of the perovskite nanodots and titania channels promoted the photogenerated charge transfer leading to higher selectivity toward $CH_4$ generation. In other work, ultrathin and small-size graphene oxide (USGO) nanosheets were employed as the electron mediator to construct an efficient Z-scheme system by combining $CsPbBr_3$ with α-$Fe_2O_3$. The heterojunction demonstrated improved efficiency for visible-light-driven $CO_2$RR with water as the electron source [209].

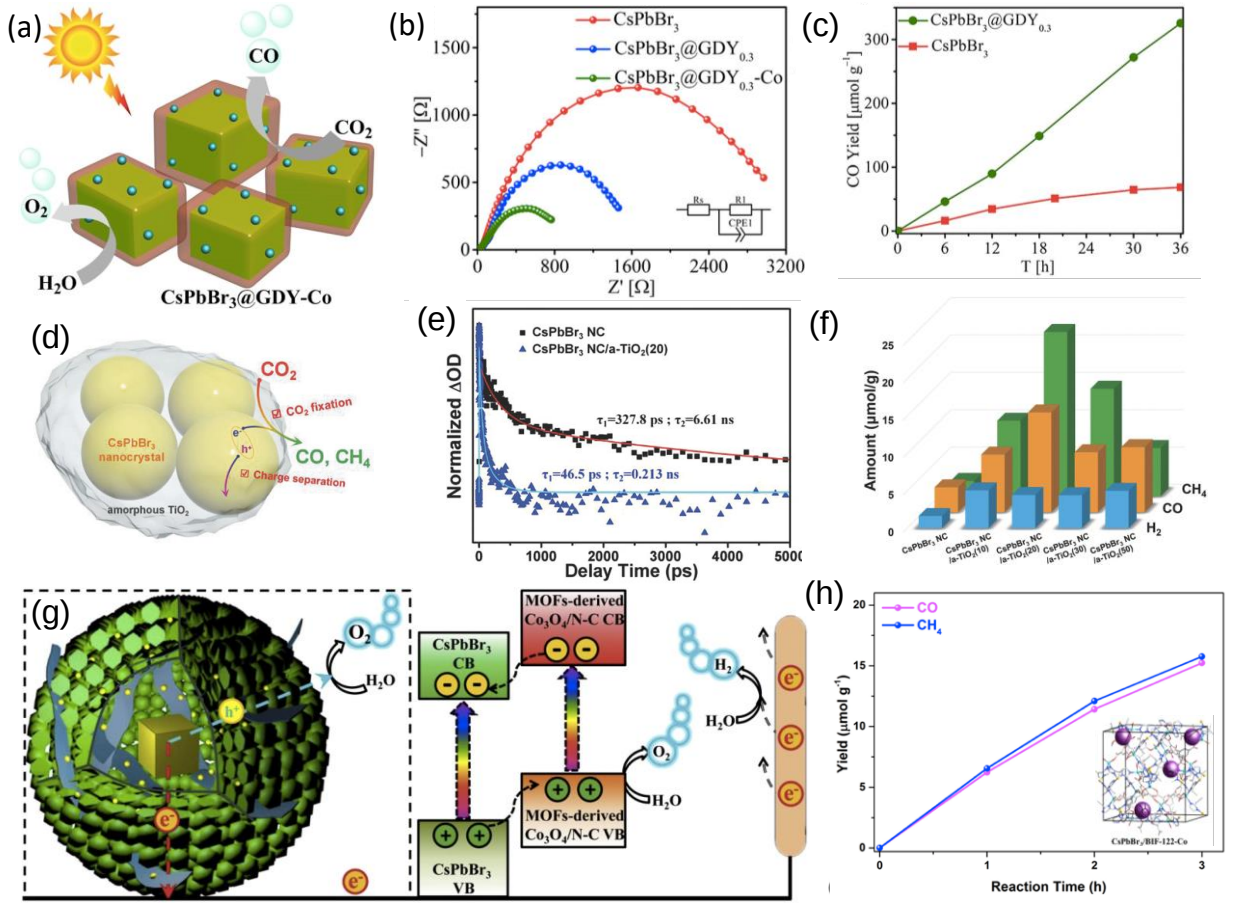


**Figure 22.** (a) Schematic illustration of photocatalytic reaction over $CsPbBr_3$@GDY-Co. (b) EIS Nyquist plots of $CsPbBr_3$@GDY-Co. (c) Photocatalytic evolution using $CsPbBr_3$@GDY-Co. Reproduced with permission [205], Copyright 2020 American Chemical Society. (d) A schematic illustration of the enhanced charge separation and $CO_2$ fixation in a-$TiO_2$-encapsulated $CsPbBr_3$ nanocrystal. Reproduced with permission [207], 2018 WILEY-VCH Verlag GmbH & Co. KGaA, Weinheim. (e) Transient absorption decay curves demonstrating electron transfer from MHP to $TiO_2$, (f) evolution of $CH_4$, CO, $H_2$ using a-$TiO_2$-encapsulated $CsPbBr_3$ as photocatalysts. (g) Illustration of chemical immobilization effect induced by MOFs-derived $Co_3O_4$/N-doped C framework to enhance the aqueous stability of CPB nanocrystal. Reproduced with permission [210], Copyright 2019 Published by Elsevier B.V. (h) $CH_4$, CO, evolution using encapsulated $CsPbBr_3$ by BIF-122-Co and its schematic representation. Reproduced with permission [211], Copyright 2021 American Chemical Society.

Metal-organic frameworks (MOFs), such as ZIF-67-derived $Co_3O_4$, MIL-88 derived $FeO_x$ have proved to be efficient PEC water oxidation photoanode materials [210]. Yin group demonstrated $CsPbBr_3$@metal-organic-frameworks derived $Co_3O_4$/N-doped Carbon core/shell composite (MHP@$Co_3O_4$/N-C) [210]. The unique N-Br halogen bonds are formed between Pyrrodic-N from N-frameworks and the Br atom from $CsPbBr_3$ NCs. Due to this distinct chemical bonding

immobilization effect introduced by the MOFs-derived $Co_3O_4$/N-C frameworks, the decomposition of $CsPbBr_3$ in an aqueous solution can be effectively inhibited, thus greatly enhancing the stability of MHP@$Co_3O_4$/N-C system (Figure 22.g). Such a configuration results in the unique type-II heterojunction, allowing charge-carrier separation, where holes are accumulated into the VB of the MOF and electrons are flowing to the CB of MHP, enhancing the photocatalytic performance of pristine MHP, while acting as a co-catalyst during water oxidation.

Boron imidazolate frameworks (BIFs) have recently attracted a lot of interest in the field of $CO_2$ reduction [211]. Due to the electron-deficient property of B and the presence of active B-H sites in the internal pore surface, the affinity of BIF with the confined perovskite could be directly increased, and thus provide an interfacial contact [211]. The terminal oxygen in BIFs can coordinate with $Pb^{2+}$ cation, which induces preferential nucleation of $CsPbX_3$ crystals. Therefore, BIFs could be suitable for perovskite encapsulation and catalytic activity improvement toward $CO_2$RR. *Zhen-Yu Chen et.al.* designed and synthesized *ctn*-type microporous BIF (cation) $[Co_3[BH(2\text{-ipim})_3]_2(BTC)_2]_n$(BIF-122-Co; with ipim = isopropylimidazolate and BTC = 1,3,5-benzenetricarboxylate) and used it as a host matrix to encapsulate $CsPbBr_3$, to afford a perovskite-BIF composite, $CsPbBr_3$/BIF-122-Co. The porous skeleton of BIF-122-Co in the composite material could considerably improve the stability of the $CsPbBr_3$ perovskite in the photocatalytic reaction system (Figure 22.h, insert). The photocatalytic activity of $CsPbBr_3$/BIF-122-Co in $H_2O$/ethyl acetate exhibits high activity in $CO_2$RR with the total CO and CH4 formation rates being 15.23 and 15.76 $\mu mol.g^{-1}$ after 3 hours, respectively (Figure 22.h) [211].

Herein, we described different strategies to enhance metal-halide perovskites' photocatalytic performance. The above-mentioned modifications have shown improved photocatalytic activity compared to the pristine $CsPbX_3$. MHP encapsulation is widely used to improve MHPs stability and boost charge-carrier separation. However, studies have shown that surface treatment, morphology manipulation, and metal doping could highly influence, both MHP stability and photocatalytic activity. One should note, coating with carbon-based materials could influence the photocatalytic yield of CO and $CO_2$, due to carbon oxidation [203].

## 4. Conclusion and perspectives

Metal-halide perovskites are perfect candidates for photocatalytic applications due to their optical

and electronic properties. This review highlights a variety of synthetic procedures focused on the surface, morphological, and structural modifications that influence MHP's stability, optical properties, charge-carrier dynamics, and especially photocatalytic activity. We provide an overview of MHP's charge-carrier dynamics to discern charge-carrier intraband relaxation, trapping, and non-radiative and radiative recombination while considering quantum confinement, cation and anion type, metallic doping, coupling, and encapsulation of MHPs in stable materials. We then summarize the charge transfer mechanisms upon MHPs coupling, encapsulation, and doping that are necessary to maximize charge-carrier separation for photocatalytic applications.

Photocatalysis requires slow charge carrier relaxation at early delay times, whereas non-radiative losses (e.g., Auger recombination) need to be minimized. At the pico- and nanoscale, the charge-carrier lifetime could be prolonged through charge transfer, resulting in photoluminescence quenching. MHPs exhibit unbalanced charge-carrier diffusion, demonstrating significantly higher diffusion of holes; this property could significantly improve oxidation reactions.

The stability and the toxicity remain, without a doubt, the major issue to overcome. While studies are discussing the protection of MHPs and claiming improved stability toward various reaction, a lack of post-reaction characterization can be observed, and the development of in situ characterization techniques during the photocatalytic process is needed. Moreover, new synthetic strategies should be explored to encapsulate and protect MHPs using a water-repellant organic and inorganic shell to maintain their stability in an aqueous solvent.

The versatility of the optical and electronic properties of MHPs allows the adjustment of their conduction and valence band potential energy for selective oxidation and reduction reactions. Simultaneous and rigorous characterization of the optical and electronic properties of modified MHPs could lead to a better correlation between the photochemical and electronic properties. The presence of defects in MHPs has not yet been explored in terms of photocatalytic reaction. The defect nature (shallow or deep) is known to affect the carrier separation, and, thus the quantum efficiency during the photocatalytic reaction. The defect nature control would enlighten a strategy to reach an effective charge carrier lifetime, and better understanding of the photocatalytic reaction mechanism.

To go further, the future studies should focus on the charge-carrier dynamics and photocatalytic properties of 2D materials, i.e., NPLs, and NSs. 2D cesium-lead halide-based materials could demonstrate significantly improved photocatalytic activity, due to their higher surface availability

and reduced thickness that allows efficient transport of the free charge carriers to the surface of the photocatalyst.

Finally, MHPs commercialization in the photocatalytic field could be attainable with the development of automated high-yield synthetic procedures and, most importantly, with stability improvements that are needed for achieving high photocatalytic activity and reproducibility. So far, the concept of MHPs' employment in photocatalysis has been demonstrated on a small scale, and medium or industrial scale is yet to be explored and developed.

**Acknowledgments**

MK acknowledges the « Ministère de l'enseignement supérieur et de la recherche Français » for the PhD grant. MK, CCJ, and MNG acknowledge the IDEX Paris-Saclay and IRS MOMENTOM for financial support. MNG thanks the French National Research Agency (ANR), through the IngenCat project (ANR-20-CE43-0014), for the financial support. The authors acknowledge the ACT programme (Accelerating CCS Technologies, Horizon2020 Project No. 691712) for the financial support of the NEXTCCUS project (project ID: 327327). MAJ acknowledges the Royal Society (RGS\R1\211068) and Cambridge Materials Limited for their funding and technical support.

**References**

1. Wells HL (1893) Über die Cäsium- und Kalium-Bleihalogenide. Zeitschrift für Anorg Chemie 3:195–210. https://doi.org/10.1002/zaac.18930030124
2. Møller CK (1959) The Structure Of Cæsium Plumbo Iodide CsPbI3. Mat Fys Medd Dan Vid Selsk 32:1–18
3. Møller CK (1959) The Structure of Perovskite-like caesium plumbo trihalides
4. Wooster WA, M CK (1936) Crystal Structure and Photoconductivity of Caesium Plumbohalides Nuclear Magnetic Resonance in ~-Brass
5. Rose G (1840) Ueber einige neue Mineralien des Urals. J f�r Prakt Chemie 19:459–468. https://doi.org/10.1002/prac.18400190179
6. Goldschmidt VM (1926) Die Gesetze der Krystallochemie. Naturwissenschaften 14:477–485. https://doi.org/10.1007/BF01507527
7. Cape JA, White RL, Feigelson RS (1969) EPR study of the structure of CsPbCl3. J Appl Phys 40:5001–5005. https://doi.org/10.1063/1.1657345
8. Saidaminov MI, Almutlaq J, Sarmah S, et al (2016) Pure Cs4PbBr6: Highly Luminescent Zero-Dimensional Perovskite Solids. ACS Energy Lett 1:840–845. https://doi.org/10.1021/acsenergylett.6b00396
9. Wang L, Liu H, Zhang Y, Mohammed OF (2020) Photoluminescence Origin of Zero-Dimensional Cs4PbBr6 Perovskite. ACS Energy Lett 5:87–99.

https://doi.org/10.1021/acsenergylett.9b02275
10. Zhu H, Fu Y, Meng F, et al (2015) Lead halide perovskite nanowire lasers with low lasing thresholds and high quality factors. Nat Mater 14:636–642. https://doi.org/10.1038/nmat4271
11. Zhang Z, Liu Y, Geng C, et al (2019) Rapid synthesis of quantum-confined CsPbBr3 perovskite nanowires using a microfluidic reactor. Nanoscale 11:18790–18796. https://doi.org/10.1039/c9nr06726d
12. Breternitz J, Schorr S (2018) What Defines a Perovskite? Adv Energy Mater 8:1–2. https://doi.org/10.1002/aenm.201802366
13. Akkerman QA, Manna L (2020) What Defines a Halide Perovskite? ACS Energy Lett 604–610. https://doi.org/10.1021/acsenergylett.0c00039
14. Li Z, Yang M, Park JS, et al (2016) Stabilizing Perovskite Structures by Tuning Tolerance Factor: Formation of Formamidinium and Cesium Lead Iodide Solid-State Alloys. Chem Mater 28:284–292. https://doi.org/10.1021/acs.chemmater.5b04107
15. Tsui KY, Onishi N, Berger RF (2016) Tolerance Factors Revisited: Geometrically Designing the Ideal Environment for Perovskite Dopants. J Phys Chem C 120:23293–23298. https://doi.org/10.1021/acs.jpcc.6b09277
16. Nitsch K, Dušek M, Nikl M, et al (1995) Ternary alkali lead chlorides: Crystal growth, crystal structure, absorption and emission properties. Prog Cryst Growth Charact Mater 30:1–22. https://doi.org/10.1016/0960-8974(95)00012-V
17. Rodová M, Brooek J, Kníiek K, Nitsch K (2003) PHASE TRANSITIONS IN TERNARY CAESIUM LEAD BROMIDE
18. MØLLER CK (1958) Crystal Structure and Photoconductivity of Cæsium Plumbohalides. Nature 182:1436–1436. https://doi.org/10.1038/1821436a0
19. Marronnier A, Roma G, Boyer-Richard S, et al (2018) Anharmonicity and Disorder in the Black Phases of CsPbI3 used for Stable Inorganic Perovskite Solar Cells. 2018 IEEE 7th World Conf Photovolt Energy Conversion, WCPEC 2018 - A Jt Conf 45th IEEE PVSC, 28th PVSEC 34th EU PVSEC 12:1715–1717. https://doi.org/10.1109/PVSC.2018.8547769
20. Protesescu L, Yakunin S, Bodnarchuk MI, et al (2015) Nanocrystals of Cesium Lead Halide Perovskites (CsPbX 3 , X = Cl, Br, and I): Novel Optoelectronic Materials Showing Bright Emission with Wide Color Gamut. Nano Lett 15:3692–3696. https://doi.org/10.1021/nl5048779
21. Heidrich K, Künzel H, Treusch J (1978) Optical properties and electronic structure of CsPbCl3 and CsPbBr3. Solid State Commun 25:887–889. https://doi.org/10.1016/0038-1098(78)90294-6
22. Ito H, Onaka R, Onuki H (1978) Optical and Photoelectronic Studies of CsPbCl3 and CsPbBr3. J Phys Soc Japan 45:2043–2044. https://doi.org/10.1143/JPSJ.45.2043
23. Nitsch K, Hamplová V, Nikl M, et al (1996) Lead bromide and ternary alkali lead bromide single crystals — growth and emission properties. Chem Phys Lett 258:518–522. https://doi.org/10.1016/0009-2614(96)00665-3
24. Nikla M, Nitsch K, Mihbkova E, et al (1997) LUMINESCENCE Quantum size effect in the excitonic luminescence of CsPbX,-like quantum dots in CsX (X = Cl, Br) single crystal host
25. Kondo SI, Kakuchi M, Masaki A, Saito T (2003) Strongly enhanced free-exciton luminescence in microcrystalline CsPbBr 3 films. J Phys Soc Japan 72:1789–1791. https://doi.org/10.1143/JPSJ.72.1789
26. Stoumpos CC, Malliakas CD, Peters JA, et al (2013) Crystal growth of the perovskite semiconductor CsPbBr3: A new material for high-energy radiation detection. Cryst Growth Des 13:2722–2727. https://doi.org/10.1021/cg400645t
27. Elbaz GA, Straus DB, Semonin OE, et al (2017) Unbalanced Hole and Electron Diffusion in Lead Bromide Perovskites. Nano Lett 17:1727–1732. https://doi.org/10.1021/acs.nanolett.6b05022
28. Dong Y, Gu Y, Zou Y, et al (2016) Improving All-Inorganic Perovskite Photodetectors by Preferred Orientation and Plasmonic Effect. Small 12:5622–5632. https://doi.org/10.1002/smll.201602366

29. Herz LM (2017) Charge-Carrier Mobilities in Metal Halide Perovskites: Fundamental Mechanisms and Limits. ACS Energy Lett 2:1539–1548. https://doi.org/10.1021/acsenergylett.7b00276
30. Kulbak M, Cahen D, Hodes G (2015) How Important Is the Organic Part of Lead Halide Perovskite Photovoltaic Cells? Efficient CsPbBr3 Cells. J Phys Chem Lett 6:2452–2456. https://doi.org/10.1021/acs.jpclett.5b00968
31. Kojima A, Teshima K, Shirai Y, Miyasaka T (2009) Organometal halide perovskites as visible-light sensitizers for photovoltaic cells. J Am Chem Soc 131:6050–6051. https://doi.org/10.1021/ja809598r
32. Im JH, Lee CR, Lee JW, et al (2011) 6.5% efficient perovskite quantum-dot-sensitized solar cell. Nanoscale 3:4088–4093. https://doi.org/10.1039/c1nr10867k
33. Kim HS, Lee CR, Im JH, et al (2012) Lead iodide perovskite sensitized all-solid-state submicron thin film mesoscopic solar cell with efficiency exceeding 9%. Sci Rep 2:1–7. https://doi.org/10.1038/srep00591
34. Lee MM, Teuscher J, Miyasaka T, et al (2012) Efficient hybrid solar cells based on meso-superstructured organometal halide perovskites. Science (80- ) 338:643–647. https://doi.org/10.1126/science.1228604
35. Swarnkar A, Ravi VK, Nag A (2017) Beyond colloidal cesium lead halide perovskite nanocrystals: Analogous metal halides and doping. ACS Energy Lett 2:1089–1098. https://doi.org/10.1021/acsenergylett.7b00191
36. Marronnier A, Roma G, Boyer-Richard S, et al (2018) Anharmonicity and Disorder in the Black Phases of Cesium Lead Iodide Used for Stable Inorganic Perovskite Solar Cells. ACS Nano 12:3477–3486. https://doi.org/10.1021/acsnano.8b00267
37. https://www.nrel.gov/pv/cell-efficiency.html https://www.nrel.gov/pv/cell-efficiency.html
38. Huang CY, Zou C, Mao C, et al (2017) CsPbBr3 Perovskite Quantum Dot Vertical Cavity Lasers with Low Threshold and High Stability. ACS Photonics 4:2281–2289. https://doi.org/10.1021/acsphotonics.7b00520
39. Jung DH, Park JH, Lee HE, et al (2019) Flash-induced ultrafast recrystallization of perovskite for flexible light-emitting diodes. Nano Energy 61:236–244. https://doi.org/10.1016/j.nanoen.2019.04.061
40. Nedelcu G, Protesescu L, Yakunin S, et al (2015) Fast Anion-Exchange in Highly Luminescent Nanocrystals of Cesium Lead Halide Perovskites (CsPbX3, X = Cl, Br, I). Nano Lett 15:5635–5640. https://doi.org/10.1021/acs.nanolett.5b02404
41. Wang D, Li W, Du Z, et al (2020) CoBr2-doping-induced efficiency improvement of CsPbBr3 planar perovskite solar cells. J Mater Chem C 8:1649–1655. https://doi.org/10.1039/c9tc05679c
42. Shapiro A, Heindl MW, Horani F, et al (2019) Significance of Ni Doping in CsPbX3 Nanocrystals via Postsynthesis Cation-Anion Coexchange. J Phys Chem C 123:24979–24987. https://doi.org/10.1021/acs.jpcc.9b08317
43. Yong ZJ, Guo SQ, Ma JP, et al (2018) Doping-Enhanced Short-Range Order of Perovskite Nanocrystals for Near-Unity Violet Luminescence Quantum Yield. J Am Chem Soc 140:9942–9951. https://doi.org/10.1021/jacs.8b04763
44. Huang D, Bo J, Zheng R, et al (2021) Luminescence and Stability Enhancement of CsPbBr3 Perovskite Quantum Dots through Surface Sacrificial Coating. Adv Opt Mater. https://doi.org/10.1002/ADOM.202100474
45. Kim H, Bae SR, Lee TH, et al (2021) Enhanced Optical Properties and Stability of CsPbBr3 Nanocrystals Through Nickel Doping. Adv Funct Mater 31:2102770. https://doi.org/10.1002/adfm.202102770
46. Yao J-S, Ge J, Han B-N, et al (2018) Ce 3+ -Doping to Modulate Photoluminescence Kinetics for Efficient CsPbBr 3 Nanocrystals Based Light-Emitting Diodes. J Am Chem Soc 140:3626–3634. https://doi.org/10.1021/jacs.7b11955
47. Yin J, Ahmed GH, Bakr OM, et al (2019) Unlocking the Effect of Trivalent Metal Doping in All-Inorganic CsPbBr 3 Perovskite. ACS Energy Lett 4:789–795. https://doi.org/10.1021/acsenergylett.9b00209

48. Lozhkina OA, Murashkina AA, Shilovskikh V V., et al (2018) Invalidity of Band-Gap Engineering Concept for Bi 3+ Heterovalent Doping in CsPbBr 3 Halide Perovskite. J Phys Chem Lett 9:5408–5411. https://doi.org/10.1021/acs.jpclett.8b02178
49. Tong Y, Bladt E, Aygüler MF, et al (2016) Highly Luminescent Cesium Lead Halide Perovskite Nanocrystals with Tunable Composition and Thickness by Ultrasonication. Angew Chemie - Int Ed 55:13887–13892. https://doi.org/10.1002/anie.201605909
50. Hoffman JB, Schleper AL, Kamat P V. (2016) Transformation of Sintered CsPbBr3 Nanocrystals to Cubic CsPbI3 and Gradient CsPbBrxI3-x through Halide Exchange. J Am Chem Soc 138:8603–8611. https://doi.org/10.1021/jacs.6b04661
51. Su Y, Chen X, Ji W, et al (2017) Highly Controllable and Efficient Synthesis of Mixed-Halide CsPbX3 (X = Cl, Br, I) Perovskite QDs toward the Tunability of Entire Visible Light. ACS Appl Mater Interfaces 9:33020–33028. https://doi.org/10.1021/acsami.7b10612
52. Mandal S, Roy D, De CK, et al (2019) Instantaneous, room-temperature, open-air atmosphere, solution-phase synthesis of perovskite quantum dots through halide exchange employing non-metal based inexpensive HCl/HI: Ensemble and single particle spectroscopy. Nanoscale Adv 1:3506–3513. https://doi.org/10.1039/c9na00406h
53. Van der Stam W, Geuchies JJ, Altantzis T, et al (2017) Highly Emissive Divalent-Ion-Doped Colloidal CsPb1-xMxBr3 Perovskite Nanocrystals through Cation Exchange. J Am Chem Soc 139:4087–4097. https://doi.org/10.1021/jacs.6b13079
54. Thawarkar S, Rana PJS, Narayan R, Singh SP (2019) Ni-Doped CsPbBr3 Perovskite: Synthesis of Highly Stable Nanocubes. Langmuir 35:17150–17155. https://doi.org/10.1021/acs.langmuir.9b02450
55. Bi C, Wang S, Li Q, et al (2019) Thermally Stable Copper(II)-Doped Cesium Lead Halide Perovskite Quantum Dots with Strong Blue Emission. J Phys Chem Lett 10:943–952. https://doi.org/10.1021/acs.jpclett.9b00290
56. Wang B, Liu L, Liu B, et al (2020) Study on fluorescence properties and stability of Cu2+-Substituted CsPbBr3 perovskite quantum dots. Phys B Condens Matter 599:412488. https://doi.org/10.1016/j.physb.2020.412488
57. Li Y, Huang H, Xiong Y, et al (2018) Revealing the Formation Mechanism of CsPbBr3 Perovskite Nanocrystals Produced via a Slowed-Down Microwave-Assisted Synthesis. Angew Chemie - Int Ed 57:5833–5837. https://doi.org/10.1002/anie.201713332
58. Pan Q, Hu H, Zou Y, et al (2017) Microwave-assisted synthesis of high-quality "all-inorganic" CsPbX3 (X = Cl, Br, I) perovskite nanocrystals and their application in light emitting diodes. J Mater Chem C 5:10947–10954. https://doi.org/10.1039/c7tc03774k
59. Liu W, Zheng J, Cao S, et al (2018) General Strategy for Rapid Production of Low-Dimensional All-Inorganic CsPbBr 3 Perovskite Nanocrystals with Controlled Dimensionalities and Sizes. Inorg Chem 57:1598–1603. https://doi.org/10.1021/acs.inorgchem.7b02941
60. Liu H, Wu Z, Gao H, et al (2017) One-Step Preparation of Cesium Lead Halide CsPbX3 (X = Cl, Br, and I) Perovskite Nanocrystals by Microwave Irradiation. ACS Appl Mater Interfaces 9:42919–42927. https://doi.org/10.1021/acsami.7b14677
61. Long Z, Ren H, Sun J, et al (2017) High-throughput and tunable synthesis of colloidal CsPbX 3 perovskite nanocrystals in a heterogeneous system by microwave irradiation. Chem Commun 53:9914–9917. https://doi.org/10.1039/C7CC04862A
62. Rao L, Tang Y, Song C, et al (2019) Polar-Solvent-Free Synthesis of Highly Photoluminescent and Stable CsPbBr 3 Nanocrystals with Controlled Shape and Size by Ultrasonication. Chem Mater 31:365–375. https://doi.org/10.1021/acs.chemmater.8b03298
63. Tong Y, Yao E-P, Manzi A, et al (2018) Spontaneous Self-Assembly of Perovskite Nanocrystals into Electronically Coupled Supercrystals: Toward Filling the Green Gap. Adv Mater 30:1801117. https://doi.org/10.1002/adma.201801117
64. Duong T, Mulmudi HK, Shen H, et al (2016) Structural engineering using rubidium iodide as a dopant under excess lead iodide conditions for high efficiency and stable perovskites. Nano Energy 30:330–340. https://doi.org/10.1016/j.nanoen.2016.10.027
65. Zhai W, Lin J, Li Q, et al (2018) Solvothermal Synthesis of Ultrathin Cesium Lead Halide

Perovskite Nanoplatelets with Tunable Lateral Sizes and Their Reversible Transformation into Cs4PbBr6 Nanocrystals. Chem Mater 30:3714–3721. https://doi.org/10.1021/acs.chemmater.8b00612
66. Zhai W, Lin J, Li C, et al (2018) Solvothermal synthesis of cesium lead halide perovskite nanowires with ultra-high aspect ratios for high-performance photodetectors. Nanoscale 10:21451–21458. https://doi.org/10.1039/c8nr05683h
67. Chen M, Zou Y, Wu L, et al (2017) Solvothermal Synthesis of High-Quality All-Inorganic Cesium Lead Halide Perovskite Nanocrystals: From Nanocube to Ultrathin Nanowire. Adv Funct Mater 27:1701121. https://doi.org/10.1002/adfm.201701121
68. Chen D, Chen X, Li J, et al (2018) Ultrathin CsPbX3 (X = Cl, Br, I) nanoplatelets: Solvothermal synthesis and optical spectroscopic properties. Dalt Trans 47:9845–9849. https://doi.org/10.1039/c8dt01720d
69. Li ZJ, Hofman E, Davis AH, et al (2018) General Strategy for the Growth of CsPbX3 (X = Cl, Br, I) Perovskite Nanosheets from the Assembly of Nanorods. Chem Mater 30:3854–3860. https://doi.org/10.1021/acs.chemmater.8b01283
70. Chen M, Hu H, Tan Y, et al (2018) Controlled growth of dodecapod-branched CsPbBr3 nanocrystals and their application in white light emitting diodes. Nano Energy 53:559–566. https://doi.org/10.1016/j.nanoen.2018.09.020
71. Li X, Wu Y, Zhang S, et al (2016) CsPbX $_3$ Quantum Dots for Lighting and Displays: Room-Temperature Synthesis, Photoluminescence Superiorities, Underlying Origins and White Light-Emitting Diodes. Adv Funct Mater 26:2435–2445. https://doi.org/10.1002/adfm.201600109
72. Wei S, Yang Y, Kang X, et al (2016) Room-temperature and gram-scale synthesis of CsPbX 3 (X = Cl, Br, I) perovskite nanocrystals with 50–85% photoluminescence quantum yields. Chem Commun 52:7265–7268. https://doi.org/10.1039/C6CC01500J
73. Akkerman QA, Park S, Radicchi E, et al (2017) Nearly Monodisperse Insulator Cs4PbX6 (X = Cl, Br, I) Nanocrystals, Their Mixed Halide Compositions, and Their Transformation into CsPbX3 Nanocrystals. Nano Lett 17:1924–1930. https://doi.org/10.1021/acs.nanolett.6b05262
74. Palazon F, Urso C, De Trizio L, et al (2017) Postsynthesis Transformation of Insulating Cs4PbBr6 Nanocrystals into Bright Perovskite CsPbBr3 through Physical and Chemical Extraction of CsBr. ACS Energy Lett 2:2445–2448. https://doi.org/10.1021/acsenergylett.7b00842
75. Wu L, Hu H, Xu Y, et al (2017) From Nonluminescent Cs4PbX6 (X = Cl, Br, I) Nanocrystals to Highly Luminescent CsPbX3 Nanocrystals: Water-Triggered Transformation through a CsX-Stripping Mechanism. Nano Lett 17:5799–5804. https://doi.org/10.1021/acs.nanolett.7b02896
76. Yang L, Wang T, Min Q, et al (2019) High Water Resistance of Monoclinic CsPbBr 3 Nanocrystals Derived from Zero-Dimensional Cesium Lead Halide Perovskites. ACS Omega 4:6084–6091. https://doi.org/10.1021/acsomega.9b00370
77. Zhu ZY, Yang QQ, Gao LF, et al (2017) Solvent-Free Mechanosynthesis of Composition-Tunable Cesium Lead Halide Perovskite Quantum Dots. J Phys Chem Lett 8:1610–1614. https://doi.org/10.1021/acs.jpclett.7b00431
78. Liu X, Gao J, Zhou G, et al (2020) Low molecular weight molecule induces the effective stabilization of CsPbBr3 in water. J Mol Liq 299:112199. https://doi.org/10.1016/j.molliq.2019.112199
79. Wang B, Zhang C, Zheng W, et al (2020) Large-Scale Synthesis of Highly Luminescent Perovskite Nanocrystals by Template-Assisted Solid-State Reaction at 800 °C. Chem Mater 32:308–314. https://doi.org/10.1021/acs.chemmater.9b03804
80. Pan A, He B, Fan X, et al (2016) Insight into the Ligand-Mediated Synthesis of Colloidal CsPbBr3 Perovskite Nanocrystals: The Role of Organic Acid, Base, and Cesium Precursors. ACS Nano 10:7943–7954. https://doi.org/10.1021/acsnano.6b03863
81. Lu C, Wright MW, Ma X, et al (2019) Cesium Oleate Precursor Preparation for Lead Halide Perovskite Nanocrystal Synthesis: The Influence of Excess Oleic Acid on Achieving

Solubility, Conversion, and Reproducibility. Chem Mater 31:62–67. https://doi.org/10.1021/acs.chemmater.8b04876
82. Zhang Y, Siegler TD, Thomas CJ, et al (2020) A “tips and Tricks” Practical Guide to the Synthesis of Metal Halide Perovskite Nanocrystals. Chem Mater 32:5410–5423. https://doi.org/10.1021/acs.chemmater.0c01735
83. Li M, Zhang X, Du Y, Yang P (2017) Colloidal CsPbX3 (X = Br, I, Cl) NCs: Morphology controlling, composition evolution, and photoluminescence shift. J Lumin 190:397–402. https://doi.org/10.1016/j.jlumin.2017.05.080
84. Liang Z, Zhao S, Xu Z, et al (2016) Shape-Controlled Synthesis of All-Inorganic CsPbBr3 Perovskite Nanocrystals with Bright Blue Emission. ACS Appl Mater Interfaces 8:28824–28830. https://doi.org/10.1021/acsami.6b08528
85. Balakrishnan SK, Kamat P V. (2018) Ligand Assisted Transformation of Cubic CsPbBr3 Nanocrystals into Two-Dimensional CsPb2Br5 Nanosheets. Chem Mater 30:74–78. https://doi.org/10.1021/acs.chemmater.7b04142
86. Xiao M, Hao M, Lyu M, et al (2019) Surface Ligands Stabilized Lead Halide Perovskite Quantum Dot Photocatalyst for Visible Light-Driven Hydrogen Generation. Adv Funct Mater 1905683. https://doi.org/10.1002/adfm.201905683
87. Akkerman QA, Motti SG, Srimath Kandada AR, et al (2016) Solution Synthesis Approach to Colloidal Cesium Lead Halide Perovskite Nanoplatelets with Monolayer-Level Thickness Control. J Am Chem Soc 138:1010–1016. https://doi.org/10.1021/jacs.5b12124
88. Ye F, Zhang H, Li W, et al (2019) Ligand-Exchange of Low-Temperature Synthesized CsPbBr3 Perovskite toward High-Efficiency Light-Emitting Diodes. Small Methods 3:1800489. https://doi.org/10.1002/smtd.201800489
89. Li J, Xu L, Wang T, et al (2017) 50-Fold EQE Improvement up to 6.27% of Solution-Processed All-Inorganic Perovskite CsPbBr3 QLEDs via Surface Ligand Density Control. Adv Mater 29:1603885. https://doi.org/10.1002/adma.201603885
90. De Roo J, Ibáñez M, Geiregat P, et al (2016) Highly Dynamic Ligand Binding and Light Absorption Coefficient of Cesium Lead Bromide Perovskite Nanocrystals. ACS Nano 10:2071–2081. https://doi.org/10.1021/acsnano.5b06295
91. Zhang D, Eaton SW, Yu Y, et al (2015) Solution-Phase Synthesis of Cesium Lead Halide Perovskite Nanowires. J Am Chem Soc 137:9230–9233. https://doi.org/10.1021/jacs.5b05404
92. Tang X, Han S, Zu Z, et al (2018) All-inorganic perovskite CsPb2Br5 microsheets for photodetector application. In: Frontiers in Physics
93. Jing Q, Xu Y, Su Y, et al (2019) A systematic study of the synthesis of cesium lead halide nanocrystals: Does Cs 4 PbBr 6 or CsPbBr 3 form? Nanoscale 11:1784–1789. https://doi.org/10.1039/c8nr08116f
94. Zhang Y, Saidaminov MI, Dursun I, et al (2017) Zero-Dimensional Cs4PbBr6 Perovskite Nanocrystals. J Phys Chem Lett 8:961–965. https://doi.org/10.1021/acs.jpclett.7b00105
95. Yang H, Zhang Y, Pan J, et al (2017) Room-Temperature Engineering of All-Inorganic Perovskite Nanocrsytals with Different Dimensionalities. Chem. Mater. 29:8978–8982
96. Wen JR, Roman BJ, Rodriguez Ortiz FA, et al (2019) Chemical availability of bromide dictates cspbbr3 nanocrystal growth. Chem Mater 31:8551–8557. https://doi.org/10.1021/acs.chemmater.9b03709
97. Akkerman QA, Abdelhady AL, Manna L (2018) Zero-Dimensional Cesium Lead Halides: History, Properties, and Challenges. J. Phys. Chem. Lett. 9:2326–2337
98. Shyamal S, Dutta SK, Das T, et al (2020) Facets and Defects in Perovskite Nanocrystals for Photocatalytic CO 2 Reduction. J Phys Chem Lett 11:3608–3614. https://doi.org/10.1021/acs.jpclett.0c01088
99. Bera S, Behera RK, Pradhan N (2020) α-Halo Ketone for Polyhedral Perovskite Nanocrystals: Evolutions, Shape Conversions, Ligand Chemistry, and Self-Assembly. J Am Chem Soc 142:20865–20874. https://doi.org/10.1021/jacs.0c10688
100. Baranov D, Lynch MJ, Curtis AC, et al (2019) Purification of Oleylamine for Materials Synthesis and Spectroscopic Diagnostics for trans Isomers. Chem Mater 31:1223–1230.

https://doi.org/10.1021/acs.chemmater.8b04198
101. Yassitepe E, Yang Z, Voznyy O, et al (2016) Amine-Free Synthesis of Cesium Lead Halide Perovskite Quantum Dots for Efficient Light-Emitting Diodes. Adv Funct Mater 26:8757–8763. https://doi.org/10.1002/adfm.201604580
102. Tan Y, Zou Y, Wu L, et al (2018) Highly Luminescent and Stable Perovskite Nanocrystals with Octylphosphonic Acid as a Ligand for Efficient Light-Emitting Diodes. ACS Appl Mater Interfaces 10:3784–3792. https://doi.org/10.1021/acsami.7b17166
103. Seth S, Samanta A (2016) A Facile Methodology for Engineering the Morphology of CsPbX3 Perovskite Nanocrystals under Ambient Condition. Sci Reports 2016 61 6:1–7. https://doi.org/10.1038/SREP37693
104. De La Hoz A, Díaz-Ortiz Á, Moreno A (2005) Microwaves in organic synthesis. Thermal and non-thermal microwave effects. Chem. Soc. Rev. 34:164–178
105. Zhu YJ, Chen F (2014) Microwave-assisted preparation of inorganic nanostructures in liquid phase. Chem. Rev. 114:6462–6555
106. Rao L, Ding X, Du X, et al (2019) Ultrasonication-assisted synthesis of CsPbBr3 and Cs4PbBr6 perovskite nanocrystals and their reversible transformation. Beilstein J Nanotechnol 10:666–676. https://doi.org/10.3762/BJNANO.10.66
107. Li Y, Huang H, Xiong Y, et al (2019) Using Polar Alcohols for the Direct Synthesis of Cesium Lead Halide Perovskite Nanorods with Anisotropic Emission. ACS Nano 13:8237–8245. https://doi.org/10.1021/ACSNANO.9B03508/ASSET/IMAGES/LARGE/NN-2019-035083_0005.JPEG
108. Ng CK, Yin W, Li H, Jasieniak JJ (2020) Scalable synthesis of colloidal CsPbBr 3 perovskite nanocrystals with high reaction yields through solvent and ligand engineering †. 12:4859. https://doi.org/10.1039/c9nr10726f
109. Li Z, Najeeb A, Alves L, et al (2020) Robot-Accelerated Perovskite Investigation and Discovery. Chem Mater 2020:16. https://doi.org/10.1021/acs.chemmater.0c01153
110. Gu E, Tang X, Langner S, et al (2020) Robot-Based High-Throughput Screening of Antisolvents for Lead Halide Perovskites. Joule 4:1806–1822. https://doi.org/10.1016/J.JOULE.2020.06.013
111. Kang J, Wang LW (2017) High Defect Tolerance in Lead Halide Perovskite CsPbBr3. J Phys Chem Lett 8:489–493. https://doi.org/10.1021/acs.jpclett.6b02800
112. Swarnkar A, Chulliyil R, Ravi VK, et al (2015) Colloidal CsPbBr3 Perovskite Nanocrystals: Luminescence beyond Traditional Quantum Dots. Angew Chemie - Int Ed 54:15424–15428. https://doi.org/10.1002/anie.201508276
113. Akkerman QA, D'Innocenzo V, Accornero S, et al (2015) Tuning the optical properties of cesium lead halide perovskite nanocrystals by anion exchange reactions. J Am Chem Soc 137:10276–10281. https://doi.org/10.1021/jacs.5b05602
114. Mondal N, De A, Samanta A (2019) Achieving Near-Unity Photoluminescence Efficiency for Blue-Violet-Emitting Perovskite Nanocrystals. ACS Energy Lett 4:32–39. https://doi.org/10.1021/acsenergylett.8b01909
115. Huang G, Wang C, Xu S, et al (2017) Postsynthetic Doping of $MnCl_2$ Molecules into Preformed $CsPbBr_3$ Perovskite Nanocrystals via a Halide Exchange-Driven Cation Exchange. Adv Mater 29:1700095. https://doi.org/10.1002/adma.201700095
116. Liu H, Wu Z, Shao J, et al (2017) CsPbxMn1-xCl3 Perovskite Quantum Dots with High Mn Substitution Ratio. ACS Nano 11:2239–2247. https://doi.org/10.1021/acsnano.6b08747
117. Mir WJ, Mahor Y, Lohar A, et al (2018) Postsynthesis Doping of Mn and Yb into CsPbX3 (X = Cl, Br, or I) Perovskite Nanocrystals for Downconversion Emission. Chem Mater 30:8170–8178. https://doi.org/10.1021/acs.chemmater.8b03066
118. Begum R, Parida MR, Abdelhady AL, et al (2017) Engineering interfacial charge transfer in CsPbBr3 perovskite nanocrystals by heterovalent doping. J Am Chem Soc 139:731–737. https://doi.org/10.1021/jacs.6b09575
119. Liu M, Zhong G, Yin Y, et al (2017) Aluminum-Doped Cesium Lead Bromide Perovskite Nanocrystals with Stable Blue Photoluminescence Used for Display Backlight. Adv Sci 4:.

https://doi.org/10.1002/ADVS.201700335
120. Ling Y, Tan L, Wang X, et al (2017) Composite Perovskites of Cesium Lead Bromide for Optimized Photoluminescence. J Phys Chem Lett 8:3266–3271. https://doi.org/10.1021/acs.jpclett.7b01302
121. Scheidt RA, Kerns E, Kamat P V. (2018) Interfacial Charge Transfer between Excited CsPbBr 3 Nanocrystals and TiO 2 : Charge Injection versus Photodegradation. J Phys Chem Lett 9:5962–5969. https://doi.org/10.1021/acs.jpclett.8b02690
122. Lu C, Li H, Kolodziejski K, et al (2018) Enhanced stabilization of inorganic cesium lead triiodide (CsPbi 3 ) perovskite quantum dots with tri-octylphosphine. Nano Res 11:762–768. https://doi.org/10.1007/s12274-017-1685-1
123. Song L, Guo X, Hu Y, et al (2017) Efficient Inorganic Perovskite Light-Emitting Diodes with Polyethylene Glycol Passivated Ultrathin CsPbBr3 Films. J Phys Chem Lett 8:4148–4154. https://doi.org/10.1021/acs.jpclett.7b01733
124. Wang Y, Zhang T, Kan M, Zhao Y (2018) Bifunctional Stabilization of All-Inorganic α-CsPbI3 Perovskite for 17% Efficiency Photovoltaics. J Am Chem Soc 140:12345–12348. https://doi.org/10.1021/jacs.8b07927
125. Zhang Q, Zhou Y, Wei Y, et al (2020) Improved phase stability of c-CsPbI 3 perovskite nanocrystals using the interface effect using iodine modified graphene oxide †. J Mater Chem C 8:2569. https://doi.org/10.1039/c9tc06465f
126. Wang H, Fang J, Cheng T, et al (2008) One-step coating of fluoro-containing silica nanoparticles for universal generation of surface superhydrophobicity. Chem Commun 877–879. https://doi.org/10.1039/b714352d
127. Zhang F, Shi ZF, Ma ZZ, et al (2018) Silica coating enhances the stability of inorganic perovskite nanocrystals for efficient and stable down-conversion in white light-emitting devices. Nanoscale 10:20131–20139. https://doi.org/10.1039/c8nr07022a
128. Loiudice A, Saris S, Oveisi E, et al (2017) CsPbBr3 QD/AlOx Inorganic Nanocomposites with Exceptional Stability in Water, Light, and Heat. Angew Chemie - Int Ed 56:10696–10701. https://doi.org/10.1002/anie.201703703
129. Zhang F, Shi Z, Li S, et al (2019) Synergetic Effect of the Surfactant and Silica Coating on the Enhanced Emission and Stability of Perovskite Quantum Dots for Anticounterfeiting. ACS Appl Mater Interfaces 11:28013–28022. https://doi.org/10.1021/acsami.9b07518
130. Park DH, Han JS, Kim W, Jang HS (2018) Facile synthesis of thermally stable CsPbBr3 perovskite quantum dot-inorganic SiO2 composites and their application to white light-emitting diodes with wide color gamut. Dye Pigment 149:246–252. https://doi.org/10.1016/j.dyepig.2017.10.003
131. Zheng Z, Liu L, Yi F, Zhao J (2019) Significantly improving the moisture-, oxygen- and thermal-induced photoluminescence in all-inorganic halide perovskite CsPbI3 crystals by coating the SiO2 layer. J Lumin 216:116722. https://doi.org/10.1016/j.jlumin.2019.116722
132. Li ZJ, Hofman E, Li J, et al (2018) Photoelectrochemically active and environmentally stable cspbbr3/tio2 core/shell nanocrystals. Adv Funct Mater 28:1704288. https://doi.org/10.1002/adfm.201704288
133. Xu YF, Wang XD, Liao JF, et al (2018) Amorphous-TiO 2 -Encapsulated CsPbBr 3 Nanocrystal Composite Photocatalyst with Enhanced Charge Separation and CO 2 Fixation. Adv Mater Interfaces 5:1801015. https://doi.org/10.1002/admi.201801015
134. Liao JF, Xu YF, Wang XD, et al (2018) CsPbBr 3 Nanocrystal/MO 2 (M = Si, Ti, Sn) Composites: Insight into Charge-Carrier Dynamics and Photoelectrochemical Applications. ACS Appl Mater Interfaces 10:42301–42309. https://doi.org/10.1021/acsami.8b14988
135. Zhong Q, Cao M, Hu H, et al (2018) One-pot synthesis of highly stable CsPbBr3@SiO2 core-shell nanoparticles. ACS Nano 12:8579–8587. https://doi.org/10.1021/acsnano.8b04209
136. Stranks SD, Eperon GE, Grancini G, et al (2013) Electron-hole diffusion lengths exceeding 1 micrometer in an organometal trihalide perovskite absorber. Science (80- ) 342:341–344. https://doi.org/10.1126/science.1243982
137. Fang Y, Dong Q, Shao Y, et al (2015) Highly narrowband perovskite single-crystal

photodetectors enabled by surface-charge recombination. Nat Photonics 9:679–686. https://doi.org/10.1038/nphoton.2015.156
138. electron-hole diffusion 175
139. Diroll BT, Nedelcu G, Kovalenko M V., Schaller RD (2017) High-Temperature Photoluminescence of $CsPbX_3$ (X = Cl, Br, I) Nanocrystals. Adv Funct Mater 27:1606750. https://doi.org/10.1002/adfm.201606750
140. Yettapu GR, Talukdar D, Sarkar S, et al (2016) Terahertz Conductivity within Colloidal CsPbBr3 Perovskite Nanocrystals: Remarkably High Carrier Mobilities and Large Diffusion Lengths. Nano Lett 16:4838–4848. https://doi.org/10.1021/acs.nanolett.6b01168
141. Sarkar S, Ravi VK, Banerjee S, et al (2017) Terahertz Spectroscopic Probe of Hot Electron and Hole Transfer from Colloidal CsPbBr3 Perovskite Nanocrystals. Nano Lett 17:5402–5407. https://doi.org/10.1021/acs.nanolett.7b02003
142. Zhai Y, Wang K, Zhang F, et al (2020) Individual Electron and Hole Mobilities in Lead-Halide Perovskites Revealed by Noncontact Methods. ACS Energy Lett 5:47–55. https://doi.org/10.1021/acsenergylett.9b02310
143. Hutter EM, Savenije TJ (2018) Thermally Activated Second-Order Recombination Hints toward Indirect Recombination in Fully Inorganic CsPbI3 Perovskites. ACS Energy Lett 3:2068–2069. https://doi.org/10.1021/acsenergylett.8b01106
144. Gaulding EA, Hao J, Kang HS, et al (2019) Conductivity Tuning via Doping with Electron Donating and Withdrawing Molecules in Perovskite CsPbI3 Nanocrystal Films. Adv Mater 31:1–9. https://doi.org/10.1002/adma.201902250
145. Boehme SC, Brinck S Ten, Maes J, et al (2020) Phonon-Mediated and Weakly Size-Dependent Electron and Hole Cooling in CsPbBr 3 Nanocrystals Revealed by Atomistic Simulations and Ultrafast Spectroscopy. Nano Lett 20:1819–1829. https://doi.org/10.1021/acs.nanolett.9b05051
146. Kobiyama E, Tahara H, Sato R, et al (2020) Reduction of Optical Gain Threshold in CsPbI 3 Nanocrystals Achieved by Generation of Asymmetric Hot-Biexcitons. Nano Lett 20:3905–3910. https://doi.org/10.1021/acs.nanolett.0c01079
147. Hopper T, Gorodetsky A, Krieg F, et al (2019) Hot-carrier cooling in lead-bromide perovskite materials. In: Congreve D, Bronstein HA, Nielsen C, Deschler F (eds) Physical Chemistry of Semiconductor Materials and Interfaces XVIII. SPIE, p 13
148. Li Y, Luo X, Liu Y, et al (2020) Size- and Composition-Dependent Exciton Spin Relaxation in Lead Halide Perovskite Quantum Dots. ACS Energy Lett 5:1701–1708. https://doi.org/10.1021/acsenergylett.0c00525
149. Butkus J, Vashishtha P, Chen K, et al (2017) The Evolution of Quantum Confinement in CsPbBr 3 Perovskite Nanocrystals. Chem Mater 29:3644–3652. https://doi.org/10.1021/acs.chemmater.7b00478
150. Chung H, Jung S Il, Kim HJ, et al (2017) Composition-Dependent Hot Carrier Relaxation Dynamics in Cesium Lead Halide ($CsPbX_3$, X=Br and I) Perovskite Nanocrystals. Angew Chemie Int Ed 56:4160–4164. https://doi.org/10.1002/anie.201611916
151. Chen J, Messing ME, Zheng K, Pullerits T (2019) Cation-Dependent Hot Carrier Cooling in Halide Perovskite Nanocrystals. J Am Chem Soc 141:3532–3540. https://doi.org/10.1021/jacs.8b11867
152. Mondal A, Aneesh J, Kumar Ravi V, et al (2018) Ultrafast exciton many-body interactions and hot-phonon bottleneck in colloidal cesium lead halide perovskite nanocrystals. Phys Rev B 98:115418. https://doi.org/10.1103/PhysRevB.98.115418
153. Mondal N, Samanta A (2017) Complete ultrafast charge carrier dynamics in photo-excited all-inorganic perovskite nanocrystals (CsPbX 3 ). Nanoscale 9:1878–1885. https://doi.org/10.1039/C6NR09422H
154. Castañeda JA, Nagamine G, Yassitepe E, et al (2016) Efficient Biexciton Interaction in Perovskite Quantum Dots under Weak and Strong Confinement. ACS Nano 10:8603–8609. https://doi.org/10.1021/acsnano.6b03908
155. Kaur G, Ghosh HN (2020) Hot Carrier Relaxation in CsPbBr3-Based Perovskites: A Polaron Perspective. J Phys Chem Lett 11:8765–8776.

https://doi.org/10.1021/acs.jpclett.0c02339
156. Rossi D, Wang H, Dong Y, et al (2018) Light-Induced Activation of Forbidden Exciton Transition in Strongly Confined Perovskite Quantum Dots. ACS Nano 12:12436–12443. https://doi.org/10.1021/acsnano.8b06649
157. Mondal A, Aneesh J, Kumar Ravi V, et al (2018) Ultrafast exciton many-body interactions and hot-phonon bottleneck in colloidal cesium lead halide perovskite nanocrystals. Phys Rev B 98:115418. https://doi.org/10.1103/PhysRevB.98.115418
158. Kaur G, Ghosh HN (2020) Hot Carrier Relaxation in CsPbBr3-Based Perovskites: A Polaron Perspective. J Phys Chem Lett 11:8765–8776. https://doi.org/10.1021/acs.jpclett.0c02339
159. Li Y, Lai R, Luo X, et al (2019) On the absence of a phonon bottleneck in strongly confined CsPbBr 3 perovskite nanocrystals. Chem Sci 10:5983–5989. https://doi.org/10.1039/C9SC01339C
160. Madjet ME, Berdiyorov GR, El-Mellouhi F, et al (2017) Cation Effect on Hot Carrier Cooling in Halide Perovskite Materials. J Phys Chem Lett 8:4439–4445. https://doi.org/10.1021/ACS.JPCLETT.7B01732
161. Soetan N, Puretzky A, Reid K, et al (2018) Ultrafast Spectral Dynamics of CsPb(BrxCl1-x)3 Mixed-Halide Nanocrystals. ACS Photonics 5:3575–3583. https://doi.org/10.1021/acsphotonics.8b00413
162. Mandal S, Ghosh S, Mukherjee S, et al (2021) Unravelling halide-dependent charge carrier dynamics in CsPb(Br/Cl)3perovskite nanocrystals. Nanoscale 13:3654–3661. https://doi.org/10.1039/d0nr08428j
163. Begum R, Parida MR, Abdelhady AL, et al (2017) Engineering Interfacial Charge Transfer in CsPbBr 3 Perovskite Nanocrystals by Heterovalent Doping. J Am Chem Soc 139:731–737. https://doi.org/10.1021/jacs.6b09575
164. Wang S, Leng J, Yin Y, et al (2020) Ultrafast Dopant-Induced Exciton Auger-like Recombination in Mn-Doped Perovskite Nanocrystals. ACS Energy Lett 5:328–334. https://doi.org/10.1021/ACSENERGYLETT.9B02678
165. Babu KJ, Kaur G, Shukla A, et al (2020) Concurrent Energy- and Electron-Transfer Dynamics in Photoexcited Mn-Doped CsPbBr3 Perovskite Nanoplatelet Architecture. J Phys Chem Lett 12:302–309. https://doi.org/10.1021/ACS.JPCLETT.0C03267
166. Ketavath R, Katturi NK, Ghugal SG, et al (2019) Deciphering the Ultrafast Nonlinear Optical Properties and Dynamics of Pristine and Ni-Doped CsPbBr 3 Colloidal Two-Dimensional Nanocrystals. J Phys Chem Lett 10:11. https://doi.org/10.1021/acs.jpclett.9b02244
167. Nenon DP, Pressler K, Kang J, et al (2018) Design Principles for Trap-Free CsPbX 3 Nanocrystals: Enumerating and Eliminating Surface Halide Vacancies with Softer Lewis Bases. J Am Chem Soc 140:17760–17772. https://doi.org/10.1021/jacs.8b11035
168. Nan G, Zhang X, Abdi-Jalebi M, et al (2018) How Methylammonium Cations and Chlorine Dopants Heal Defects in Lead Iodide Perovskites. Adv Energy Mater 8:1–9. https://doi.org/10.1002/aenm.201702754
169. Wang L, Liu H, Zhang Y, Mohammed OF (2019) Photoluminescence Origin of Zero-Dimensional Cs4PbBr6 Perovskite. ACS Energy Lett 5:87–99. https://doi.org/10.1021/ACSENERGYLETT.9B02275
170. Guo JJ, Zhao HY, Ai LY, et al (2019) B12@Mg20Al12 core-shell molecule: A candidate for high-capacity hydrogen storage material. Int J Hydrogen Energy 44:28235–28241. https://doi.org/10.1016/j.ijhydene.2019.09.080
171. Brzhezinskaya M, Svechnikov NY, Stankevich VG, et al (2019) Characterization of amorphous hydrocarbon CDx films (x ~ 0.5) for energy storage applications. Fullerenes Nanotub Carbon Nanostructures. https://doi.org/10.1080/1536383X.2019.1686616
172. AL S (2019) Investigations of Physical Properties of XTiH3 and Implications for Solid State Hydrogen Storage. Zeitschrift für Naturforsch A 0: https://doi.org/10.1515/zna-2019-0184
173. Li J, Wang L, Yuan X, et al (2018) Ultraviolet light induced degradation of luminescence in CsPbBr3 perovskite nanocrystals. Mater Res Bull 102:86–91.

https://doi.org/10.1016/j.materresbull.2018.02.021
174. Ye Q, Zhao Y, Mu S, et al (2019) Stabilizing the black phase of cesium lead halide inorganic perovskite for efficient solar cells. Sci China Chem 62:810–821. https://doi.org/10.1007/s11426-019-9504-x
175. Dutta A, Pradhan N (2019) Phase-Stable Red-Emitting CsPbI3 Nanocrystals: Successes and Challenges. ACS Energy Lett 4:709–719. https://doi.org/10.1021/acsenergylett.9b00138
176. Yang MZ, Xu YF, Liao JF, et al (2019) Constructing CsPbBrxI3-x nanocrystal/carbon nanotube composites with improved charge transfer and light harvesting for enhanced photoelectrochemical activity. J Mater Chem A 7:5409–5415. https://doi.org/10.1039/c8ta11760h
177. Kong ZC, Liao JF, Dong YJ, et al (2018) Core@shell cspbbr3@zeolitic imidazolate framework nanocomposite for efficient photocatalytic co2 reduction. ACS Energy Lett 3:2656–2662. https://doi.org/10.1021/acsenergylett.8b01658
178. Kong ZC, Zhang HH, Liao JF, et al (2020) Immobilizing Re(CO)3Br(dcbpy) Complex on CsPbBr3 Nanocrystal for Boosted Charge Separation and Photocatalytic CO2 Reduction. Sol RRL 4:1900365. https://doi.org/10.1002/solr.201900365
179. Shyamal S, Dutta SK, Das T, et al (2020) Facets and Defects in Perovskite Nanocrystals for Photocatalytic CO2Reduction. J Phys Chem Lett 11:3608–3614. https://doi.org/10.1021/acs.jpclett.0c01088
180. Song W, Wang Y, Wang C, et al (2021) Photocatalytic Hydrogen Production by Stable CsPbBr3@PANI Nanoparticles in Aqueous Solution. ChemCatChem 13:1711–1716. https://doi.org/10.1002/cctc.202001955
181. Corti M, Bonomi S, Chiara R, et al (2021) Application of metal halide perovskites as photocatalysts in organic reactions. Inorganics 9:. https://doi.org/10.3390/inorganics9070056
182. Zhang Y, Siegler TD, Thomas CJ, et al (2020) A “tips and Tricks” Practical Guide to the Synthesis of Metal Halide Perovskite Nanocrystals. Chem Mater 32:5410–5423. https://doi.org/10.1021/acs.chemmater.0c01735
183. Xu Y, Zhang W, Su K, et al (2021) Glycine-Functionalized CsPbBr3 Nanocrystals for Efficient Visible-Light Photocatalysis of CO2 Reduction. Chem - A Eur J 27:2305–2309. https://doi.org/10.1002/chem.202004682
184. Li Y, Shu Q, Du Q, et al (2020) Surface Modification for Improving the Photocatalytic Polymerization of 3,4-Ethylenedioxythiophene over Inorganic Lead Halide Perovskite Quantum Dots. ACS Appl Mater Interfaces 12:451–460. https://doi.org/10.1021/acsami.9b14365
185. Wu LY, Zhang MR, Feng YX, et al (2021) Two-Dimensional Metal Halide Perovskite Nanosheets for Efficient Photocatalytic CO2 Reduction. Sol RRL 5:1–9. https://doi.org/10.1002/solr.202100263
186. Knezevic M, Quach VD, Lampre I, et al (2023) Adjusting the band gap of CsPbBr3−yXy (X = Cl, I) for optimal interfacial charge transfer and enhanced photocatalytic hydrogen generation. J Mater Chem A 11:6226–6236. https://doi.org/10.1039/D2TA09920A
187. Guo SH, Zhou J, Zhao X, et al (2019) Enhanced CO2 photoreduction via tuning halides in perovskites. J Catal 369:201–208. https://doi.org/10.1016/j.jcat.2018.11.004
188. Shyamal S, Dutta SK, Pradhan N (2019) Doping Iron in CsPbBr3 Perovskite Nanocrystals for Efficient and Product Selective CO2 Reduction. J Phys Chem Lett 10:7965–7969. https://doi.org/10.1021/acs.jpclett.9b03176
189. Liu Y, Guo S, You S, Sun C (2020) Mn-doped CsPb ( Br / Cl ) 3 mixed-halide perovskites for CO 2 photoreduction. Nanotechnology 3:0–5
190. Mu YF, Zhang W, Guo XX, et al (2019) Water-Tolerant Lead Halide Perovskite Nanocrystals as Efficient Photocatalysts for Visible-Light-Driven CO2 Reduction in Pure Water. ChemSusChem 12:4769–4774. https://doi.org/10.1002/cssc.201902192
191. Ding L, Shen C, Zhao Y, et al (2020) CsPbBr3 nanocrystals glass facilitated with Zn ions for photocatalytic hydrogen production via H2O splitting. Mol Catal 483:1–7. https://doi.org/10.1016/j.mcat.2020.110764

192. Chen Z, Hu Y, Wang J, et al (2020) Boosting Photocatalytic CO2 Reduction on CsPbBr3 Perovskite Nanocrystals by Immobilizing Metal Complexes. Chem Mater 32:1517–1525. https://doi.org/10.1021/acs.chemmater.9b04582
193. Kong ZC, Zhang HH, Liao JF, et al (2020) Immobilizing Re(CO)3Br(dcbpy) Complex on CsPbBr3 Nanocrystal for Boosted Charge Separation and Photocatalytic CO2 Reduction. Sol RRL 4:2–8. https://doi.org/10.1002/solr.201900365
194. Xu YF, Yang MZ, Chen BX, et al (2017) A CsPbBr3 Perovskite Quantum Dot/Graphene Oxide Composite for Photocatalytic CO2 Reduction. J Am Chem Soc 139:5660–5663. https://doi.org/10.1021/jacs.7b00489
195. Xu YF, Yang MZ, Chen HY, et al (2018) Enhanced Solar-Driven Gaseous CO2 Conversion by CsPbBr3 Nanocrystal/Pd Nanosheet Schottky-Junction Photocatalyst. ACS Appl Energy Mater 1:5083–5089. https://doi.org/10.1021/acsaem.8b01133
196. Kobosko SM, Dubose JT, Kamat P V. (2020) Perovskite Photocatalysis. Methyl Viologen Induces Unusually Long-Lived Charge Carrier Separation in CsPbBr3 Nanocrystals. ACS Energy Lett 5:221–223. https://doi.org/10.1021/acsenergylett.9b02573
197. Dubose JT, Kamat P V. (2019) Probing Perovskite Photocatalysis. Interfacial Electron Transfer between CsPbBr3 and Ferrocene Redox Couple. J Phys Chem Lett 10:6074–6080. https://doi.org/10.1021/acs.jpclett.9b02294
198. Li L, Zhang Z, Ding C, Xu J (2021) Boosting charge separation and photocatalytic CO2 reduction of CsPbBr3 perovskite quantum dots by hybridizing with P3HT. Chem Eng J 419:129543. https://doi.org/10.1016/j.cej.2021.129543
199. Li L, Zhang Z, Ding C, Xu J (2021) Boosting charge separation and photocatalytic CO2 reduction of CsPbBr3 perovskite quantum dots by hybridizing with P3HT. Chem Eng J 419:129543. https://doi.org/10.1016/J.CEJ.2021.129543
200. Zhang Z, Shu M, Jiang Y, Xu J (2021) Fullerene modified CsPbBr3 perovskite nanocrystals for efficient charge separation and photocatalytic CO2 reduction. Chem Eng J 414:128889. https://doi.org/10.1016/j.cej.2021.128889
201. Pan A, Ma X, Huang S, et al (2019) CsPbBr3 Perovskite Nanocrystal Grown on MXene Nanosheets for Enhanced Photoelectric Detection and Photocatalytic CO2 Reduction. J Phys Chem Lett 10:6590–6597. https://doi.org/10.1021/acs.jpclett.9b02605
202. Ou M, Tu W, Yin S, et al (2018) Amino-Assisted Anchoring of CsPbBr3 Perovskite Quantum Dots on Porous g-C3N4 for Enhanced Photocatalytic CO2 Reduction. Angew Chemie - Int Ed 57:13570–13574. https://doi.org/10.1002/anie.201808930
203. Zhou L (2018) Fundamentals of Combustion Theory. Theory Model Dispersed Multiph Turbul React Flows 15–70. https://doi.org/10.1016/B978-0-12-813465-8.00003-X
204. Guo XX, Tang SF, Mu YF, et al (2019) Engineering a CsPbBr3-based nanocomposite for efficient photocatalytic CO2 reduction: Improved charge separation concomitant with increased activity sites. RSC Adv 9:34342–34348. https://doi.org/10.1039/c9ra07236e
205. Su K, Dong GX, Zhang W, et al (2020) In Situ Coating CsPbBr3Nanocrystals with Graphdiyne to Boost the Activity and Stability of Photocatalytic CO2Reduction. ACS Appl Mater Interfaces 12:50464–50471. https://doi.org/10.1021/acsami.0c14826
206. Gu K, Wang Y, Shen J, et al (2020) Effective Singlet Oxygen Generation in Silica-Coated CsPbBr3 Quantum Dots through Energy Transfer for Photocatalysis. ChemSusChem 13:682–687. https://doi.org/10.1002/cssc.201903157
207. Xu YF, Wang XD, Liao JF, et al (2018) Amorphous-TiO2-Encapsulated CsPbBr3 Nanocrystal Composite Photocatalyst with Enhanced Charge Separation and CO2 Fixation. Adv Mater Interfaces 5:1–8. https://doi.org/10.1002/admi.201801015
208. Sun QM, Xu JJ, Tao FF, et al (2022) Boosted Inner Surface Charge Transfer in Perovskite Nanodots@Mesoporous Titania Frameworks for Efficient and Selective Photocatalytic CO2 Reduction to Methane. Angew Chemie Int Ed 61:e202200872. https://doi.org/10.1002/ANIE.202200872
209. Mu YF, Zhang W, Dong GX, et al (2020) Ultrathin and Small-Size Graphene Oxide as an Electron Mediator for Perovskite-Based Z-Scheme System to Significantly Enhance Photocatalytic CO2 Reduction. Small 16:2002140.

https://doi.org/10.1002/SMLL.202002140
210. Tang R, Zhou S, Li H, et al (2020) Halogen bonding induced aqueously stable CsPbBr3@MOFs-Derived Co3O4/N-doped-C heterostructure for high-performance photoelectrochemical water oxidation. Appl Catal B Environ 265:118583. https://doi.org/10.1016/j.apcatb.2019.118583
211. Chen ZY, Hong QL, Zhang HX, Zhang J (2022) Composite of CsPbBr3with Boron Imidazolate Frameworks as an Efficient Visible-Light Photocatalyst for CO2Reduction. ACS Appl Energy Mater 5:1175–1182. https://doi.org/10.1021/acsaem.1c03552